

RESEARCH ON SLOPE STABILITY AND
LANDSLIDE MOBILITY DURING EARTHQUAKES

地震時における斜面の安定性と
地すべりの運動特性に関する研究

Oct. 2013

Deping GUO

郭 德平

RESEARCH ON SLOPE STABILITY AND
LANDSLIDE MOBILITY DURING EARTHQUAKES

地震時における斜面の安定性と
地すべりの運動特性に関する研究

Oct. 2013

Waseda University
Graduate School of Creative Science and Engineering
Major in Civil and Environmental Engineering
Research on Earthquake Engineering

Deping GUO

郭 德平

Preface

The 2008 Wenchuan earthquake occurred at Wenchuan County in Sichuan province, southwest China. At that time, I was an undergraduate student of Southwest Jiaotong University, which is about 65km from epicenter. The strong ground motion shook everything around me and my heart. From that moment, I planned to combine my major, tunnel engineering, with earthquake engineering, and then studied overseas in Waseda University.

After the earthquake, I visited the severe damage areas several times, such as Yingxiu County, MaoXian and Dujiangyan; the damage scenes deeply impressed on my mind. Slope failure was one of the typical seismic geo-hazards during the 2008 Wenchuan earthquake, which caused a large amount of disasters; hence, my study on earthquake engineering began with the slope stability and the mobilization of slope failure triggered by earthquake.

The work presented in this thesis was initiated from October 2010 when I was admitted as a doctorate program student in Waseda University. The thesis mainly consists of four parts; the analysis is not only from the global viewpoint to local viewpoint, but also from slope stability and its dynamic response to landslide mobility and its travel distance. The first part reported the overview of Wenchuan earthquake and slope failure distribution regularity; the second part concerned numerous influential factors on slope stability and its dynamic response; the third part explored influential factors on landslide mobility and travel distance, further proposed two statistical models for the prediction of landslide mobility and travel distance; the forth part reported seismic performance of slope reinforcements based on field investigation, indenting to learn from seismic damage for future mitigation of slope disasters.

Deping Guo



Acknowledgements

I am grateful to a large number of people who have supported me during my doctoral period on the professional or personal level.

First of all, I would like to express my deep appreciation to my research advisor, Professor Masanori Hamada, for invaluable guidance and many fruitful discussions, and also for his kindness to care for my oversea life. I am very grateful to my domestic advisor, Professor Chuan He, for his kind recommendation to make me study abroad. I would like to deeply thank the thesis committee members, Professor Ömer Aydan, Professor Hirokazu Akagi, for their careful review and constructive comments. I would like to thank Professor Charles Scawthorn, research engineer Jun Itoh for their valuable discussions and suggestions during my studies. I am greatly thankful to the China Scholarship Council (CSC) and Waseda University for their financial supports.

I would like to thank Professor Shanjie Gan, Dr. Yufeng Wang, Dr. Guo Li, Dr. Chong Xu, Dr. Hongling Tian, Dr. Gang Luo, Dr. Jinghe Wang, Yifeng Zhang, Dr. Rui Guo, Dr. Qinghua Yang, Dr. Xin Liao, Engineer Yi Xu and Yafeng Jin, Zhiyu Tian, Professor Qiang Xu, Professor Linkan Yao, Professor Jianjing Zhang, Dr. Dage Song, Dr. Lin Li, Dr. Fei Chen, Lei Zou and Chenghao Zhu for their kind help during my field investigation and data collection.

Great appreciation to my dear friends, Hong Lai, Zeng Zhang, Zhifeng Sun, for their selfless and heart-warming help and encouragement, especially during the preparation of my application and formalities for going abroad.

I am extremely grateful to all members of the Hamada Laboratory for providing a calm academic research environment; especially I would like to mention the laboratory secretary Ms. Tamami Koyama, Ms. Ritsu Asaoka, and Dr. Ikki Kato, Dr. Namyi Yun, Dr. Saima Riaz. Their kind help and encouragement have contributed to many joyful memories.

At last, not least but endless, I want to thank my family. My grandmother, mother, father-Shuhua Yang, Runfen Liu, Caiwen Guo, who always support me in silence, who always encourage me in silence, who always contribute themselves to enrich me in silence. My gratitude to my dear family is beyond any words. I deeply appreciated my wife, Jing Huang, for her patience, understanding and support.

Abstract

The 2008 Wenchuan earthquake with a surface wave magnitude of 8.0 occurred at Yingxiu County in Longmenshan thrust fault belt, southwest China, having triggered a huge amount of slope failures. This catastrophic earthquake had disastrous consequences and took more than 80,000 lives, which one third was attributed to slope failures. In order to study on the distribution regularity of slope failures related with seismic parameters, and the influential factors on slope stability and landslide mobility, field investigation, statistical analysis, theoretical derivation and finite element simulation were used.

A detailed inventory with more than 190,000 slope failures and strong ground motion records of 187 seismic stations were used to analyze the qualitative and quantitative relations between slope failure distribution and seismic parameters in Wenchuan earthquake wholly affected area. The results revealed that slope failure distribution exponentially decreased with the increment of epicentral distance and distance from surface fault rupture; seismic acceleration attenuation and slope failure distribution provided solid evidences to the existence of hanging-foot wall effect, because peak ground acceleration (PGA) on the hanging wall side was apparently larger than that on footwall side, resulting in slope failures on the hanging wall side was predominantly more than those on footwall side. Linear correlation between slope failure distribution and PGA was demonstrated by regressive analysis, which revealed that 0.18–0.21g horizontal PGA was the threshold value of slope failure occurrence. Furthermore, an empirical model for slope failure distribution attenuation was discussed in Chapter 2.

A case study of landslide distribution and slope stability related with numerous influential factors was implemented based on field investigation of 119 landslides in Wenchuan County. The effectiveness of each influential factor on slope stability was studied by multivariable analysis and demonstrated that slope height, horizontal peak ground acceleration and geological structure had stronger effect on the sliding source area and volume than slope angle and rock type. In order to analyze more influential factors on slope dynamic responses, theoretical derivation was conducted to study the influences of geomechanical parameters and seismic wave parameters. The analytical results revealed that the shape of contour plot of displacement amplification ratio was determined by seismic wave frequency; with the increment of frequency, the contour plot changed from parallel to slope surface to rhythm

distribution with multiple peak values. Lower frequency induced more dangerous dynamic responses; the maximum displacement amplification ratio relied on Poisson's ratio, input angle of seismic wave and slope angle; mass density had smaller effect on slope dynamic responses than Young's modulus; the thickness of saliently affected region by earthquake become larger with the increment of Young's modulus and seismic wave input angle, and with the decrease of seismic wave frequency. Furthermore, the effect of topography on slope dynamic responses was discussed based on finite element simulation. Five simplified slopes with different shapes were analyzed under three typical seismic waves, the results revealed that seismic acceleration was generally amplified with the increment of slope elevation, especially, at the steep section and ground surface curvature sharp changing section; slopes with convex and S-like shape were much more unstable than other three slope types during earthquakes; step-like slope had relatively highest stability; concave slope and inverse S-like slope had medium stability.

High mobility landslide was a severe hazard to endanger the area along travel path due to time limitation of evacuation. It is essential to evaluate the effects of influential factors on landslide mobility, so as to better understand the movement of landslide. Hence, the relations between equivalent coefficient of friction ($\mu=H_{\max}/L_{\max}$) and other 6 parameters of 46 landslides, such as topographical factors, landslide volume, horizontal PGA and rock type, have been qualitatively analyzed by means of simplified plots. The effectiveness of each factor on landslide mobility ($1/\mu$) was revealed by multivariable analysis and proposed that rock type, landslide volume, slope transition angle and slope height had predominant effect on landslide mobility and its travel distance. Furthermore, two statistical models for predicting equivalent coefficient of friction and travel distance were developed, respectively, intending to serve relocation and rehabilitation; their validities were verified by satisfactory agreement between observations and predictions, and further compared with previous statistical models.

Finally, in order to learn from seismic damage, seismic performance of slope reinforcements was surveyed and showed that anchor cable, frame beam and soil nailing wall had good anti-seismic property, however, shotcrete with bolts had limited ability to enhance slope stability during earthquake.

Keywords: Slope failure distribution; Slope stability; Slope dynamic responses; Landslide mobility; Influential factors; Wenchuan earthquake

List of Figures

Figure 1.1 Sketches of major types of landslide.....	3
Figure 1.2 Sketches of slope failure	4
Figure 1.3 Major tectonic and geological settings in and around the China	5
Figure 1.4 Fault system of Longmenshan fault zone.....	6
Figure 1.5 3-Dimensional model of the Longmenshan fault.....	8
Figure 1.6 Geological formation in the severely damaged area	9
Figure 1.7 Earthquake-indeced displacement distribution along surface ruptures.....	11
Figure 1.8 Seismic intensity map of 2008 Wenchuan earthquake	12
Figure 1.9 Typically catastrophic landslides	14
Figure 1.10 Typical seismic damages of bridges during Wenchuan earthquake	15
Figure 1.11 Statistics of bridge seismic damages along Road213 and Du-Wen expressway	15
Figure 1.12 Typical seismic damages of tunnels during Wenchuan earthquake.....	16
Figure 1.13 Statistics of tunnel seismic damages along Road213 and Du-Wen expressway.....	16
Figure 1.14 Research flow chart and graphic abstract.....	25
Figure 2.1 The distribution of strong motion stations triggered by the main shock of Wenchuan earthquake	36
Figure 2.2 Slope failure distribution induced by Wenchuan earthquake and a part of surrounding strong motion stations	37
Figure 2.3 Slope failure distribution with respect to epicenter, with 5km width concentric band	39
Figure 2.4 Slope failure distribution regularity with respect to epicentral distance.	40
Figure 2.5 Slope failure distribution with respect to Yingxiu-Beichuan surface fault rupture	41
Figure 2.6 Slope failure distribution with respect to distance from Yingxiu-Beichuan surface fault rupture	41
Figure 2.7 Slope failure distribution related with fault rupturing motion	42
Figure 2.8 Selected strong motion stations in the rectangle for studying seismic ground motion attenuation with respect to Yingxiu-Beichuan surface fault rupture.....	44
Figure 2.9 Peak ground acceleration attenuation on the hanging wall side and footwall side	45
Figure 2.10 The quantitative relation between slope failure distribution and seismic ground motion on the hanging wall side.....	46

Figure 2.11 The quantitative relation between slope failure distribution and seismic ground motion on the footwall side	47
Figure 2.12 Slope failure distribution related with lithology	48
Figure 2.13 Area comparison of susceptible lithology of slope failure occurrence between hanging wall side and footwall side	49
Figure 2.14 Slope failure distribution attenuation during the 2008 Wenchuan earthquake, 1989 Loma Prieta earthquake and 1999 Chi-Chi earthquake	51
Figure 3.1 (a) The distribution of strong motion stations around Wenchuan County. (b) The distribution of investigated landslides in Wenchuan County	58
Figure 3.2 Typical longitudinal profile of slope.....	59
Figure 3.3 Landslide distribution related with the distance from surface fault rupture.....	61
Figure 3.4 The distribution of estimated horizontal PHA in Wenchuan County	61
Figure 3.5 Landslide distribution related with horizontal peak ground acceleration	62
Figure 3.6 Landslide distribution related with slope angle	63
Figure 3.7 Landslide distribution related with slope height	64
Figure 3.8 Landslide distribution related with rock type.....	64
Figure 3.9 The relation between slope angle and inclination of rock layer for failure modes	66
Figure 3.10 Landslide distribution related with geological structure	67
Figure 3.11 Comparing square root of observed sliding source area with the predicted values	69
Figure 3.12 Comparing cube root of observed sliding source volume with the predicted values.....	70
Figure 3.13 Sketch of S-wave mode conversion on the inclined free air surface	71
Figure 3.14 P-wave and S-wave reflection coefficients related to Poisson's ratio and input angle	73
Figure 3.15 Sketch of seismic wave superposition	74
Figure 3.16 Contour plots of displacement amplification ratio related to different parameters.....	78
Figure 3.17 Sketches of five slopes with simplified ground surface.....	81
Figure 3.18 2-D numerical model of step-like slope	81
Figure 3.19 Typical acceleration time history of Wenchuan earthquake	83
Figure 3.20 Typical acceleration time history of El Centro earthquake.....	84
Figure 3.21 Typical acceleration time history of Kobe earthquake	84
Figure 3.22 Natural frequency comparison among five typical slopes	85
Figure 4.1 The sketch of landslide and its deposit for terminological definition	93
Figure 4.2 The location of 46 landslides in Wenchuan earthquake area	94
Figure 4.3 Typical longitudinal profile of a long travel landslide	95

Figure 4.4 Landslide travel distance related with sliding source volume.....	96
Figure 4.5 Landslide travel distance related with sliding source area.....	96
Figure 4.6 Landslide travel distance related with landslide height	97
Figure 4.7 Equivalent coefficient of friction related with tangent of slope angle	98
Figure 4.8 Equivalent coefficient of friction related with sine of slope transition angle.....	99
Figure 4.9 Statistical histogram of slope transition angle	99
Figure 4.10 Equivalent coefficient of friction related with slope height.....	100
Figure 4.11 Equivalent coefficient of friction related with seismic acceleration	101
Figure 4.12 Equivalent coefficient of friction related with rock type	102
Figure 4.13 Equivalent coefficient of friction related with landslide source volume	103
Figure 4.14 Predicted versus observed equivalent coefficient of friction	106
Figure 4.15 Predicted equivalent coefficient of friction by previous models versus the observed	107
Figure 4.16 Landslide mobility of unconfined debris flows (Hunter and Fell, 2003).....	108
Figure 4.17 Predicted versus observed horizontal travel distance.....	110
Figure 4.18 Predicted landslide travel distance by Rickenmann's model versus the observed	113
Figure 4.19 Predicted landslide travel distance by Legros's model versus the observed.....	113
Figure 5.1 The sketch of investigated route	121
Figure 5.2 Performance of anchor cable reinforced slopes and reinforcement parameters.....	122
Figure 5.3 Comparison between reinforced slope and non-reinforced slope	123
Figure 5.4 Performance of frame beam reinforced slope and reinforcement parameters.....	124
Figure 5.5 Performance of soil nailing wall reinforced slope and its reinforcement parameters	125
Figure 5.6 Cracks and steel mesh exposure of the slope reinforced by soil nailing wall.....	126
Figure 5.7 Performance of slopes reinforced by shotcrete with bolts	126
Figure 5.8 The comparison of damage percent among four reinforcements	127
Figure 5.9 Reinforcement principle sketch of shotcrete with bolts.....	128
Figure 5.10 Reinforcement principle sketch of soil nailing wall	128
Figure 5.11 The comparison of average collapse depth between non-reinforced slopes and shotcrete with bolts reinforced slopes.....	129

List of Tables

Table 1.1 Types of landslide.....	2
Table 1.2 Symbol and typical lithology of geological formation in Wenchuan earthquake area.....	10
Table 1.3 The summary of 31 catastrophic slope failures	13
Table 2.1 Regression parameters of acceleration attenuation on the hanging wall and footwall side with respect to Yingxiu-Beichuan surface fault rupture.....	45
Table 2.2 Threshold PGA value of slope failure occurrence about three recent earthquakes	47
Table 2.3 Regression parameters of empirical model for slope failure distribution attenuation	52
Table 3.1 Classification standard of rock type	59
Table 3.2 Regression parameters of horizontal acceleration attenuation model	60
Table 3.3 Sketches of geological structure	65
Table 3.4 Multivariable analysis of sliding area related with influential factors.....	68
Table 3.5 Multivariable analysis of sliding volume related with influential factors	69
Table 3.6 Different parameters of compared slopes	77
Table 3.7 Geomechanical parameters of slope materials	81
Table 3.8 Acceleration amplification ratio of five simplified slopes with different shapes	86
Table 3.9 Contour plots of equivalent plastic strain of five simplified slopes with different shapes ...	88
Table 4.1 Multivariable analysis of landslide mobility by backward elimination approach	104
Table 4.2 Landslide mobility prediction models and their comparisons	107
Table 4.3 Multivariable analysis of landslide travel distance by backward elimination approach ...	109
Table 4.4 The validation of proposed statistical model for landslide travel distance by case studies	111
Table 4.5 Landslide travel distance prediction models and their comparisons	112

List of Symbols

R_e	Epicentral distance
D_{rup}	Distance from site to Yingxiu-Beichuan surface fault rupture
LNC	Number concentration of slope failure
LAP	Area distribution percentage of slope failure
PGA	Peak ground acceleration
PHA	Horizontal peak ground acceleration
h	Slope height
θ	Slope angle
A	Landslide source area
V	Landslide source volume
δ	Inclination of rock layer
RT	Rock type
L_{max}	Landslide horizontal travel distance
H_{max}	Landslide maximum elevation loss
ε	Slope transition angle
μ	Equivalent coefficient of friction
S_d, S'_d, S''_d	Seismic wave displacement
$\mathbf{S}_d, \mathbf{S}'_d, \mathbf{S}''_d$	Seismic wave displacement vector
k, k', k''	Wave number
$\omega, \omega', \omega''$	Seismic wave circular frequency
f	Seismic wave frequency
v_s	S-wave velocity

v_p	P-wave velocity
η_{pd}	Displacement reflection coefficient of P-wave
η_{sd}	Displacement reflection coefficient of S-wave
S_{hor}	Horizontal component of seismic wave displacement
S_{ver}	Vertical component of seismic wave displacement
ζ_d	Displacement amplification ratio of seismic wave
ζ_v	Velocity amplification ratio of seismic wave
ζ_a	Acceleration amplification ratio of seismic wave
E_d	Young's modulus
ν	Poisson's ratio
ρ	Mass density
ϕ	Seismic wave input angle
ψ	Seismic wave reflected angle
φ	Friction angle
φ_j	Friction angle of stratum joint
c	Cohesion stress
$[C]$	Damping matrix
$[M]$	Structural mass matrix
$[K]$	Structural stiffness matrix
α	Mass proportional Rayleigh damping coefficient
β	Stiffness proportional Rayleigh damping coefficient
ξ	Damping ratio

List of Contents

<i>Preface</i>	I
<i>Acknowledgements</i>	II
<i>Abstract</i>	III
<i>List of Figures</i>	V
<i>List of Tables</i>	VIII
<i>List of Symbols</i>	IX
<i>List of Contents</i>	XI

Chapter 1 Introduction

1.1 The terms for the disaster related with slope.....	1
1.2 Overview of Wenchuan earthquake	5
1.2.1 Tectonic and geological settings	5
1.2.2 Fault surface rupture and seismic intensity	10
1.2.3 Disasters related with slope failure.....	12
1.3 Reviews of previous researches	17
1.3.1 Researches on slope failure distribution related with seismic parameters	17
1.3.2 Researches on influential factors of slope stability and dynamic responses	18
1.3.3 Researches on landslide mobility	20
1.3.4 Researches on landslide travel distance	21
1.4 Research objectives and procedures.....	22
References	26

Chapter 2 Slope Failure Distribution and Seismic Ground Motion

2.1 Introduction	35
2.2 Data source of Wenchuan earthquake	35
2.3 Slope failure distribution regularity.....	38
2.3.1 Slope failure distribution with respect to epicenter	38
2.3.2 Slope failure distribution with respect to surface fault rupture	40
2.4 Seismic ground motion attenuation.....	43
2.5 Quantitative relation between slope failure distribution and seismic ground motion	46
2.6 Discussions.....	50

2.7 Summary	53
References	53

Chapter 3 Influential Factors on Slope Stability and Slope Dynamic Responses

3.1 Introduction	57
3.2 Influential factors on landslide distribution and slope stability.....	58
3.2.1 Landslide data collection in Wenchuan County	58
3.2.2 Qualitative analysis of influential factors on landslide distribution	60
3.2.2.1 The effect of seismic acceleration	60
3.2.2.2 The effects of slope angle and height	62
3.2.2.3 The effects of rock type and geological structure.....	64
3.2.3 Multivariable analysis of influential factors on slope stability.....	67
3.3 Theoretical analysis of influential factors on slope dynamic responses.....	71
3.3.1 Wave mode conversion on the free air surface.....	71
3.3.2 Seismic wave superposition	74
3.3.3 The cases of analysis	76
3.3.4 The results and analyses of dynamic responses.....	77
3.3.4.1 Displacement amplification ratio related with parameters	77
3.3.4.2 The effects of geomechanical parameters	78
3.3.4.2 The effects of seismic wave parameters	79
3.3.4.2 The effect of slope angle	80
3.4 FEM analysis of slope shape on dynamic responses.....	80
3.4.1 Simplification of slope ground surface and numerical models	80
3.4.2 Seismic source waves.....	83
3.4.3 The influence on vibration mode.....	84
3.4.4 The influence on acceleration amplification	85
3.4.5 The influence on equivalent plastic strain.....	87
3.5 Summary	89
References	90

Chapter 4 Influential Factors on Landslide Mobility and Travel Distance

4.1 Introduction	92
4.2 Data source.....	93
4.3 Relationships between landslide travel distance and landslide parameters.....	96
4.4 Qualitative analysis of influential factors on landslide mobility.....	98
4.4.1 The effects of topographical factors	98
4.4.2 The effect of seismic acceleration	100
4.4.3 The effect of rock type	101

4.4.4 The effect of landslide volume	102
4.5 Statistical model of landslide mobility	103
4.5.1 Development of statistiacal model	104
4.5.2 Comparison with previous models	106
4.6 Statistical model of landslide travel distance	108
4.6.1 Development of statistical model	108
4.6.2 Comparison with previous models	112
4.7 Discussions.....	114
4.8 Summary	116
References	116

Chapter 5 Seismic Performance of Reinforced Slope

5.1 Introduction	121
5.2 Anti-seismic behaviors of different slope reinforcements.....	122
5.3 Comparison and analysis of four reinforcements.....	127
5.4 Summary	130
References	130

Chapter 6 Conclusions and Future Perspectives

6.1 Finding summary.....	132
6.2 Future research topics.....	135

Appendix

Table 1: The parameters of 187 strong motion stations	137
Table 2: 119 landslides in Wenchuan County induced by Wenchuan earthquake.....	145
Table 3: 46 landslides with relatively long travel distance induced by Wenchuan earthquake	151

Chapter 1 Introduction

At the local time 14:28(06:28 UTC) on May 12, 2008, a $M_s=8.0$ earthquake occurred at Longmenshan thrust fault belt in Wenchuan County of Sichuan province, southwest China, the location of epicenter is 31.021° north latitude, 103.367° east longitude, with 14km focal depth (China earthquake administration, CAE, 2008). In the 75 days after the main shock, 20,000 aftershocks were recorded, which included 241 with $M_s \geq 4.0$, 205 with $4.0 \leq M_s \leq 4.9$, 30 with $5.0 \leq M_s \leq 5.9$ and 6 with $M_s \geq 6.0$ (Chen, et al., 2008). This catastrophic earthquake had caused heavy damage to the infrastructure, communications and electronic power systems, especially in the Wenchuan, Beichuan, Qingchuan, Dujiangyan, Pengzhou, Shifang, Mianzhu, Jiangyou, Pingwu, Lixian, Maoxian, Wenxian (Gansu province) and Ningqiang(Shanxi province). The seriously affected area is over $130,000\text{km}^2$, resulting in 69,227 casualties, 17,293 missing, 374,643 injured and 10 million people homeless (Ministry of Civil Affairs, 2008); the total economic loss was estimated about 10 trillion RMB (Chen, et al., 2008); 24 expressways, 161 national roads and 8618 county roads were blocked, 6140 bridges and 156 tunnels were damaged in different degrees (Liu, et al., 2008), and countless houses were severely destroyed.

1.1 The terms for the disaster related with slope

There are many terms for the disaster related with slope, such as landslide, slope failure, landslip or slumps, and also some researchers used “geo-hazard” to generally call the disaster related with slope (Huang and Li, 2009a).

A landslide is defined as “the movement of a mass of rock, debris, or earth down a slope” (Cruden, 1991). Landslide is a type of “mass wasting”, which denotes any down-slope movement of soil and rock under the direct influence of gravity. The term “landslide” encompasses five modes of slope movement: falls, topples, slides, spreads, and flows. These are further subdivided

by the type of geologic material (rock, debris, or soil). Debris flows (commonly referred to as mudflows or mudslides) and rock falls are examples of common landslide types (Cruden and Varnes, 1996). British Geological survey takes the definition of landslide from Cruden (1991) for the Working Party on World Landslide Inventory.

From Geoscience Australia, the definition of landslide is as follows: A landslide is the movement of rock, debris or earth down a slope. The results from the failure of the materials which make up the hill slope are driven by the force of gravity. Besides, landslides are also named as landslips, slumps or slope failure. The basic types of landslide movement are: fall, topple, flow, slide and spread.

From U.S. Geological Survey, a landslide is a movement of surface material down a slope. The term “landslide” describes a wide variety of processes that result in the downward and outward movement of slope-forming materials including rock, soil, artificial fill, or a combination of these. The materials may move by falling, toppling, sliding, spreading, or flowing.

Based on above mentioned definitions from globally typical institutes, there is very little difference among them, and all of them agree with the definition from Cruden (1991). The different types of landslide are summarized in **Table 1.1** and illustrated in **Figure 1.1**.

Table 1.1 Types of landslide

Type of movement	Type of material		
	Rock	Soils	
		Predominantly coarse	Predominantly fine
Falls	Rock fall	Debris fall	Earth fall
Topples	Rock topple	Debris topple	Earth topple
Slides	Rotational	Debris slide	Earth slide
	Translational		
Lateral spreads	Rock spread	Debris spread	Earth spread
Flows	Rock flow	Debris flow	Earth flow
	(Deep creep)	(Soil creep)	
Complex	Combination of two or more principal types of movement		

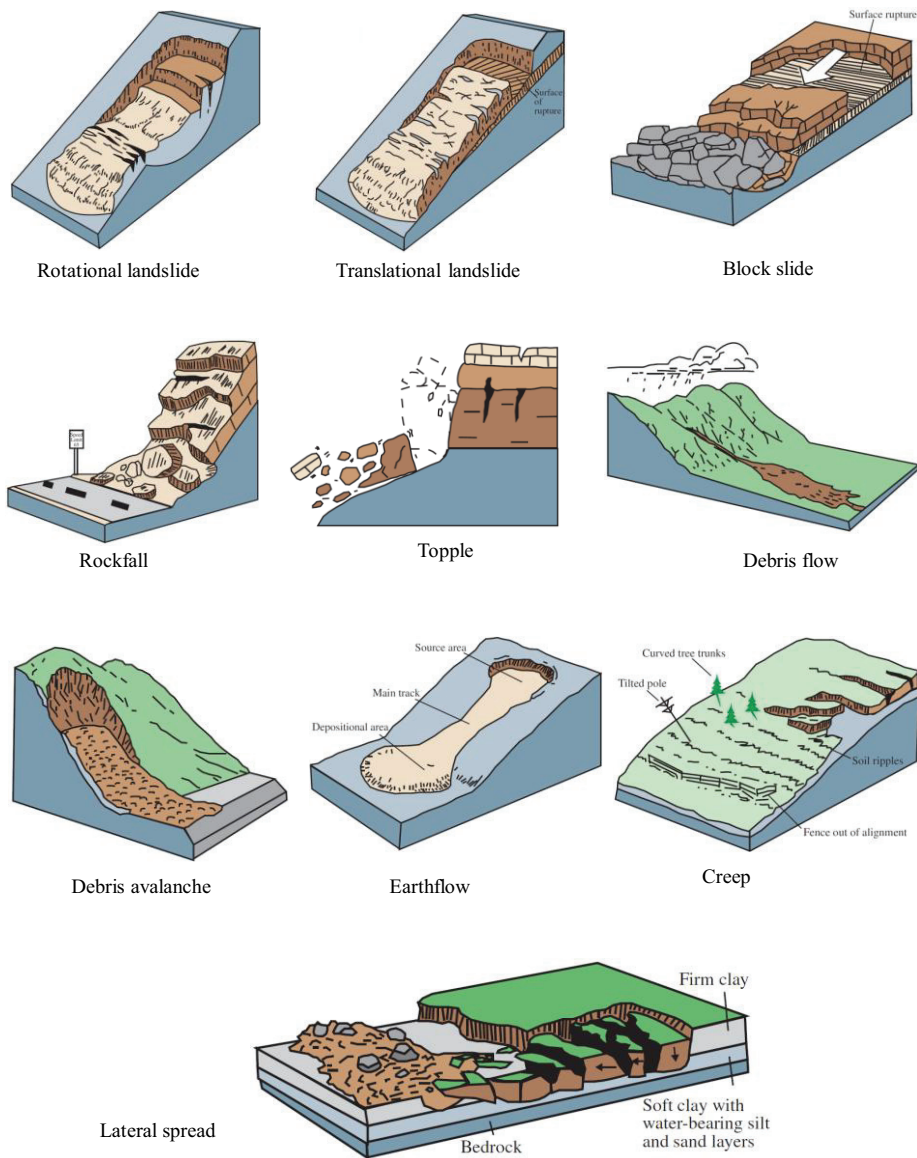


Figure 1.1 Sketches of major types of landslide (U.S. Geological Survey)

But there are some arguments, another researcher used slope failure to term the disaster related with slope. In their opinions, “landslide” is a word composed by “land” and “slide”, the mobile motion of slide does not include toppling, bending, buckling, hence, Aydan (1989, 1991, 2009, 2009a, b) proposed a classification for failure modes of rock slopes, as shown in **Figure 1.2**, then “slope failure” is applied to replace the term of “landslide” in order to express all kinds of disaster related with slope.

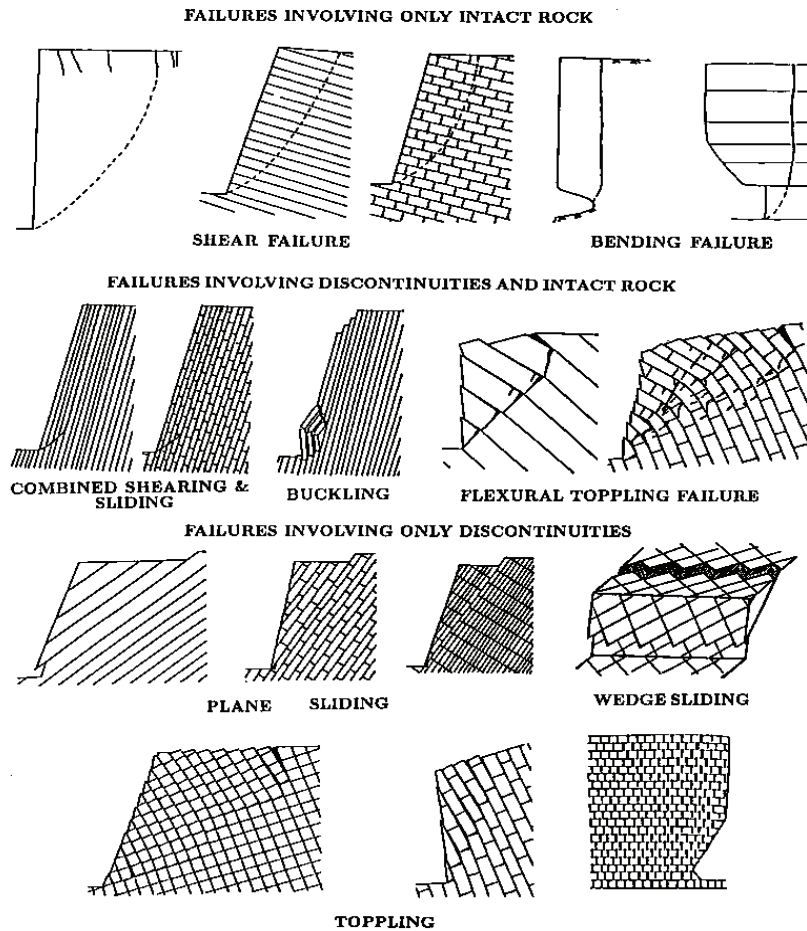


Figure 1.2 Sketches of slope failure (Aydan, et al.1989, 1991)

In a word, the term of “slope failure” includes all types of failure modes related with slope disaster, and “landslide” is a part of “slope failure”, but it also includes many types of failure modes. During Wenchuan earthquake, the disaster related with slope is so widespread that it mostly included all types of failure modes. Therefore, in this thesis, the term of “slope failure” was used in chapter 2, because chapter 2 is from a general viewpoint to analyze the distribution regularity in the whole area affected by Wenchuan earthquake, but in the following part, the term of “landslide” was used in chapter 3 and chapter 4, where did not include all types of slope failure, because the data in these two chapters were collected from rotational landslide, translational landslide, block slide, rock avalanche, debris avalanche, all belonging to “landslide”. Hence, a smaller range of the definition about disasters related with slopes is more suitable in these two chapters.

1.2 Overview of Wenchuan earthquake

1.2.1 Tectonic and geological settings

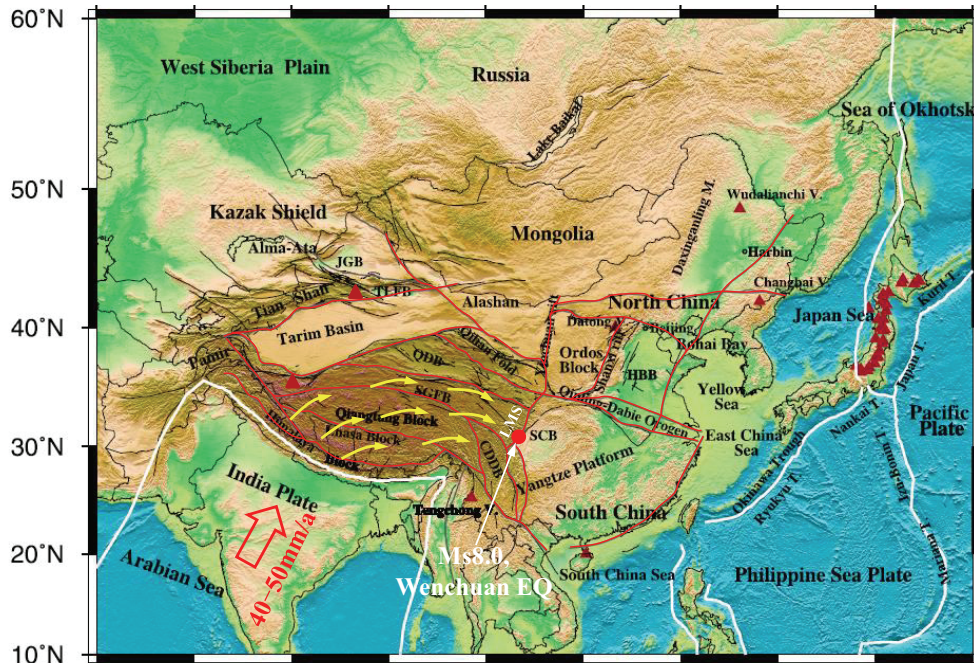


Figure 1.3 Major tectonic and geological settings in and around the China. Color shows the surface topography. White lines show the plate boundaries. Red lines show the large fault zones and/or tectonic block boundaries in mainland China. Brown solid triangles denote volcanoes. Abbreviations are Jungger Basin (JGB), Qaidam Basin (QDB), Sichuan Basin (SCB), Turfan Basin (TLFB), Songpan Ganzi Fold Belt (SGFB), Chuandian Diamond Block (CDDB) and Longmenshan thrust fault zone (LMS). (Modified from Huang and Zhao, 2006)

The structure and tectonics of China are affected by the interaction among three plates: the Pacific, the Philippine Sea and the Indian plates. In the east, the Pacific and the Philippine Sea plates are sub-ducting beneath the Eurasian plate. In the southwest, the India-Asia Plate collides with Eurasian plate at the speed of about 40-50mm/a (Molnar and Tapponnier, 1975; Avouac and Tapponnier, 1993; Dai, et al., 2011), leading to the shortening and elevating the Tibetan Plateau and causing high and great mountain ranges, as shown in **Figure 1.3**. The movement of eastward slip-fault is blocked by Ordos Block and Yangtze Platform, forming a complex fold-thrust

structure with thrust belt and its foreland in the western Sichuan Basin (Deng et al., 1994; Xu, et al. 2008a). The eastern margin of the Tibetan Plateau is composed of three major tectonic units: the Songpan–Ganzi fold belt, the Longmanshan thrust belt, and the Longmenshan foreland basin (Li, et al., 2003). The southeastward extrusion of the Songpan–Ganzi block, which obliquely collides with the foreland basin, results in Longmenshan tectonic boundary between eastern Tibetan Plateau and the Yangtze Platform (Sichuan Basin).

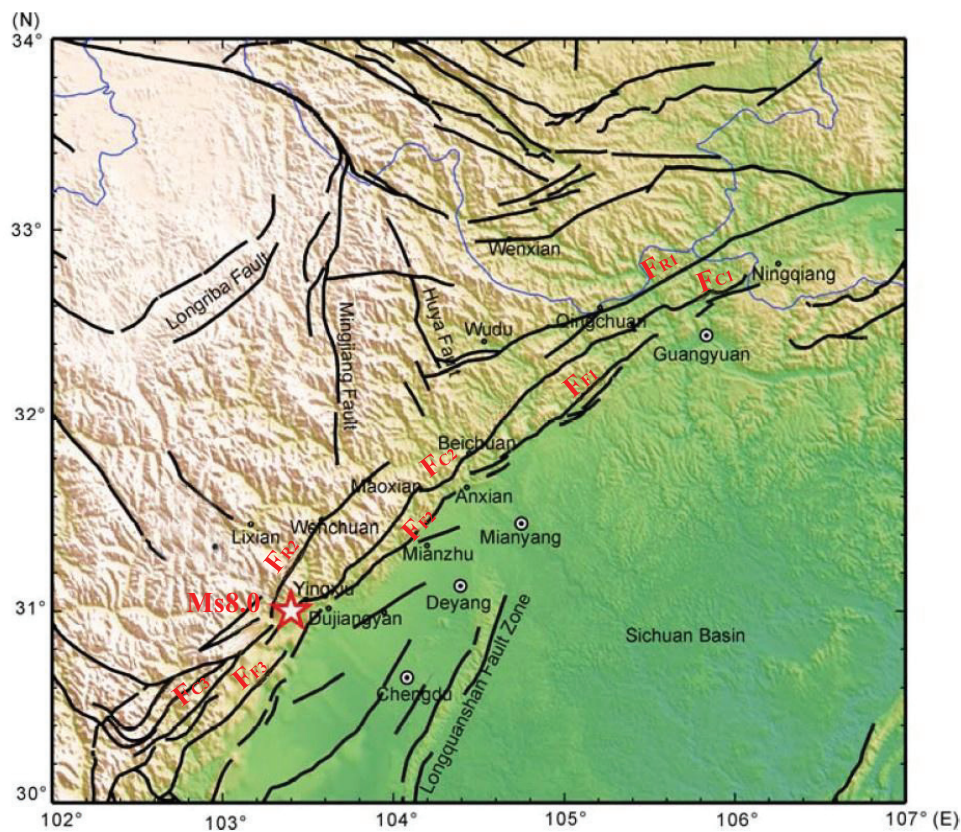


Figure 1.4 Fault system of Longmenshan fault zone; Lines mark fault system and star denotes the epicenter of Ms 8.0 Wenchuan earthquake. F_{R1} , Qingchuan fault; F_{R2} , Wenchuan–Maoxian fault; F_{C1} , Chaba–Linyansi fault; F_{C2} , Yingxiu–Beichuan fault; F_{C3} , Yanjing–Wulong fault; F_{F1} , Jiangyou–Guangyuan fault. F_{F2} , Guanxian–Jiangyou fault; F_{F3} , Shuangshi–Dachuan fault (Based on Zhao, et al., 2010)

At least two major orogenic events occurred in the Longmenshan belt since the Mesozoic: a Late Triassic compressional event (Indosinian orogeny) and a Cenozoic deformation related to the India-Asia collision (Jia, et al., 2010). Longmenshan fault zone represents the features of thrusting and dextral strike-slip in late Cenozoic (Densmore et al., 2007; Li et al., 2003). The dextral strike-slip rate of the Yingxiu–Beichuan fault since the late Pleistocene is less than 1 mm/a, and the thrust rate is 0.3–6 mm/a. The shortening rate across the Longmenshan range is about 3 mm/a based on the estimation of GPS (Shen et al., 2009; Xu et al., 2009a). The length of Longmenshan fault zone is about 500km, width is 40–50km, with N40–50°E strike, and dips to NW direction with 50–75°, which consists of three sub-parallel faults dipping to the west, namely, the Rear-Longmenshan fault, the Central-Longmenshan fault and the Fore-Longmenshan fault, as shown in **Figure 1.4**. (Xu, et al. 2008a, 2009b; Zhao, et al., 2010).

Each fault includes several segments. From north to south, the Rear-Longmenshan fault consists of Qingchuan fault (F_{R1}) and Wenchuan–Maoxian fault (F_{R2}). Qingchuan fault (F_{R1}) is characterized by dextral strike-slip, with N60–70°E strike and northwest dipping; Wenchuan–Maoxian fault trends N25–45°E and dips to the northwest. Since 1597, 13 earthquakes of $M \geq 4$, have been historically attributed to this fault (Zhao, et al., 2010; Dai, et al. 2011).

The Central-Longmenshan fault trends N35–45°E and dips to the northwest, which is composed of the Chaba–Linyansi fault (F_{C1}) in the north, the Yingxiu–Beichuan fault (F_{C2}) in the middle, and the Yanjing–Wulong fault (F_{C3}) in the south (Zhao, et al., 2010). Since 1168, 12 earthquakes of $M \geq 4$ have been noted along this fault, among which the most significant one was the 1958 Beichuan earthquake, $M_{6.2}$ (Dai, et al., 2011).

The Jiangyou–Guangyuan fault (F_{F1}), Guanxian–Jiangyou fault (F_{F2}) and Shuangshi–Dachuan fault (F_{F3}) are the northern, middle and southern segments of the Fore-Longmenshan fault, respectively, which is trending N35–45°E and dipping 50–70° to the northwest. This fault is the eastern edge of the Tibetan Plateau and adjacent to the Sichuan Basin.

Among above mentioned faults, the Yingxiu-Beichuan fault is the largest-scale fault in the Longmenshan thrust fault belt. It cuts to the deep crust and separates sedimentary rock in the shallow crust from the metamorphic rock and magma complex in the middle and deep crust. It is this fault that triggered the $M_{8.0}$ Wenchuan earthquake; the initial rupture point was located nearby Yingxiu town, on the southern end of Yingxiu-Beichuan fault (Zhao, et al., 2010).

Complex thrusting movement causes three dimensional structure of Longmenshan like an imbricate stack (Xu et al., 2008a, 2009b), as shown in **Figure 1.5**. To the south segment of Longmenshan fault, three major reverse faults, Wenchuan-Maoxian fault, Yingxiu-Beichuan fault and Guanxian-Jiangyou fault, and a blind fault under the Sichuan basin accommodate most of the crustal shortening. The Yingxiu-Beichuan fault dips steeply at the surface (dipping $>45^\circ$), and appears to root into a basal detachment in the mid-crust (Burchfiel et al., 1995; Hubbard et al., 2008; Xu et al., 2008b). Guanxian-Jiangyou fault, dipping $20^\circ\text{--}30^\circ$, merges with the Yingxiu-Beichuan fault at depth. To the north, the dip of the Yingxiu-Beichuan fault in the upper crust is steepening (Hubbard et al., 2008; Xu, et al., 2009b).

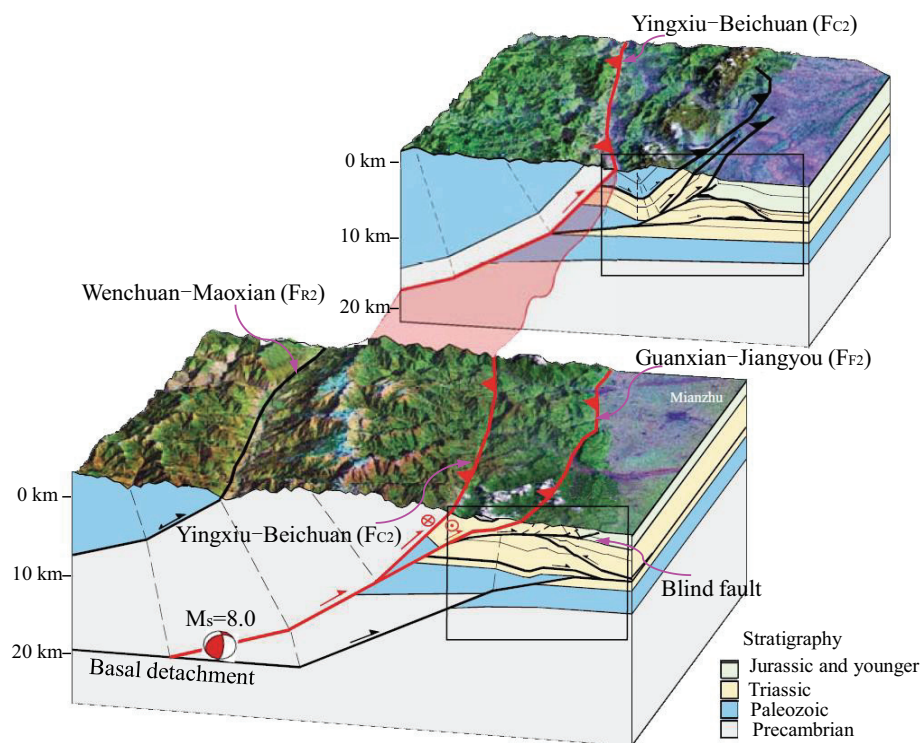


Figure 1.5 3-Dimensional model of the Longmenshan fault (Based on Xu, et al., 2008a, 2009b)

The strata in the earthquake-affected zone include from upper Archean to Quaternary, they are simplified in **Table 1.2** and shown in **Figure 1.6**, which are based on the geochronological sequence. In the southeast of the Longmenshan fault zone, Jurassic and Cretaceous strata are covered by Quaternary alluvium in the Sichuan Basin, and outcrops from Anxian-Jiangyou in the

Sichuan Basin to the northeast of the Longmenshan fault zone. Triassic strata widely disclose in the western of Longmenshan fault zone, such as, Wenchuan, Lixian, Maoxian, Beichuan and Pingwu; meanwhile, there is a stripe of Triassic strata outcrop along the Longmenshan fault, mainly including carbonate rock (i.e. limestone) and clastic rock (i.e. mudstone, fine sandstone and sandy mudstone with silty sandstone). Permian-Devonian strata are sparse to disclose in the severely damaged zone. A metamorphic stratum of Silurian is widely disclosed in Qingchuan County, mainly with marine facies clastic rock, siliceous rock, carbonate rock, flysch and volcanic clastic rock. Ordovician strata and Cambrian strata, with thin-middle thick limestone, black siliceous phyllite, etc., are clustered outcrop in the Longmenshan fault zone with a small area. Sinian strata are mainly disclosed in Qingchuan and Pingwu, and sparsely outcrop in Mianzhu and Maoxian. Archean strata are mainly outcropped in Wenchuan, Dujiangyan, Pengzhou, Shifang, Mianzhu and Lixian. The main shock epicenter was located in a set of migmatized metamorphic rock and migmatite (Qi, et al., 2010, 2011).

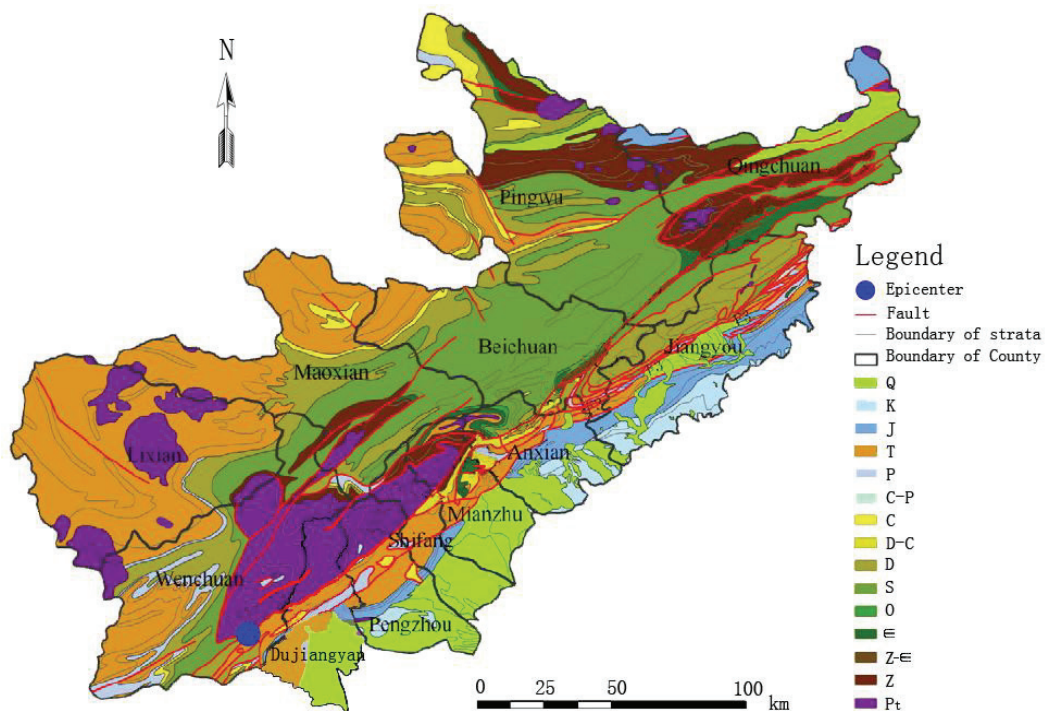


Figure 1.6 Geological formation in the severely damaged area. (Modified from Qi. et al., 2011)

Table 1.2 Symbol and typical lithology of geological formation in Wenchuan earthquake area (Qi, et al., 2011)

Sequence	Symbol	Lithology
Quaternary	Q	Unconsolidated deposit
Cretaceous	K	Conglomerate
Jurassic	J	Sandy slate, mudstone, sandy stone with mudstone
Triassic	T	Sandy stone, limestone, slate
Permian	P	Thick limestone with slate
Carboniferous Permian-	C-P	Limestone, marble with sandy stone
Carboniferous Devonian-	C	Limestone, marble and sandy stone
Carboniferous Devonian	D-C	Carbonate rock, sandy conglomerate
Silurian	D	Quartzose sandstone
Ordovician	S	Sandy stone, phyllite with limestone
Cambrian	O	Limestone, marble and phyllite of Baota formation
Cambrian-Sinian	Є	Metomorphic sandy conglomerate, limestone
Sinian	Z-Є	Metomorphic sandy stone, metamorphic limestone
Archean	Z	Metomorphic sandy stone, metamorphic limestone
	Pt	Granite, diorite, gabbro

1.2.2 Fault surface rupture and seismic intensity

Seismological studies and field surveys both indicated that the epicenter of the main shock was located at the southern section of Yingxiu–Beichuan fault and fault rupture initiated from the southern Longmenshan and propagated unilaterally toward north-northeast for more than 300km, mainly generated about 240km surface rupture along Yingxiu–Beichuan fault and about 72km Hanwang surface rupture along Guanxian-Jiangyou fault, as illustrated in **Figure 1.7**. Between these two main surface fault ruptures, there was a short northwest-striking rupture zone, named Xiaoyudong rupture zone. (Xu, et al. 2008a, 2009b). Co-seismic rupture could be divided into two sub-events. One sub-event between Yingxiu Town and Beichuan Town underwent reverse faulting with minor dextral slip component along Yingxiu-Beichuan fault, while the northeast sub-event between Beichuan Town and Nantou Town primarily exhibited dextral slip (Chen et al., 2008; Xu, et al., 2008a, 2009b; Jia, 2010). Maximum vertical and horizontal offsets along Yingxiu-Beichuan fault were found nearby Yingxiu Town, 6.5 m and 4.9 m, respectively. 3.5m

maximum offset was measured along the Guanxian-Jiangyou fault as maximum displacement in vertical direction (Xu et al., 2008a, 2009b).

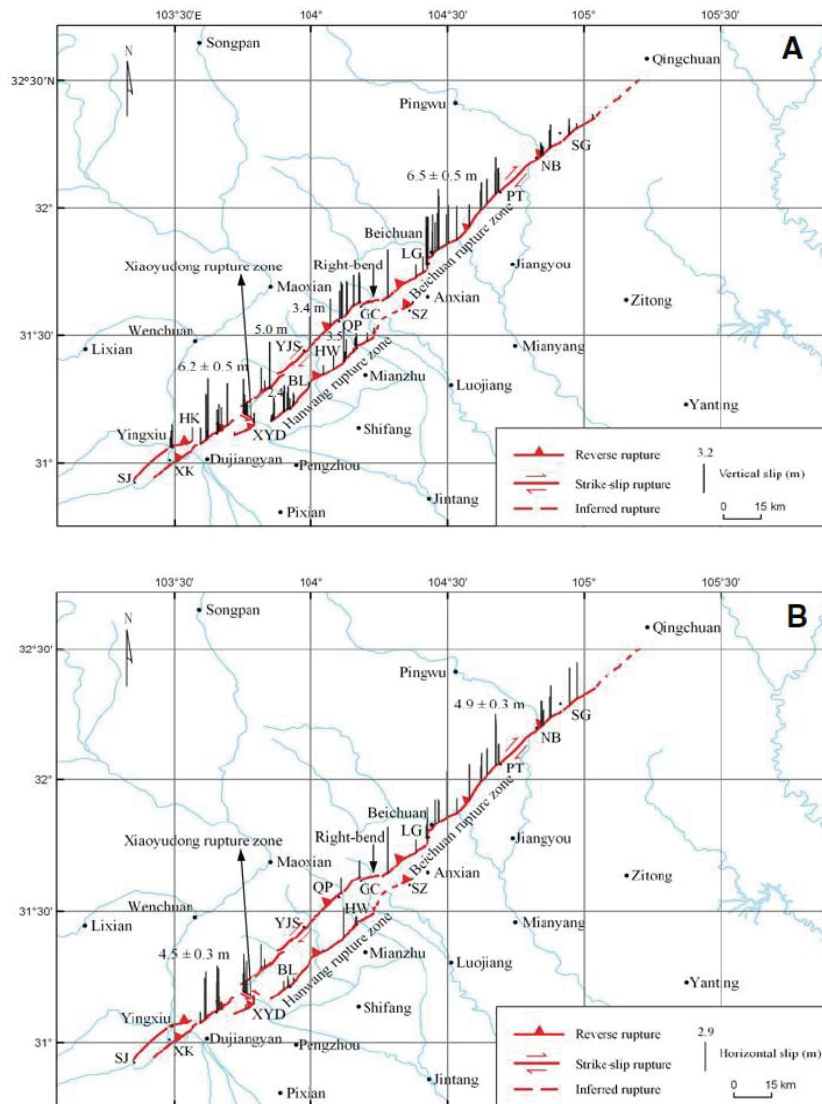


Figure 1.7 Earthquake-induced displacement distribution along surface ruptures; A: vertical offsets; B: Horizontal offsets. GC—Gaochuan Town; QP—Qingping Town; HK—Hongkou Town; SG—Shuiguan Town; SJ—Sanjiang Town; SZ—Sangzao Town; XK—Xuankou Town; YJS—Yuejiashan (Xu, et al., 2008a, 2009b).

Seismic intensity map suggests that XI scale (Chinese Seismic Intensity Scale, CSIS, GB/T17742-1999) area appears like a strip with two polar centers, that is, Yingxiu Town and

Beichuan Town, as shown in **Figure 1.8**. The southwest extreme intensity area, Yingxiu as center, distributed along Wenchuan-Dujiangyan-Pengzhou direction, with about 66km length and 20km width; the northeast extreme intensity area, Beichuan as center, went across Anxian-Beichuan-Pingwu, with about 82km length and 15km width. The total area of XI is about 2419km². X seismic intensity area is about 3144km², appearing a narrow band in north-east direction, with about 224km length and 28km with. The northeast end of X seismic intensity area extended to Qingchuan County, the southwest end stretched to Wenchuan County (China earthquake administration, CAE, 2008).

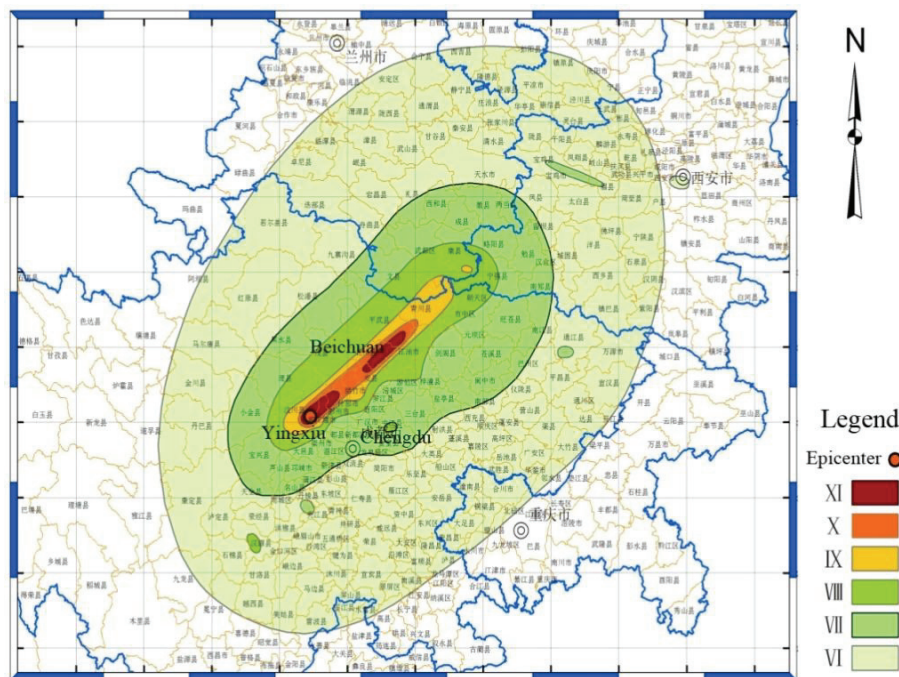


Figure 1.8 Seismic intensity map of 2008 Wenchuan earthquake (Modified from CAE, 2008)

1.2.3 Disasters related with slope failure

The area affected by Wenchuan earthquake is a typically mountainous zone, highest elevation is up to 7500 m above sea level, and its topography varies more than 5 km height within 50 km. The earthquake triggered a large number of slope failures. Huang and Li (2009a,b) indentified 11,300 landslides based on air photos and satellite images. Gorum et al. (2011) interpreted 60,104

slope failures; latest research reveals that there were 197,481 slope failures (Xu, et al., 2013a, b). Some of these slope failures formed landslide dams in the rivers, at least 257 landslide dams in the earthquake-hit region, which had high potential to develop into secondary hazard due to the subsequent flooding (Cui, et al., 2009)

Slope failure was the most representative geo-hazard during Wenchuan earthquake, which caused one third of the estimated casualties (Chen, et al., 2008; Wang et al., 2009). Some of these catastrophic slope failures are listed in the **Table 1.3**, and **Figure 1.9** illustrates three representatively catastrophic landslides.

Table 1.3 The summary of 31 catastrophic slope failures

No.	Slope failures	Location	Volume (10^4m^3)	Casualties	Economic loss (10^4RMB)
1	Wangjiayan	Zhouqu Town, Beichuan County	1000	1600	1600
2	Yingtaogou	Chenjiaba Town, Beichuan County	188	906	1500
3	Jingjiashan	Zhoushan Town, Beichuan County	1000	700	1200
4	Chenjiabachang No.1	Chenjiaba Town, Beichuan County	1200	400	500
5	Donghekou	Hongguang Town, Qingchuan County	1000	260	5000
6	Hongyan Village	Chenjiaba Town, Beichuan County	480	141	120
7	Liming Village	Zipingpu Town, Dujiangyan City	20	120	500
8	Xiejiadian	Jiufeng Village, Pengzhou City	400	100	4000
9	Xiaolongchi	Yinchangou, Pengzhou City	5.4	100	8000
10	Dalongchi	Yinchangou, Pengzhou City	10	100	8000
11	Taihong Village No.2	Chenjiaba Town, Beichuan County	500	100	110
12	Taian No.9 Village	Qingchengshan Town, Dujiangyan City	120	62	800
13	Zhenjiashan	Nanba Town, Pingwu County	1250	60	5000
14	Hanjiashan	Guixi Town, Beichuan County	30	50	130
15	Dayanke	Quhe Town, Qingchuan County	70	41	200
16	Ma'anshi	Shuiguan Town, Pingwu County	400	34	8000
17	Liangaiping	Tuanshan Village, Pengzhou City	40	30	800
18	Mayanzi	Nanba Town, Pingwu County	800	23	60000
19	Huilonggou	Longmenshan Town, Pengzhou County	100	20	12000

No.	Slope failures	Location	Volume (10^4m^3)	Casualties	Economic loss (10^4RMB)
20	Maerping	Quhe Town, Qingchuan County	40	19	50-60
21	Niujuangou	Yingxiu Town, Wenchuan County	100	18	-
22	Zhaojiafen	Nanba Town, Pingwu County	1250	17	-
23	Jiulonggou	Sanlang Town, Chouzhou City	0.5	13	90000
24	Yaogoushe	Nanba Town, Pingwu County	720	11	-
25	Guihuashu No.1	Longchi Town, Dujiangyan City	11	11	120
26	Shaba	Mianchi Town, Wenchuan County	6.51	10	186
27	Yanmengou	Yanmen Town, Wenchuan County	10	10	-
28	Caoping Village	Sanjiang Town, Wenchuan County	100	10	-
29	Niushidun	Keku Town, Wenchuan County	8	10	1000
30	Wenjiaba	Nanba Town, Pingwu County	300	10	10000
31	Shazipo No.1	Longchi Town, Dujiangyan City	11	10	250
Total Casualties				4996	



Figure 1.9 Typically catastrophic landslides (Source from Huang, R.Q.)

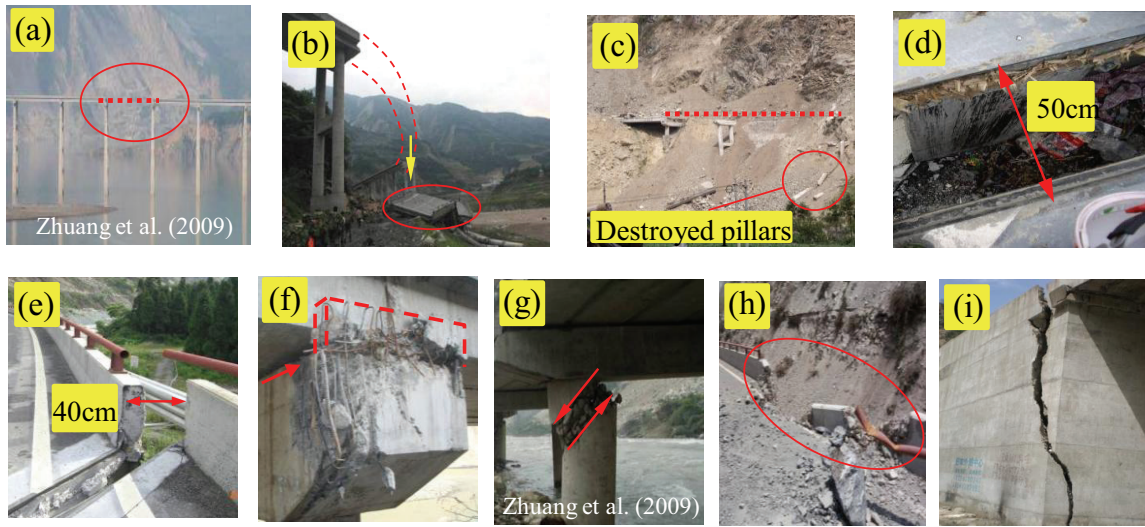


Figure 1.10 Typical seismic damages of bridges during Wenchuan earthquake

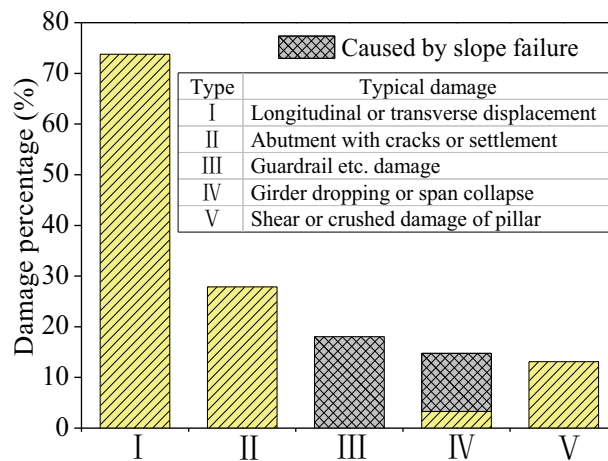


Figure 1.11 Statistics of bridge seismic damages along Road213 and Du-Wen expressway

There were 61 bridges located along National Road 213 and Dujiangyan–Wenchuan expressway, most of these bridges suffered different patterns of seismic damage except 4 bridges with slight destruction. According to damage scales and patterns, seismic damages of bridge were classified into five types: girder dropping or span collapse (**Figure 1.10 a~c**); longitudinal or transverse displacement (**Figure 1.10 d~f**); shear or crushed damage of pillar (**Figure 1.10 g**); guardrail etc. damaged by slope failure (**Figure 1.10 h**); abutment with cracks or settlement (**Figure 1.10 i**). **Figure 11** suggests that 74% out of 61 investigated bridge damages were caused

by girder displacement; meanwhile, damages of guardrail were completely destroyed by slope failures, and most of the girder dropping or span collapse were attributable to slope failure.

Various patterns of tunnel damages were observed in 18 tunnels along National Road 213 and Dujiangyan–Wenchuan expressway, such as, portal failure (Figure 1.12 a~d), lining crack (Figure 1.12 e and f), lining shear failure (Figure 1.12 g), groundwater permeation (Figure 1.12 h) and pavement fissures or uplift (Figure 1.12 i). The statistical analysis suggests that portal failure was the most widespread damage, furthermore, the portal failure was mainly triggered by slope failure, as shown in Figure 1.13.

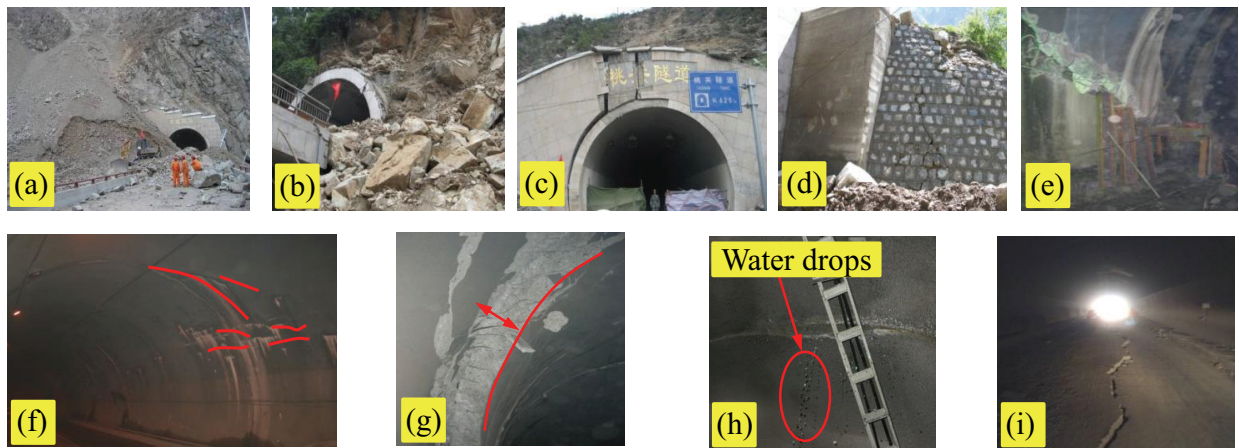


Figure 1.12 Typical seismic damages of tunnels during Wenchuan earthquake

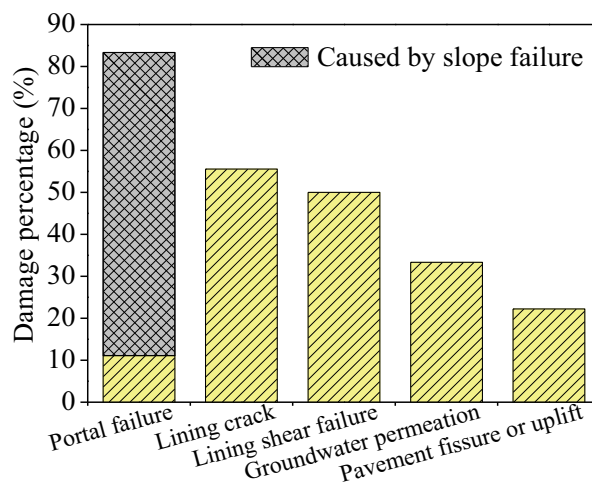


Figure 1.13 Statistics of tunnel seismic damages along Road213 and Du-Wen expressway

1.3 Reviews of previous researches

1.3.1 Researches on slope failure distribution related with seismic parameters

The Ms8.0 Wenchuan earthquake occurred at Yingxiu–Beichuan thrust fault, in Sichuan province, southwest China, on May 12th 2008. This catastrophic earthquake triggered an unprecedented amount of slope failures in Chinese history. It put forward a great challenge to mitigate geo-hazard caused by earthquake-induced slope failures, meanwhile, providing a large amount of data to explore the regularity of slope failure distribution and the relations between slope failure and seismic parameters. However, there are only a few studies combining seismic ground motion with slope failure distribution. Based on statistical combination analysis on 3000 slope failures and strong motion station records of 40 seismic stations related with disaster susceptibility map, Wang et al. (2010a,b) only qualitatively proposed that 0.05g–0.07g tri-component PGA was the threshold value of slope failure occurrence and when tri-component PGA exceeded 0.2g, slope failures were widely induced.

From the global viewpoint, there are also limited studies on quantitative relation between slope failure distribution and seismic ground motion. Keefer (1984) firstly delivered empirical upper bound lines for the relations between earthquake magnitude and total area affected by landslides, maximum distance from epicenter or from fault rupture zone. Rodríguez et al. (1999) extended the work of Keefer (1984) from 1811-1980 to 1997, however, their results were very similar to those proposed by Keefer (1984) and they also just presented upper bound lines. Hancox et al. (1997, 2002) proposed a quantitative relationship between earthquake magnitude and total area affected by landslides based on New Zealand data. Papadopoulos and Plessa (2000) presented a straight-line upper bound for maximum epicentral distance to landslides related with earthquake magnitude based on Greek data. Keefer (2002) globally reviewed landslides induced by earthquake and proposed an empirically quantitative relation between earthquake magnitude and total area affected by landslides. More recently, besides the empirical bounds of Keefer (1984), Aydan (2007, 2009, 2009c) proposed an empirical equation for the maximum distance of disrupted and coherent landslides as a function of earthquake magnitude and fault orientation; Meunier et al. (2007) firstly analyzed the relation between landslide distribution and seismic ground motion, and proposed an empirical model for predicting landslide distribution density,

which took distance from hypocenter as variable. Delgado et al. (2011) summarized 270 earthquakes to analyze the relation between maximum epicentral distance to landslides and earthquake magnitude. Based on above brief review, there are limited studies on the quantitative relationship between slope failure distribution and seismic ground motion. Therefore, this issue of Wenchuan earthquake will be discussed in chapter 2.

1.3.2 Researches on influential factors of slope stability and dynamic responses

In many previous studies about landslide triggered by Wenchuan earthquake, their focus was on the qualitative tendency between landslide spatial distribution and influential factors, such as seismic factors (earthquake magnitude, epicentral distance, distance from surface fault rupture and intensity), geomorphologic factors (elevation, slope gradient, slope height and slope aspect) and geological factors (lithology and geological structure). Huang and Li (2009a, b) studied the distribution of 11,300 landslides what they called “geo-hazards” triggered by the earthquake. Yin et al. (2009) analyzed the distribution of earthquake-induced landslides and the characteristics and failure mechanism of some typical landslides, and assessed the risks caused by some of the landslide dams. Sato and Harp (2009) carried out a preliminary study on landslide interpretation by using pre-earthquake and post-earthquake FORMOSAT-2 imageries. Wang et al. (2009) presented preliminary investigation results of some large landslides triggered by the earthquake. Xu et al. (2009c, 2010) interpreted 48,007 landslides and researched the influence of each triggering factor on landslide distribution. Qi, et al. (2010) made use of 13,085 landslides within 11 severely damaged counties to analyze the correlations between landslide distribution and influential factors. Chigira, et al. (2010) studied the correlation between slope failed modes and lithology. Gorum et al., (2011) mapped about 60,000 landslides by satellite images and analyzed landslide distribution related with influential factors. Dai et al. (2011) interpreted over 56,000 landslides to discuss the types and spatial distribution of landslides. Xu et al. (2013a, b) interpreted a most detailed landslide inventory, which includes more than 197,000 slope failures triggered by Wenchuan earthquake, and statistically analyzed slope failure spatial distribution related with influential factors. Based on above brief review, section 3.2 in chapter 3 will firstly follow previous research methodology to study the general trend of landslide distribution related

with influential factors in Wenchuan County, and further comprehensively discuss the effectiveness of each influential factor on slope stability.

The interaction between seismic waves with slope plays a major role in slope stability during earthquakes. Methods for assessing slope stability or performance during earthquakes have evolved steadily since the early twentieth century, which generally fall into three categories: (1) pseudo-static analysis (Terzaghi, 1950), (2) finite element modeling, a type of stress-deformation analysis (Clough, 1960; Clough and Chopra, 1966), and (3) permanent-displacement analysis (Newmark, 1965). Pseudo-static analysis models the seismic shaking as a permanent body force that is added to the force-body diagram of a conventional static limit-equilibrium analysis; normally, only the horizontal component of earthquake shaking is modeled and considered by pseudo-static coefficient. It is conceptually simple, but the process of selecting a seismic coefficient commonly lacks a rational basis, and the analysis tends to be over-conservative. Stress-deformation analysis is more sophisticated, but it is too complex and expensive to be applied during routine application, as a result of requiring sufficient data to merit it. Permanent-displacement greatly bridges the gap between overly simplistic pseudo-static analysis and overly complex stress-deformation analysis. Great efforts were widely contributed to improve these analyzing methods, but all of these slope stability analysis methods have not demonstrated the effects of numerous influential factors on slope stability. Recently, Qi (2006) applied dimensional analysis method to research the dynamic responses of single surface slope. Shi et al. (2008) derived the analytic solution of the elevation amplification effect on a single surface slope and discussed the influential factors on dynamic responses. Luo et al. (2010) proposed a criterion to check the seismic stability of layer rock slope. Other researches (Martino and Mugnozza, 2005; Sepulveda et al., 2005a,b; Bourdeau and Havenith, 2008; Danneels et al., 2008) suggested that slope stability and triggering conditions relied on seismic input properties, such as energy, frequency content and peak ground acceleration (PGA). Nevertheless, there are few studies to fully explore the influences of geomechanical parameters and seismic wave parameters on slope dynamic response; hence, this issue will be discussed in section 3.3 in chapter 3.

The effects of topography on slope stability during earthquakes, such as ridges and canyons, have been researched by several authors (Sanchez-Sesma and Rosenblueth, 1979; Geli et al., 1988; Athanasopoulos et al., 1999). There are some studies on the dynamic responses of step-like slope by using numerical modeling, for example, Ashford et al. (1997), Bouckovalas and

Papadimitriou (2005), Nguyen and Gatmiri (2007), Lenti and Martino (2012). However, the studies about the effects of different slope shapes on dynamic responses are still limited, therefore, section 3.4 in chapter 3 applied finite element method to research dynamic responses of five simplified slopes with different shapes.

1.3.3 Researches on landslide mobility

The discussions for landslide mobility and debris flow mobility have been given, for example, Hungr (1995), Corominas (1996), Okura, et al. (2000a, 2003), Fannin and Wise (2001), Legeros (2002), Hunter and Fell (2003), Berti and Simoni (2007), Hattanji and Moriwaki (2009, 2011), D'Agostino et al. (2010), Tang et al. (2012) and Pudasaini and Miller (2013). A well-known index expressing the mobility of landslide is the angle of the line connecting the crest of the landslide source to the distal margin of the deposited mass; this angle was firstly named as the *fahrböschung* (Heim, 1932). Shreve (1968) and Scheidegger (1973) later named tangent of this angle as equivalent coefficient of friction, and followed by angle of reach (Corominas, 1996), travel distance angle (Hunter and Fell, 2003). A number of authors discussed the relationship between equivalent coefficient of friction and sliding volume (Scheidegger, 1973; Hsü, 1975; Corominas, 1996; Legros, 2002; Okura et al., 2000b, 2003), and proposed that equivalent coefficient of friction shown a decreasing trend with the increment of landslide volume. Other authors, such as Hunter and Fell (2003), Okura et al. (2000a, 2003), Hattanji and Moriwaki (2009), revealed a positive correlation between equivalent coefficient of friction and slope angle. Corominas (1996) proposed that the relative excess of travel distance was more suitable than “excessive travel distance”, proposed by Hsü (1975), to express the degree of landslide mobility. Aydan and Shimizu (1993) experimentally explored the effects of slope height, slope angle, frictional properties of the basal surface and failure modes on landslide mobility. Recent statistical analyses ensured the effect of topography on the landslide mobility of constructed and natural slopes (Hunter and Fell, 2003; Hattanji and Moriwaki, 2009; Fan and Qiao, 2010). However, most of these studies were limited to discuss non-seismically induced landslide; it needs to be further explored whether the mobility of earthquake-induced landslide is consistent with previous studies of non-seismically induced landslide. Furthermore, most of these authors either just qualitatively discussed several influential factors on landslide mobility or just

quantitatively analyzed landslide mobility related with very few influential factors, such as landslide mobility related with landslide volume or slope angle. In fact, landslide mobility was affected by numerous factors simultaneously, such as slope angle, slope height, slope transition angle, landslide volume, rock type, and so on. It is necessary to develop a new model to fully and comprehensively consider all of these influences. Hence, landslide mobility will be discussed in section 4.4 and 4.5 of chapter 4, which is based on 46 well-documented landslides with relatively long travel distance from remote sensing interpretation, field investigation and published literatures.

1.3.4 Researches on landslide travel distance

As a first approximation, the debris flow runout, length between apex of deposit fan and the distal, had been proposed that this distance could be related to event volume and deposit geometry (VanDine, 1996; Lo, 2000). Vandre (1985) summarized an empirical relation between runout distance of debris flow and elevation loss (D'Agostino, et al., 2010). Ikeya (1981, 1989) developed empirical relationships to estimate debris flow runout length from event volume and channel slope. Rickenmann (1999) proposed an empirical equation to relate the horizontal travel distance (L_{max}) of debris flow with its volume (V) and maximum elevation loss (H_{max}). Finlay et al. (1999) made use of multiple regression method to propose a model for the prediction of travel distance based on over 1100 man-modified slopes in Hong Kong. Fannin and Wise (2001) stated that the initial volume of a debris flow and the rate at which material is entrained or deposited along its travel path could be used to estimate the total travel distance. More recently, Tsukamoto et al. (2006) presented a form of simple charts to evaluate the runout distance of landslide, in which the runout distance is expressed as a function of relevant geometrical parameters and residual shear strength of soils. Kokusho et al. (2007) applied energy approach to discuss the slope displacement depended on shaking model table test and further analyze the travel distance during 2004 Chuetsu earthquake (Kokusho et al., 2009). Prochaska et al. (2008) developed a model that provided runout prediction based on the average channel slope for non-volcanic debris flows which emanate from confined channels and deposit on well-defined alluvial fans. Qi et al. (2011) delineated six typical destructive long travel landslides and listed 66 valuable cases caused by the 2008 Wenchuan earthquake, but limitedly analyzed the relationship between elevation loss

& sliding area and travel distance. Tang et al. (2012) established an empirical model to estimate the maximum runout distance and the width of debris flow in Wenchuan earthquake area.

Other ways to estimate runout or travel distance of landslide are theoretical model and numerical simulation model. A commonly advocated theoretical model to calculate landslide runout is the leading-edge model (Takahashi, 1981; VanDine, 1996; Lo, 2000), which requires two parameters that are difficult to be accurately estimated, namely, the velocity of sliding mass and the frictional parameter. Numerical simulation model treats the failure mass as either continuum element (O'Brien et al., 1993; Hungr, 1995; McArdell et al., 2007) or distinct element (Asmar et al., 2003; González et al., 2003). Although, numerical simulation model provides additional information, such as velocity of sliding mass and endangered area, they need the most sophisticated data to yield accurate runout or travel distance; Since the parameters of a landslide may change during movement, in order to avoid the usage of uncertainly and highly variable input parameters to predict landslide travel distance, empirical model was widely applied to preliminary assessment of landslide travel distance, as a result of no requirement of the parameters of rheology or detail mechanics of movement, besides, it is a relatively simple tool to offer a practical means of prediction. Hence, there are lots of previous researches to use this approach, such as, Scheidegger, 1973; Corominas, 1996; Fannin and Wise, 2001; Hunter and Fell, 2003; Okura et al, 2003; Berti and Simoni, 2007; Prochaska et al, 2008; Hattanji and Moriwaki, 2009, 2011.

Based on above brief review, landslide travel distance is an active research topic, but there exists some difficulties, i.e. variations of some models are difficult to be collected or the cost of accessing the data may not be economical for preliminary hazard assessment, meanwhile, some existing empirical models have not enough considered the influential factors on landslide travel distance, for example, the model proposed by Rickenmann (1999). Therefore, this issue will be further discussed in section 4.3 and 4.6 of chapter 4.

1.4 Research objectives and procedures

Based on above reviews of previous researches and disasters induced by the 2008 Wenchuan earthquake, this thesis has researched the following five aspects:

1. The relationship between slope failure distribution and seismic parameters, and slope failure distribution attenuation model.
2. The general tendency of landslide distribution related with influential factors and the effectiveness of various influential factors on slope stability and its dynamic responses.
3. The effectiveness of influential factors on landslide mobility and its prediction.
4. The effectiveness of influential factors on landslide travel distance and its prediction.
5. Seismic performance of slope countermeasures.

In order to study on the distribution of slope failure related with seismic parameters and influential factors on slope stability and landslide mobility, this thesis used a series of methodologies, such as statistical analysis and comparison analysis, finite element simulation and theoretical derivation. The research aspects included whole viewpoint and local viewpoint, qualitative analysis and quantitative analysis, numerical simulation and in-situ investigation. The whole research procedure obeyed a process of a slope from stability to instability, from the estimation of mobile ability of sliding debris to the prediction of its travel distance, and then investigated slope countermeasures so as to effectively mitigate natural slope from failure in the future. The topic of each chapter is following:

Firstly, chapter 1 introduced the research background, which briefly delineated the causes and results of Wenchuan earthquake, and reviewed previous researches on slope failure distribution related with earthquake parameters, slope stability and landslide mobility.

Secondly, from the whole viewpoint of Wenchuan earthquake affected area, chapter 2 applied a detailed inventory with more than 190,000 slope failures and strong ground motion records of 187 seismic stations to analyze the qualitative and quantitative relations between slope failure distribution and seismic ground motion, and slope failure distribution attenuation was further discussed.

Thirdly, three kinds of methodologies were used to analyze the numerous influential factors on slope stability in chapter 3. In section 3.2, 119 landslides, in-situ investigated in Wenchuan County, were used to analyze the effects of slope angle, slope height, peak ground acceleration, geological structure, rock type on slope stability; In section 3.3, theoretical deviation was applied to study the influences of geomechanical parameters and seismic parameters on dynamic responses of a slope with singly and linearly inclined surface; finite element simulation was

conducted to research the effect of slope geometrical shape on slope stability and dynamic responses in section 3.4.

Fourthly, the chapter 4 studied the landslide mobility and travel distance, where qualitative and quantitative analyses were implemented to research the effectiveness of influential factors on landslide mobility and travel distance according to 46 landslides with relatively long travel distance in Wenchuan earthquake area.

Fifthly, Seismic performances of four slope reinforcements were compared in chapter 5 based on the field investigation, so as to explore their reinforcement mechanics and abilities.

Finally, the chapter 6 summarized the findings in this research and discussed the future research topics.

The research flow chart and graphic abstract are shown in **Figure 1.14**.

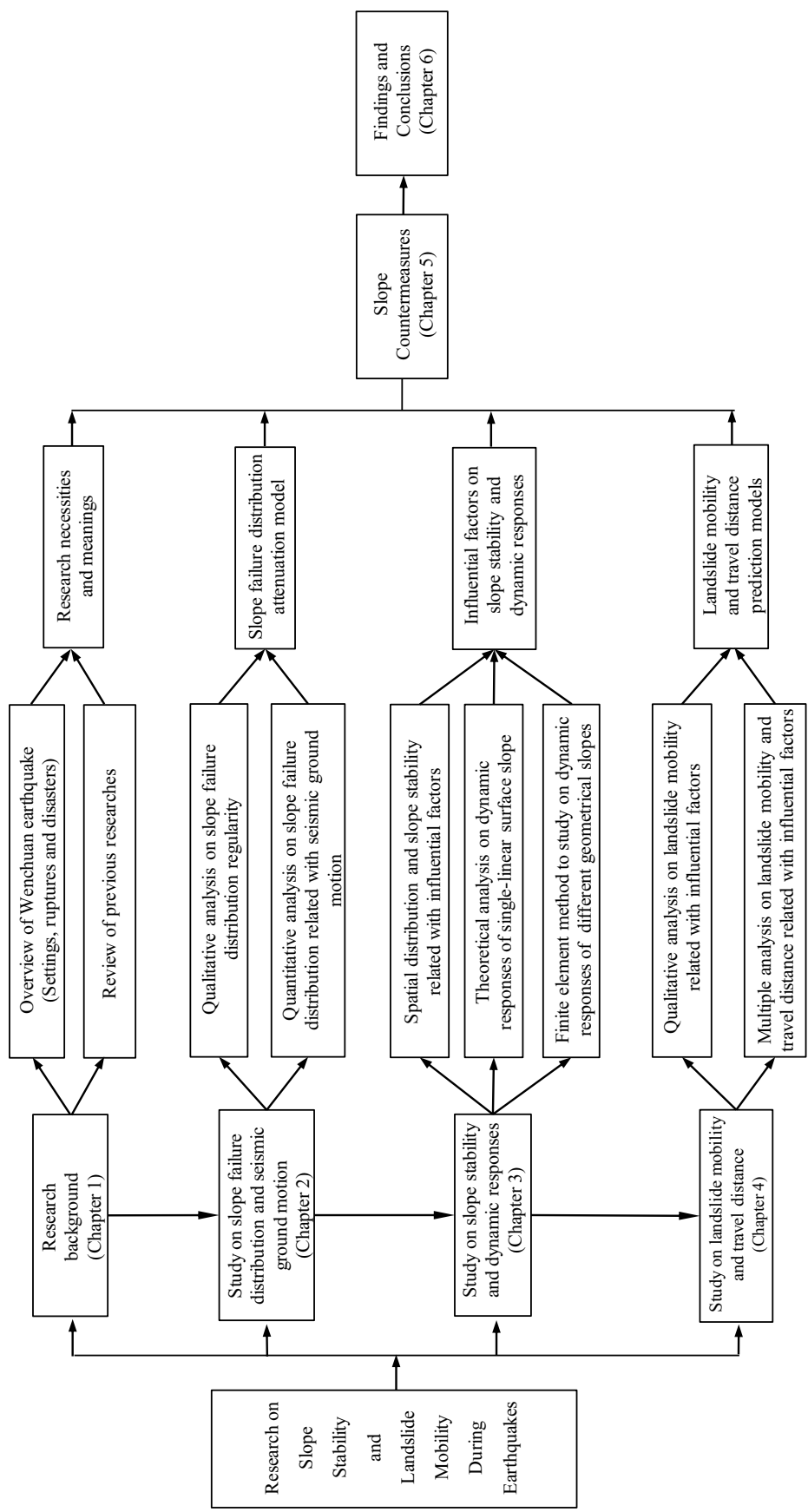


Figure 1.14 Research flow chart and graphic abstract

References

- Aydan, Ö., 1989. The stabilization of rock engineering structures by rockbolts. Doctorate thesis, Nagoya University, 204pages.
- Aydan Ö., Ichikawa, Y., Shimizu, Y., 1991. An integrated system for the stability of rock slopes. Proceedings of the Seventh International Conference on Computer Methods and Advances in Geomechanics, 469–474.
- Avouac, J.P. and Tapponnier, P., 1993. Kinematic model of active deformation in Central Asia. Geophysical research letters, 20(10), 895–898.
- Aydan, Ö. and Shimizu, Y., 1993. Post-failure motions of rock slopes. Proceedings of the International Symposium on Assessment and Prevention of Failure Phenomena in Rock Engineering.
- Ashford, S.A., Sitar, N., Lysmer, J., et al., 1997. Topographic effects on the seismic response of steep slopes. Bulletin of the Seismological Society of America, 87, 701–709.
- Athanasopoulos, G.A., Pelekis, P.C., Leonidou, E.A., 1999. Effects of surface topography on seismic ground response in the Egion (Greece) 15 June 1995 earthquake. Soil Dynamics and Earthquake Engineering, 18, 135–149.
- Asmar, B.N., Langston, P.A., Ergenzinger, P., 2003. The potential of the discrete element method to simulate debris flow. In: Rickenmann, D., Chen, C.-L. (Eds.), Abstract.
- Aydan, Ö., 2007. The inference of seismic and strong motion characteristics of earthquakes from faults with a particular emphasis on Turkish earthquakes. The 6th national earthquake engineering conference of Turkey, Istanbul, 563–574.
- Aydan, Ö., 2009. Characteristics of large scale rock slope failures induced by recent worldwide earthquakes. 12th International Conference on Soil Mechanics Geotechnical Engineering.
- Aydan, Ö., Ohta, Y., Hamada, M., et al., 2009a. The characteristics of the 2008 Wenchuan earthquake disaster with a special emphasis on rock slope failures, quake lakes and damage to tunnels, Journal of the School of Marine Science and Technology, Tokai University, 7(2), 1–23.

- Aydan, Ö., Hamada, M., Itoh, J. et al., 2009b. Damage to civil engineering structures with an emphasis on rock slope failures and tunnel damage induced by the 2008 Wenchuan earthquake. *Journal of Disaster Research*, 4(2), 153–164.
- Aydan, Ö., Ohta, Y., Hamada, M., 2009c. Geotechnical evaluation of slope and ground failures during the 8 October 2005 Muzaffarabad earthquake, Pakistan. *Journal of Seismology*, 13(3), 399–413.
- Burchfiel, B.C., Chen, Z., Liu, Y., et al., 1995, Tectonics of the Longmen Shan and adjacent regions, Central China. *International Geology Review*, 37, 661–738.
- Berti, M., Simoni, A., 2007. Prediction of debris flow inundation areas using empirical mobility relationships. *Geomorphology*, 90, 144–161.
- Bouckovalas, G.D. and Papadimitriou, A.G., 2005. Numerical evaluation of slope topography effects on seismic ground motion. *Soil Dynamics and Earthquake Engineering*, 25, 547–558.
- Bourdeau, C., Havenith, H.B., 2008. Site effects modeling applied to the slope affected by the Suusamyr earthquake (Kyrgyzstan, 1992). *Engineering Geology*, 97, 126–145.
- Clough, R.W., 1960. The finite element method in plane stress analysis. *Proceedings of the 2nd Conference on Electronic Computation*. American Society of Civil Engineers, Structural Division, Pittsburgh, PA.
- Clough, R.W., Chopra, A.K., 1966. Earthquake stress analysis in earth dams. *ASCE Journal of the Engineering Mechanics Division* 92, 197–211.
- Cruden, D.M., 1991. A Simple Definition of a Landslide. *Bulletin of the International Association of Engineering Geology*, 43, 27–29.
- Cruden, D.M., Varnes, D.J., 1996. Landslide types and processes. In special report 247: *Landslides: Investigation and Mitigation*, Transportation Research Board, Washington D.C.
- Corominas, J., 1996. The angle of reach as a mobility index for small and larger landslides. *Canadian Geotechnical Journal*, 33, 260–271.
- Chen, Y., Li, L., Li, J., et al., 2008. Wenchuan earthquake: way of thing is changed. *Episodes*, 31 (4), 374–377.
- Cui, P., Zhu, Y.Y., Han, Y.S., et al., 2009. The 12 May Wenchuan earthquake-induced landslide lakes: distribution and preliminary risk evaluation. *Landslides* 6, 209–223.
- Chigira, M., Wu, X.Y., Inokuchi, T., et al., 2010. Landslides induced by the 2008 Wenchuan earthquake, Sichuan, China. *Geomorphology*, 118, 225–238.

- Deng, Q.D., Chen, S.F., Zhao, X.L., 1994. Tectonics, seismicity and dynamics of Longmenshan Mountains and its adjacent regions. *Seismology and Geology*, 16(4), 389-403. (In Chinese with English abstract)
- Densmore, A.L., Ellis, M.A., Li, Y., Zhou, R., Hancock, G.S., Richardson, N., 2007. Active tectonics of the Beichuan and Pengguan fault at the eastern margin of the Tibetan Plateau. *Tectonics*, 26, TC4005.
- Danneels, G., Bourdeau, C., Torgoev, I., Havenith, H.B., 2008. Geophysical investigation and dynamic modelling of unstable slopes: case-study of Kainama (Kyrgyzstan). *Geophysical Journal International*, 175 (1), 17–34.
- D'Agostino, V., Cesca, M., Marchi, L., 2010. Field and laboratory investigations of runout distances of debris flows in the Dolomites (Eastern Italian Alps). *Geomorphology*, 115, 294–304.
- Delgado, J., Garrido, J., López-Casado, C., et al., 2011. On far field occurrence of seismically induced landslides. *Engineering Geology*, 123, 204–213.
- Dai, F.C., Xu, C., Yao, X., et al., 2011. Spatial distribution of landslides triggered by the 2008 Ms 8.0 Wenchuan earthquake. *Journal of Asian Earth Sciences*, 10, 883–895.
- Finlay, P.J., Mostyn, G.R., Fell, R., 1999. Landslide risk assessment: prediction of travel distance. *Canadian Geotechnical Journal*, 36, 556–562.
- Fannin, R.J., Wise, M.P., 2001. An empirical-statistical model for debris flow travel distance. *Canadian Geotechnical Journal*, 38, 982–994.
- Fan, X.Y., Qiao, J.P., 2010. Influence of landslide and ground factors on large-scale landslide movement. *Chinese Journal of Rock Mechanics and Engineering*, 29(11), 2337–2347. (In Chinese with English abstract).
- Geli, L., Bard, P.Y., Jullien, B., 1988. The effect of topography on earthquake ground motion: a review and new results. *Bulletin of the Seismological Society of America*, 78, 42–63.
- González, E., Herreros, M.I., Pastor, M., Quecedo, M., Fernández Merodo, J.A., 2003. Discrete and continuum approaches for fast landslide modeling. In: Konietzky, H. (Ed.), *Numerical Modeling in Micromechanics via Particle Methods*, Proceedings of the 1st International PFC Symposium, Gelsenkirchen. Lisse, AA Balkema, 307–313.

- Gorum, T., Fan, X.M., Westen, C.J., et al., 2011. Distribution pattern of earthquake-induced landslides triggered by the 12 May 2008 Wenchuan earthquake, *Geomorphology*, 133, 152–167.
- Heim, A., 1932. *Bergsturz und Menschenleben*. Fretz und Wasmuth, Zurich, p.218.
- Hsü, K.J., 1975. Catastrophic debris streams (sturzstroms) generated by rock falls. *Geological Society of America Bulletin*, 86,129–140.
- Hungr, o., 1995. A model for runout analysis of rapid flow slides, debris flows, and avalanches. *Canadian Geotechnical Journal*, 32,610–623.
- Hancox, G.T., Perrin, N.D., and Dellow, G.D., 1997. Earthquake-induced Landsliding in New Zealand and Implications for MM Intensity and Seismic Hazard Assessment, Institute of Geological and Nuclear Sciences, Ltd., GNS Client Report 43601B.
- Hancox, G.T., Perrin, N.D., and Dellow, G.D., 2002. Recent Studies of Historical Earthquake-Induced Landsliding, Ground Damage, and MM Intensity in New Zealand, *Bulletin of the New Zealand Society for Earthquake Engineering*, 35(2), 59–94.
- Hunter,G., Fell, R., 2003. Travel distance angle for “rapid” landslides in constructed and natural soil slopes. *Canadian Geotechnical Journal*, 40, 1123–1141.
- Huang, J.L., Zhao, D.P., 2006. High-resolution mantle tomography of China and surrounding regions. *Journal of Geophysical Research*, 111, B09305.
- Hubbard, J., Shaw, J.H., and Klinger, Y., 2008, Structure of the imbricate thrust system that sourced the 2008 M7.9 Wenchuan earthquake: Eos (*Transactions, American Geophysical Union*), 89, Fall meeting supplement, abs. T24B-01.
- Huang, R.Q., Li, W.L., 2009a. Analysis of the geo-hazards triggered by the 12 May 2008 Wenchuan earthquake, China. *Bulletin of Engineering Geology and the Environment*, 68, 363–371.
- Huang, R.Q., Li, W.L., 2009b. Research on development and distribution rules of geohazard induced by Wenchuan earthquake on 12th May, 2008. *Chinese Journal of Rock Mechanics and Engineering*, 27(12), 2585–2592. (In Chinese with English abstract)
- Hattajji, T., Moriwaki, H., 2009. Morphometric analysis of relic landslides using detailed landslide distribution maps: Implications for forecasting travel distance of future landslides. *Geomorphology*, 103, 447– 454.

- Ikeya, H., 1981. A method of designation for area in danger of debris flow. In: Davies, T.R.H., Pearce, A.J. (Eds.), I.A.H.S. Publication No. 132, Erosion and Sediment Transport in Pacific Rim Steeplands. Christchurch, New Zealand, pp. 576–587.
- Ikeya, H., 1989. Debris flow and its countermeasures in Japan. *Bulletin of the International Association of Engineering Geology*, 40, 15–33.
- Jia, D., Li, Y.Q., Li, A.M., et al., 2010. Structural model of 2008 M_w 7.9 Wenchuan earthquake in the rejuvenated Longmen Shan thrust belt, China. *Tectonophysics*, 491, 174–184.
- Keefer, D.K., 1984. Landslides Caused by Earthquakes, *Geological Society of America Bulletin*, 95, 406–421.
- Keefer, D.K., 2002. Investigating landslides caused by earthquakes—a historical review. *Surveys in Geophysics*, 23, 473–510.
- Kokusho, T. and Ishizawa, T., 2007. Energy approach to earthquake-induced slope failures and its implications. *Journal of Geotechnical and Geoenvironmental Engineering*, 133, 828–840.
- Kokusho, T., Ishizawa, T., Nishida, K., 2009. Travel distance of failed slopes during 2004 Chuetsu earthquake and its evaluation in terms of energy. *Soil Dynamics and Earthquake Engineering*, 29, 1159–1169.
- Lo, D.O.K., 2000. Review of Natural Terrain Landslide Debris-resisting Barrier Design. GEO Report No. 104. Geotechnical Engineering Office, Civil Engineering Department, The Government of Hong Kong Special Administrative Region.
- Lergros, F., 2002. The mobility of long-runout landslides. *Engineering Geology*, 63, 301–331.
- Li, Y., Allen, P.A., Densmore, A.L., Xu, Q., 2003. Evolution of the Longmen Shan foreland basin (western Sichuan, China) during the late triassic indosinian orogeny. *Basin Research*, 15, 117–138.
- Liu, A.W., Xia, S., Xu, C., 2008. Damage and emergency recovery of the transportation systems after Wenchuan earthquake. *Technology for Earthquake Disaster Prevention*, 3(3), 243–250. (In Chinese with English abstract)
- Luo, G., Hu, X.W., Zhang, Y., 2010. Seismic dynamic responses of plane sliding rock slope. *Journal of Southwest Jiaotong University*, 45(4), 521–526. (In Chinese with English abstract)
- Lenti, L., Martino, S., 2012. The interaction of seismic waves with step-like slopes and its influence on landslide movements. *Engineering Geology*, 126, 19–36.

- Molnar, P. and Tapponnier, P., 1975. Cenozoic tectonics of Asia: Effects of a continental collision. *Science*, 189(4201), 419-426.
- Martino, S., Scarascia Mugnozza, G., 2005. The role of the seismic trigger in the Calitri landslide (Italy): historical reconstruction and dynamic analysis. *Soil Dynamics and Earthquake Engineering*, 25, 933–950.
- Meunier, P., Hovius, N., Haines, J., 2007. Regional patterns of earthquake-triggered landslides and their relation to ground motion. *Geophysical research letters*, 34(L20408), 5 pages.
- McArdell, B.W., Cesca, M., Huggel, C., Scheuner, T., Graf, C., Christen, M., 2007. Numerical modeling of debris flow runout in the Swiss Alps. *Geological Society of America, Denver Annual Meeting, Abstract*.
- Newmark, N.M., 1965. Effects of earthquakes on dams and embankments. *Geotechnique*, 15, 139–159.
- Nguyen, K.V., Gatmiri, B., 2007. Evaluation of seismic ground motion induced by topographic irregularities. *Soil Dynamics and Earthquake Engineering*, 27, 183–188.
- O'Brien, J.S., Julien, P.Y., Fullerton, W.T., 1993. Two-dimensional water flood and mudflow simulation. *Journal of Hydraulic Engineering*, 119, 244–261.
- Okura, Y., Kitahara, H., Kawanami, T., Sammori, T., 2000a. Fluidization in dry landslides. *Engineering Geology*, 56, 347–360.
- Okura, Y., Kitahara, H., Sammori, T., Kawanami, A., 2000b. The effects of rockfall volume on runout distance. *Engineering Geology*, 58, 109–124.
- Okura, Y., Kitahara, H., Kawanami, A., Kurokawa, U., 2003. Topography and volume effects on travel distance of surface failure. *Engineering Geology*, 67, 243–254.
- Papadopoulos, G.A., Plessa, A., 2000. Magnitude-distance relations for earthquake-induced landslides in Greece. *Engineering Geology*, 58, 377–386.
- Prochaska, A.B., Santi, P.M., Higgins, J.D., Cannon, S.H., 2008. Debris flow runout predictions based on the average channel slope (ACS). *Engineering Geology*, 98, 29–40.
- Pudasaini, S.P. and Miller, S.A., 2013. The hypermobility of huge landslides and avalanches. *Engineering Geology*, 157, 124–132.
- Qi, S.W., 2006. Two patterns of dynamic responses of single-free-surface slopes and their threshold height. *Chinese Journal of Geophysics*, 49(2), 518–523. (In Chinese with English abstract)

- Qi, S.W., Xu, Q., Lan, H.X., et al., 2010. Spatial distribution analysis of landslides triggered by 2008.5.12 Wenchuan earthquake, China, *Engineering Geology*, 116, 95–108.
- Qi, S.W., Xu, Q., Zhang, B., et al., 2011. Source characteristics of long runout rock avalanches triggered by the 2008 Wenchuan earthquake, China. *Journal of Asian Earth Sciences*, 10, 896–906.
- Rodríguez, C.E., Bommer, J.J., Chandler, R.J., 1999. Earthquake-induced landslides: 1980-1997, *Soil Dynamics and Earthquake Engineering*, 18, 325–346.
- Rickenmann, D., 1999. Empirical relationships for debris flows. *Natural Hazards*, 19, 47–77.
- Shreve, R.L., 1968. The Blackhawk landslide. *Geological Society of America*, Special paper 108, 1-47.
- Scheidegger, A.E., 1973. On the prediction of the reach and velocity of catastrophic landslides. *Rock Mechanics*. 5, 231–236.
- Sanchez-Sesma, F.J., Rosenblueth, E., 1979. Ground motion at canyons of arbitrary shape under incident SH waves. *Earthquake Engineering and Structural Dynamics*, 7, 441–450.
- Sepulveda, S.A., Murphy, W., Jibson, R.W., et al., 2005a. Seismically induced rock slope failures resulting from topographic amplification of strong ground motions: the case of Pacoima Canyon, California. *Engineering Geology*, 80, 336–348.
- Sepulveda, S.A., Murphy, W., Petley, D.N., 2005b. Topographic controls on coseismic rock slides during the 1999 Chi-Chi earthquake, Taiwan. *Quarterly Journal of Engineering Geology & Hydrogeology*, 38 (2), 189–196.
- Shi, C., Zhou, J.W., Ren, Q., et al., 2008. Ray theory solution of the elevation amplification effect on a single-free-face slope. *Journal of Hohai University (Natural Sciences)*, 36(2), 238–241. (In Chinese with English abstract)
- Sato, H.P., Harp, E.L., 2009. Interpretation of earthquake-induced landslides triggered by the 12 May 2008, M7.9 Wenchuan earthquake in the Beichuan area, Sichuan Province, China using satellite imagery and Google Earth. *Landslides*, 6, 153–159.
- Shen, Z., Sun, J., Zhang, P., et al., 2009. Slip maxima at fault junctions and rupturing of barriers during the 2008 Wenchuan earthquake. *Nature Geoscience*, 2, 718-724.
- Terzaghi, K., 1950. Mechanism of landslides. In: Paige, S. (Ed.), *Application of Geology to Engineering Practice (Berkey Volume)*. Geological Society of America, New York, NY, 83–123.

- Takahashi, T., 1981. Estimation of potential debris flows and their hazardous zones: soft countermeasures for a disaster. *Journal of Natural Disaster Science*, 3(1), 57–89.
- Tsukamoto, Y., Ishihara, K. and Kobari, Y., 2006. Evaluation of runout distances of slope failures during 2004 Niigata-Ken Chuetsu earthquake. *Soils and Foundations*, 46(6), 713–725.
- Tang, C., Zhu, J., Chang, M., et al., 2012. An empirical-statistical model for predicting debris flow runout zones in the Wenchuan earthquake area. *Quaternary International*, 250, 63–73.
- VanDine, D.F., 1996. Debris flow control structures for forest engineering. Working Paper 08/1996, Ministry of Forests Research Program. Victoria, British Columbia.
- Wang, F.W., Cheng, Q.G., Highland, L., et al., 2009. Preliminary investigation of some large landslides triggered by the 2008 Wenchuan earthquake, Sichuan Province, China. *Landslides* 6, 47–54.
- Wang, X.Y., Nie, G.Z. and Wang, D.W., 2010a. Research on relationship between landslides and peak ground accelerations induced by Wenchuan earthquake. *Chinese Journal of rock mechanics and engineering*, 29(1), 82–89. (In Chinese with English abstract)
- Wang, X.Y., Nie, G.Z. and Wang, D.W., 2010b. Relationships between ground motion parameters and landslides induced by Wenchuan earthquake. *Earthquake Science*, 23, 233–242.
- Xu, X.W., Wen, X.Z., Ye, J.Q., et al., 2008a. The Ms8.0 Wenchuan earthquake surface ruptures and its seismogenic structures, *Seismology and Geology*, 30(3), 597-629. (In Chinese with English abstract)
- Xu, X.W., Wen, X.Z., Chen, G.H., and Yu, G.H., 2008b, Discovery of the Longriba fault zone in Eastern Bayan Har Block, China and its tectonic implication: *Science in China series D: Earth Science*, 51,(9), 1209–1223.
- Xu, Q., Fan, X.M., Huang, R.Q., et al., 2009a. Landslide dams triggered by the Wenchuan earthquake, Sichuan Province, south west China. *Bulletin of Engineering Geology and the Environment*, 68, 373-386.
- Xu, X.W., Wen, X.Z., Yu, G.H., et al., 2009b. Coseismic reverse- and oblique-slip surface faulting generated by the 2008Mw7.9 Wenchuan earthquake, China. *Geology*, 37, 515-518.

- Xu, C., Dai, F.C., Yao, X., et al., 2009c. GIS-based landslide susceptibility assessment using analytical hierarchy process in Wenchuan earthquake region. *Chinese Journal of Rock Mechanics and Engineering*, 28(Supp.2), 1–8. (In Chinese with English abstract)
- Xu, C., Dai, F.C., Yao, X., et al., 2010. GIS based certainty factor analysis of landslide triggering factors in Wenchuan earthquake. *Chinese Journal of Rock Mechanics and Engineering*, 29(Supp.1), 2972–2981. (In Chinese with English abstract)
- Xu, C., Xu, X.W., Wu, X.Y., et al., 2013a. Detailed catalog of landslides triggered by the 2008 Wenchuan earthquake and statistical analyses of their spatial distribution. *Journal of Engineering Geology*, 21(1), 25–44. (In Chinese with English abstract)
- Xu, C., Xu, X.W., Yao, X., Dai, F.C., 2013b. Three (nearly) complete inventories of landslides triggered by the May 12, 2008 Wenchuan Mw 7.9 earthquake of China and their spatial distribution statistical analysis, *Landslides*, open access.
- Yin, Y., Wang, F., Sun, P., 2009. Landslide hazards triggered by the 2008 Wenchuan earthquake, Sichuan, China. *Landslides*, 6, 139–151.
- Zhuang, W.L., Liu, Z.Y., Jiang, J.S., 2009. Earthquake-induced damage analysis of highway bridges in Wenchuan earthquake and countermeasures, *Chinese Journal of Rock Mechanics and Engineering*, 28(7), 1377–1387. (In Chinese with English abstract)
- Zhao, C. P., Chen, Z. L., Zhou, L. Q., et al., 2010. Rupture process of the Wenchuan M8.0 earthquake of Sichuan, China: the segmentation feature. *Chinese Science Bulletin*, 55(3), 284-292.
- Ministry of Civil Affairs of the People’s Republic of China, Information from website: <http://www.512gov.cn/GB/123057/8074265.html>
- China earthquake administration (CAE), 2008. information from website: http://www.cea.gov.cn/manage/html/8a8587881632fa5c0116674a018300cf/_content/09_02/02/1233562368699.html.
- British Geological Survey: http://www.bgs.ac.uk/landslides/How_does_BGS_classify_landslides.html
- Geoscience Australia: <http://www.ga.gov.au/hazards/landslide/landslide-basics/what.html>
- U.S. Geological Survey: <http://pubs.usgs.gov/fs/2004/3072/pdf/fs2004-3072.pdf>

Chapter 2 Slope Failure Distribution and Seismic Ground Motion

2.1 Introduction

The Ms8.0 Wenchuan earthquake occurred at the middle segment of the Longmenshan thrust fault belt. Seismological study and field survey both indicated that the seismic source rupture initiated from the southern Longmenshan and propagated unilaterally towards north-northeast for more than 300km, mainly generated about 240km surface rupture along Yingxiu–Beichuan fault and about 72km Hanwang surface rupture along Guanxian–Jiangyou (Xu, et al., 2008, 2009a).

This catastrophic earthquake triggered an unprecedented amount of slope failures in Chinese history. It put forward a great challenge to mitigate this kind of geo-hazard caused by earthquake-induced slope failure, meanwhile, providing lots of data to explore the relation between slope failure distribution and seismic parameters. However, there are very few studies combining seismic ground motion with slope failure distribution, as reviewed in section 1.3.1. In this chapter, it would firstly introduced the data source in section 2.2; section 2.3 reported the distribution regularity of slope failures with respect to epicenter and surface fault rupture, respectively; section 2.4 presented seismic ground motion attenuation law; section 2.5 quantitatively analyzed the relationship between slope failure distribution and peak ground acceleration; An empirical model for distribution attenuation of slope failure would be discussed in the section 2.6; section 2.7 made a summary of this chapter.

2.2 Data source of Wenchuan earthquake

The National Strong-Motion Observation Network System (NSMONS) of China was completely established in March 2008, just before the Wenchuan earthquake (Li, et al., 2008).

During the main shock, 420 accelerometers were triggered, as shown in **Figure 2.1**. 1253 components were recorded except 7 missing components. It was unprecedented in Chinese strong-motion observation history. The maximum acceleration component was recorded at Wolong station, that is, 957.7 cm/s^2 EW component. According to earthquake records nearby seismic source fault, the main characteristics were that the dominant frequencies of EW and NS components were both smaller than 6Hz, UD component is larger than 6Hz (Yu, et al., 2008); the durations were all beyond 90–120s (Chen, et al., 2008; Xu, et al., 2009b). Field evidences demonstrated that the vertical component of ground shaking had a significant effect on slope failure occurrence (Xu and Huang, 2008; Yin, et al., 2009; Yuan, et al., 2010); therefore, three components (EW, NS and UD) were sorted into horizontal component and vertical component to obtain seismic ground acceleration attenuation law based on strong ground motion records of 187 seismic stations in the section 2.4. For horizontal component, vectorial composition was implemented at every record interval to obtain acceleration time history of horizontal component and then horizontal peak ground acceleration (PGA) was extracted. Vertical PGA was directly extracted from UD component.

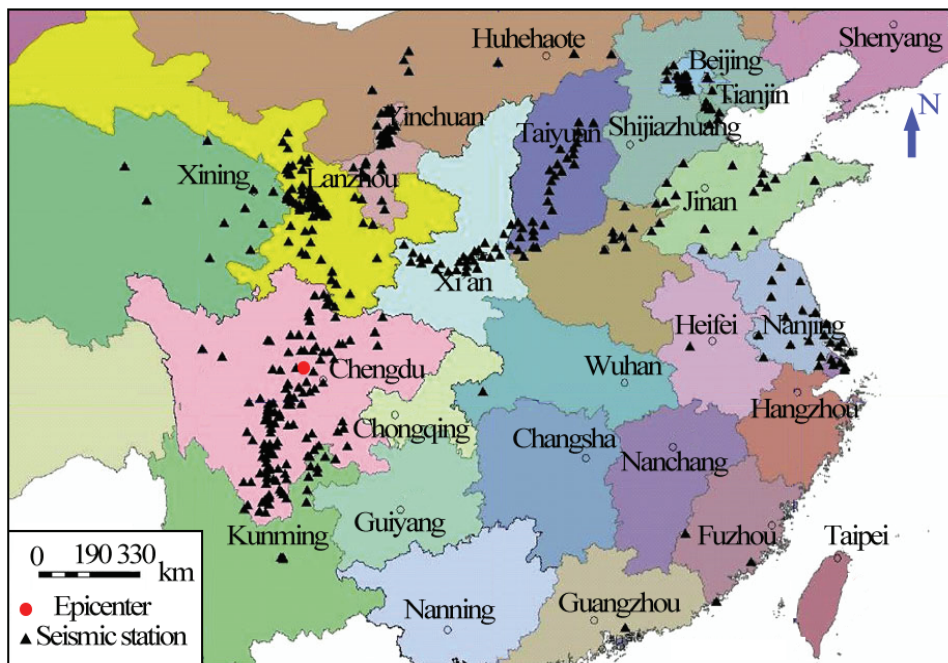


Figure 2.1 The distribution of strong motion stations triggered by the main shock of Wenchuan earthquake (Modified from Yu, H.Y., et al., 2008)

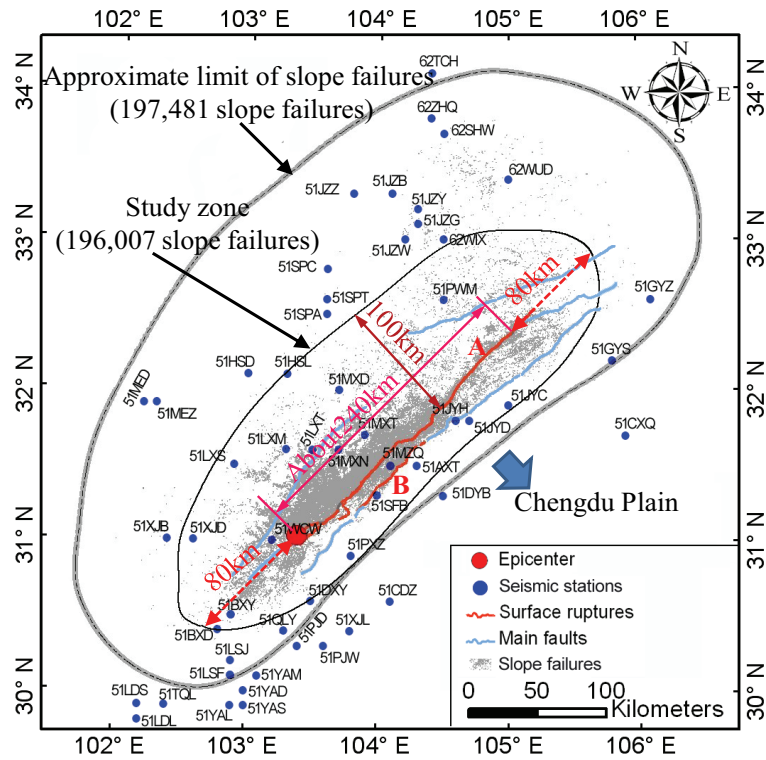


Figure 2.2 Slope failure distribution induced by Wenchuan earthquake and a part of surrounding strong motion stations (After Xu et al., 2013a, b). A: Yingxiu–Beichuan surface fault rupture (about 240km); B: Hangwang surface fault rupture (about 72km).

Wenchuan earthquake occurred in a mountainous zone, slope failure was termed as the representative hazard and attracted high attention from lots of researches. Based on remote sensing interpretation and field investigation, a detailed inventory of Wenchuan earthquake-triggered slope failures was established, which satisfied following requirements, proposed by Harp et al. (2011): (1) covering the entire area affected by earthquake-induced slope failures, (2) including all slope failures down to a size of 1–5 m in length, and (3) depicting slope failures as polygons rather than dots. The results from remote sensing interpretation demonstrated that there were 197,481 slope failures having been triggered in a range of about 110,000km², and sliding area was totally about 1,160km² (Xu et al., 2013a, b). In order to analyze the relationship between the distribution of slope failure and seismic ground motion, a study zone including 99% slope failures out of the total was selected, which covered 44,031km², with 1151km² sliding area. The

boundary of this study zone in southeast direction is close to the intersection between mountain area and Chengdu Plain; in northwest direction, 100km is the maximum distance away from Yingxiu–Beichuan surface fault rupture; the two ends of Yingxiu–Beichuan surface fault were extended 80km. Slope failure distribution and a part of strong motion stations surrounded study zone were both illustrated in **Figure 2.2**.

In the following discussion, two indices about slope failure distribution would be used and defined as follows:

Number concentration of slope failure (*LNC*) was expressed as the number of slope failures per square kilometers in each divided concentric band.

Area distribution percentage of slope failure (*LAP*) was expressed as sliding area divided by the total area of corresponding concentric band, in unit of percentage. This index had a meaning of slope failure occurrence probability.

2.3 Slope failure distribution regularity

In this section, slope failure distribution regularity would be discussed with respect to the epicenter and Yingxiu–Beichuan surface fault rupture, respectively.

2.3.1 Slope failure distribution with respect to epicenter

With respect to epicenter, number concentration of slope failure (*LNC*) and area distribution percentage of slope failure (*LAP*) were determined from a sequence of 5km-width concentric bands, which were outward from epicenter and truncated by the boundary of study zone, as illustrated in **Figure 2.3**. The general tendency of slope failure distribution (*LNC*, *LAP*) related with distance from epicenter was shown in **Figure 2.4**, which suggests that the number concentration of slope failure (*LNC*) and its occurrence probability (*LAP*) significantly decreased with the increment of epicentral distance, generally obeying exponential form. However, there were two abrupt changes, as marked by dot ellipse in **Figure 2.4**. When epicentral distance increased to about 95–105km, the first abrupt change appeared. It might be caused by the transform of rupturing motion. Based on field investigation, Xu et al. (2008, 2009a) pointed out that rupturing motion of Yingxiu-Beichuan surface fault rupture was divided into two segments,

that is, Hongkou-Qingping section, about 105km length, predominated by reserve-faulting with minor right-lateral faulting; Beichuan-Nanba section, about 135km length, mainly dominated by right-lateral faulting with minor reserve-faulting. Between these two segments, it was linked by a 5–6km right bend section; meanwhile, the north end of Hangwang surface rupture (B) was close to the right bend zone of Yingxiu–Beichuan surface fault rupture, as illustrated in **Figure 2.3**. With epicentral distance increase again, slope failure distribution generally decreased. When epicentral distance reached about 210–220km, the second abrupt change appeared, as illustrated in **Figure 2.4**, which is consistent with the north end of Yingxiu–Beichuan surface fault rupture. From above analysis of slope failure distribution regularity and its abrupt changes, it suggested that slope failure distribution was strongly affected by rupturing motion; furthermore, rupturing motion transforming section and the end section of surface fault rupture had relatively strong effect on slope failure occurrence.

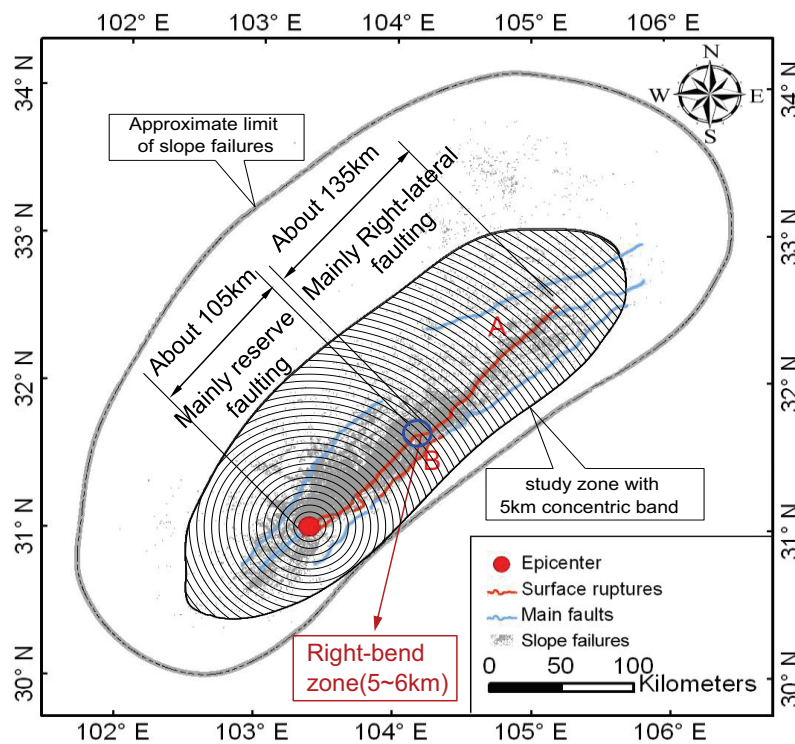


Figure 2.3 Slope failure distribution with respect to epicenter, with 5km width concentric band. A denotes Yingxiu–Beichuan surface fault rupture (about 240km), B denotes Hangwang surface fault rupture (about 72km)

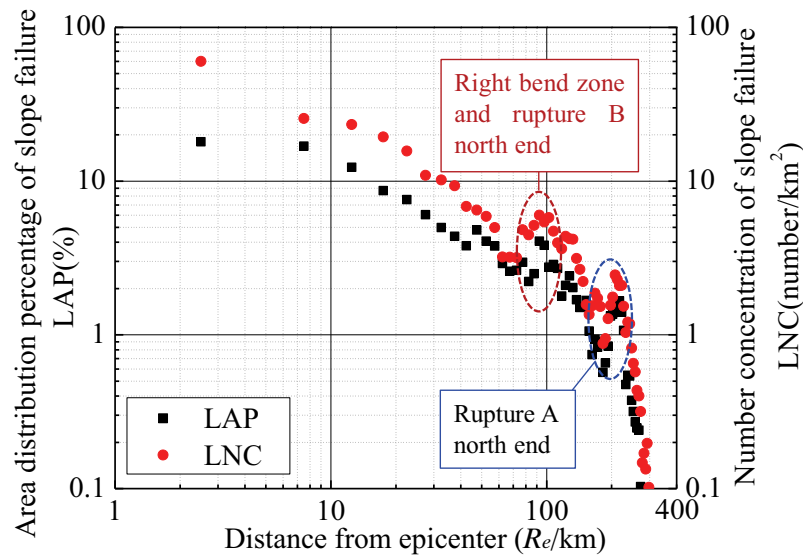


Figure 2.4 Slope failure distribution regularity with respect to epicentral distance.

2.3.2 Slope failure distribution with respect to surface fault rupture

Because slope failure were triggered along the surface fault rupture as a zonal distribution (Huang and Li, 2008), herein, its distribution would be studied with respect to Yingxiu–Beichuan surface fault rupture. Pseudo-rectangle with 5km-width concentric band was moved outward from Yingxiu–Beichuan surface fault rupture and truncated by the boundary of study zone, as shown in **Figure 2.5**, *LNC* and *LAP* were respectively calculated in each band. When just taking absolute value of distance from Yingxiu–Beichuan surface fault as a variable, without consideration of upper or lower side with respect to seismic source fault, the general trend of slope failure distribution was shown in **Figure 2.6**, which suggests that number concentration of slope failure (*LNC*) and area distribution percentage of slope failure (*LAP*) rapidly decreased with the increment of distance from Yingxiu–Beichuan surface fault rupture, generally obeying exponential law. Unlike the distribution with respect to epicenter, there were not any abrupt changes, because the transform of rupturing motion was averaged in each concentric band, therefore, the attenuation curves related with distance from surface fault rupture are smoother than those curves with respect to epicentral distance.

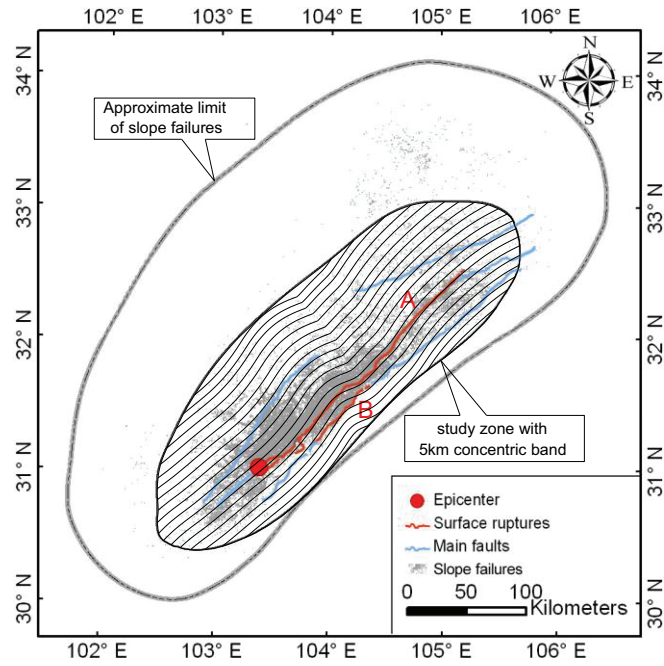


Figure 2.5 Slope failure distribution with respect to Yingxiu-Beichuan surface fault rupture, with 5km-width concentric band. A denotes Yingxiu-Beichuan surface fault rupture (about 240km), B denotes Hangwang surface fault rupture (about 72km)

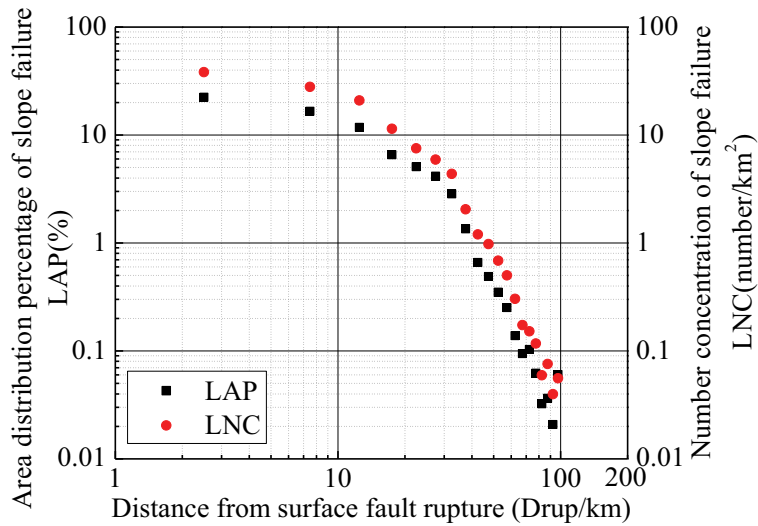


Figure 2.6 Slope failure distribution with respect to distance from Yingxiu-Beichuan surface fault rupture

Since Wenchuan earthquake occurred in a thrust fault, that is, Yingxiu–Beichuan thrust fault, slope failure distribution was further analyzed based on hanging wall side and footwall side. The statistical result was shown in **Figure 2.7**. Within 30km from Yingxiu–Beichuan surface fault rupture, number concentration of slope failure (*LNC*) was 14.0 slope failures per km² on the hanging wall side, which was three times larger than that of footwall side, 4.65 slope failures per km²; while area distribution percentage of slope failure (*LAP*) on the hanging wall side was 8.86%, which was four times larger than that of footwall side, 2.23%. From this statistical result, it clearly revealed that hanging-foot wall effect existed during Wenchuan earthquake, as demonstrated by previous studies on slope failure distribution (Huang and Li, 2009; Chigira et al., 2010; Dai, et al., 2011).

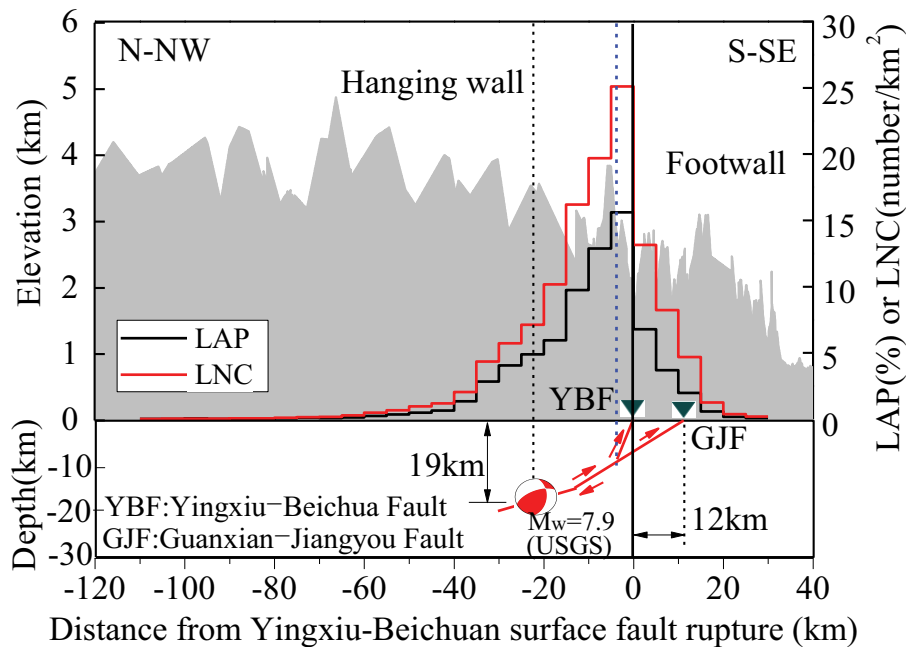


Figure 2.7 Slope failure distribution related with fault rupturing motion. The cross section is taken at epicenter and perpendicular to the strike of Yiungxiu–Beichuan fault. The dip of Yingxiu–Beichuan fault (YBF) is about 60°, the dip of Guanxian–Jiangyou fault (GJF) is about 30° and its trace is east located about 12km from the southern part of Yingxiu–Beichuan surface fault rupture (Hubbard, et al., 2010).

Furthermore, combining slope failure distribution with seismological results from Ji and Hayes (2008), Chen, et al., (2008), Wang and Yao (2008), Hubbard, et al. (2010), the illustration, as **Figure 2.7**, suggests that number concentration of slope failure (*LNC*) and area distribution percentage of slope failure (*LAP*) did not peak at epicenter but around the intersection between Yingxiu–Beichuan fault (YBF) and Guanxian–Jiangyou fault (GJF). It is inconsistent with the 1993 Finisterre earthquake and 1999 Chi-Chi earthquake, which number concentration of slope failure both peaked around the epicenter (Meunier, et al., 2007), although these three earthquakes were all triggered at thrust faults and all existed hanging-foot wall effect. The reason of this difference was inferred that multiple seismic source ruptures of Wenchuan earthquake caused the distribution of slope failures peaked around the intersection between these earthquake source faults.

2.4 Seismic ground motion attenuation

In section 2.3, slope failure distribution regularity was qualitatively analyzed. In order to obtain the quantitative relation between slope failure distribution and seismic ground motion, acceleration attenuation model should be firstly established in this section. Because peak ground acceleration (PGA) is one of the most important and popular indices about seismic ground motion, herein, PGA would be applied to regression analysis of seismic ground motion attenuation.

Since the hanging-foot wall effect had a significant influence on slope failure distribution and its occurrence probability, the acceleration attenuation law was respectively regressed on the hanging wall and footwall side, so as to improve the model proposed by Yu et al. (2008), which did not consider hanging-foot wall effect. Because slope failures were triggered as zonal distribution along the surface fault rupture (Huang and Li, 2008) rather than radial distribution from epicenter, herein, distance from surface fault rupture was used as regression parameter to obtain acceleration attenuation formulae instead of distance from epicenter or hypocenter, which was used in Aydan et al. proposed model (Aydan, et al., 2006, 2009). Furthermore, the main surface fault rupture was 240km Yingxiu–Beichuan surface rupture (Xu, et al., 2008, 2009a) and the USGS finite element model could locate it (Ji and Hayes, 2008), therefore, the nearest

distance from strong motion station to Yingxiu–Beichuan surface fault rupture was used to establish the acceleration attenuation model.

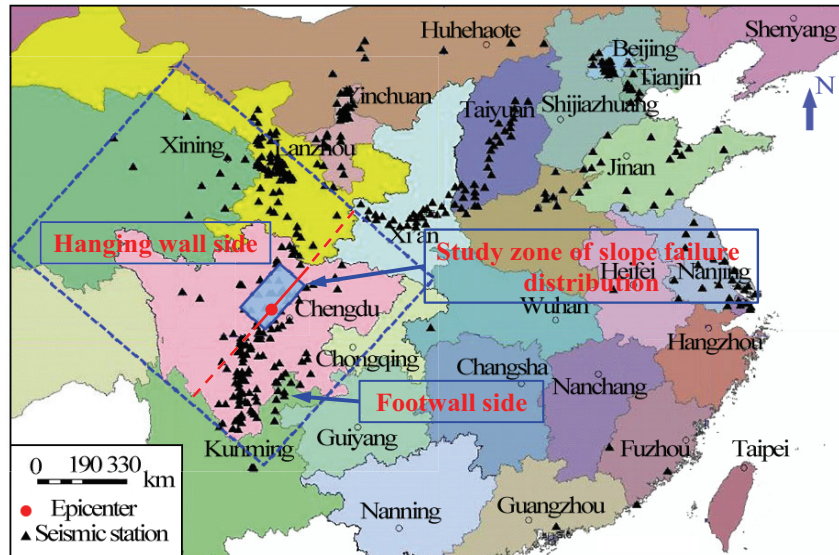


Figure 2.8 Selected strong motion stations in the rectangle for studying seismic ground motion attenuation with respect to Yingxiu–Beichuan surface fault rupture. (Modified from Yu, H.Y., et al., 2008)

420 strong motion stations totally recorded 1253 earthquake time-histories, another 7 components were missing. As a result of hanging-foot wall effect, strong ground motion records of 187 seismic stations were selected to obtain acceleration attenuation law for hanging wall side and footwall side, respectively, and their parameters used were listed in **Appendix Table 1**, these strong motion stations were surrounding the study zone of slope failures and located in a rectangle (1200×1500km), as shown in **Figure 2.8**, which width, 1200km, is about three times as long as the length slope failure study zone. 90 stations located on the footwall side, totally in the Sichuan province; 97 stations located on the hanging wall side, which consisted of 25 stations in the Sichuan province, 61 stations in the Qinghai province and 11 stations in the Gansu province. The peak ground acceleration attenuation model is followed as Eq. (2.1); it would be used to estimate peak ground acceleration in each concentric band with respect to Yingxiu–Beichuan surface fault rupture.

$$\ln PGA = a_1 \ln(D_{rup} + a_2) + a_3 \cdot D_{rup} + a_4 \quad (2.1)$$

where PGA refers to horizontal or vertical peak ground acceleration (cm/s^2); D_{rup} represents nearest distance from site to Yingxiu–Beichuan surface fault rupture (km), which was located by USGS data (Ji and Hayes, 2008); a_1, a_2, a_3, a_4 are the regression coefficients, listed in **Table 2.1**, in which R^2 stands for coefficient of determination. **Figure 2.9** suggests that seismic ground acceleration on the hanging wall side was apparently larger than that on footwall side. According to these regression results, it was inferred that the acceleration difference between hanging wall and footwall was a significant cause to the hanging-foot wall effect, which triggered more slope failures on the hanging wall side.

Table 2.1 Regression parameters of acceleration attenuation on the hanging wall and footwall side with respect to Yingxiu–Beichuan surface fault rupture

Hanging wall or footwall	Component	a_1	a_2	a_3	a_4	R^2
Hanging wall	Horizontal	-0.8203	13.767	-0.0042	9.1689	0.639
	Vertical	-1.6554	33.364	-0.0023	12.670	0.639
Footwall	Horizontal	-0.6907	5.6180	-0.0072	7.9393	0.555
	Vertical	-1.3490	9.4829	-0.0023	9.6389	0.563

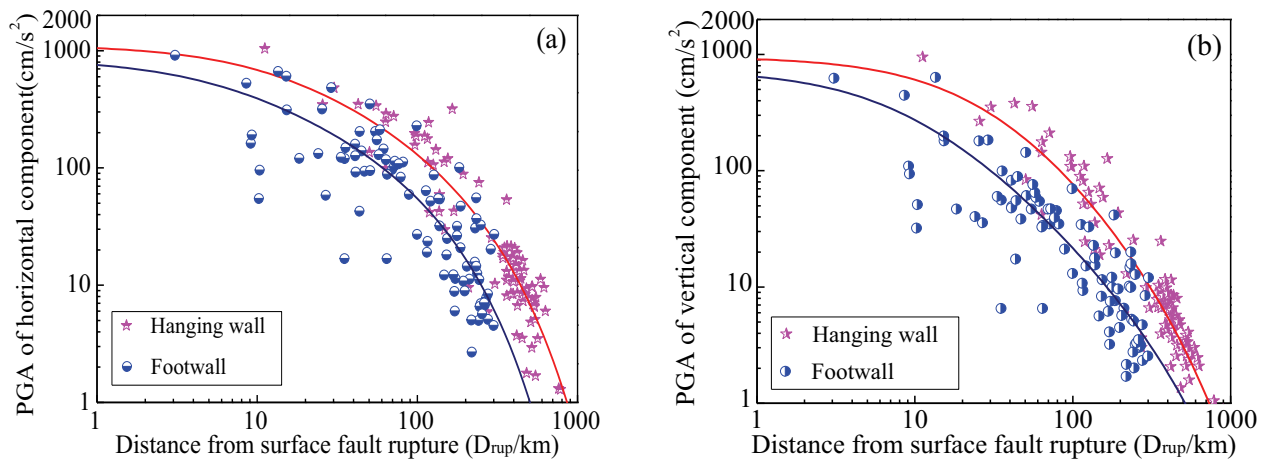


Figure 2.9 Peak ground acceleration attenuation on the hanging wall side and footwall side. (a) Horizontal component. (b) Vertical component.

2.5 Quantitative relation between slope failure distribution and seismic ground motion

In this section, the relation between slope failure distribution and seismic ground motion would be discussed, Eq.(2.1) with regression parameters in **Table 2.1** was applied to estimate the horizontal and vertical PGAs in each 5km width concentric band with respect to Yingxiu-Beichuan surface fault rupture by substituting the distance from each band center into Eq.(2.1). The relations of hanging wall side and footwall side were shown in **Figure 2.10** and **Figure 2.11**, respectively. The best-fit regression reveals that slope failure distribution indices (LNC_{rup} and LAP_{rup}) linearly and highly correlated with horizontal and vertical PGA, obeying following equation:

$$LNC_{rup} \text{ or } LAP_{rup} = b_1 \cdot PGA + b_2 \quad (2.2)$$

where the subscript ‘rup’ of slope failure distribution indices (LNC and LAP) refers to slope failure with respect to Yingxiu-Beichuan surface fault rupture; PGA means peak ground acceleration of horizontal component or vertical component (cm/s^2); b_1 and b_2 are the best-fit regression coefficients. Each regressive equation was shown in the figure, where R^2 means coefficient of determination.

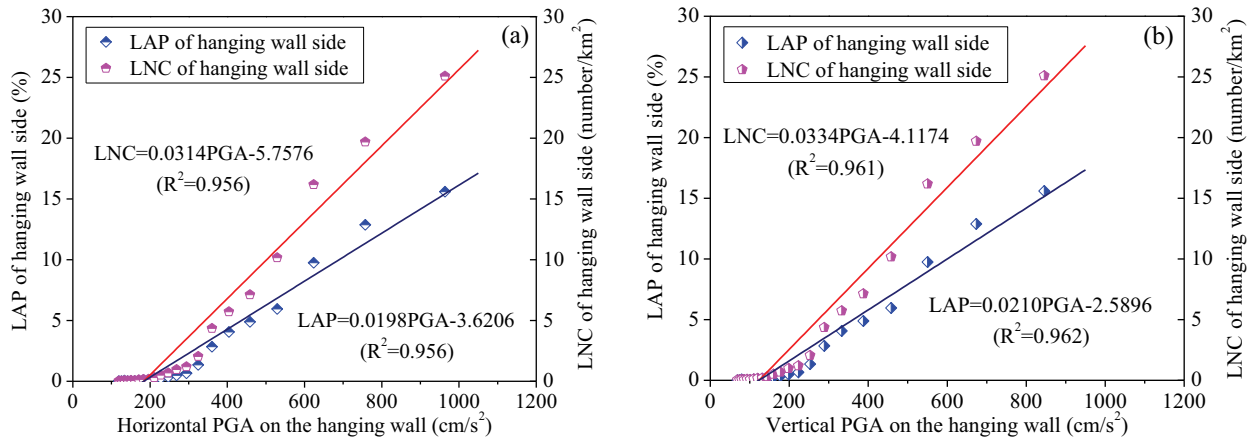


Figure 2.10 The quantitative relation between slope failure distribution and seismic ground motion on the hanging wall side. (a) Horizontal PGA; (b) Vertical PGA.

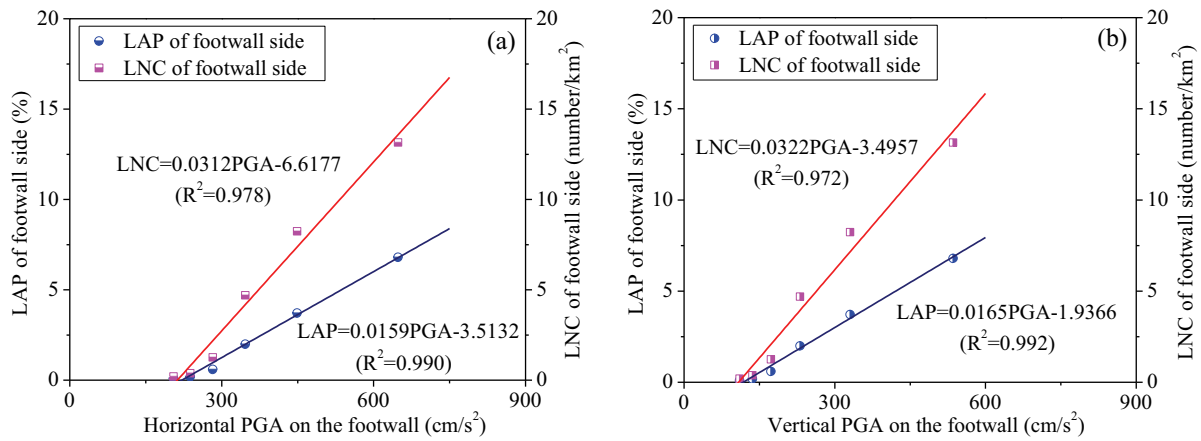


Figure 2.11 The quantitative relation between slope failure distribution and seismic ground motion on the footwall side. (a) Horizontal PGA; (b) Vertical PGA

Table 2.2 Threshold PGA value of slope failure occurrence about three recent earthquakes

Earthquakes	Component	Threshold value of		Reference	
		<i>LNC</i> (cm/s ²)	<i>LAP</i> (cm/s ²)		
2008 Wenchuan earthquake (M _w =7.9)	HW	Horizontal	183.4	182.9	This chapter
		Vertical	123.3		
	FW	Horizontal	212.1		
		Vertical	108.6		
1999 Chi-Chi earthquake (M _w =7.6)	Horizontal	181.5	-	Meunier, et al. (2007)	
	Vertical	101.4	-		
1994 Northridge earthquake (M _w =6.7)	Horizontal	208.6	-		
	Vertical	89.1	-		

*HW: Hanging wall side; FW: Footwall side

The intersection between regression line and horizontal axis is a threshold value of peak ground acceleration to trigger slope failure, theoretically, below which there is no slope failure occurrence. The threshold values were listed in **Table 2.2**, in which, HW means hanging wall, FW represents footwall, *LNC* denotes number concentration of slope failure, *LAP* denotes area distribution percentage of slope failure. For 2008 Wenchuan earthquake, the statistical results suggest that the PGA threshold values of *LNC* and *LAP* are almost the same, indicating that

different statistical methodologies of slope failure distribution have very limited effect on the relation between slope failure distribution and seismic ground motion; meanwhile, the vertical threshold value of PGA on the footwall side is almost the same as that of hanging wall side, while the horizontal threshold value of PGA on the footwall side is about 18% bigger than that of hanging wall side. This might be caused by that the region of susceptible lithology of slope failure occurrence on the hanging wall side were much wider than that on footwall side. Slopes consisting of Sinian sandstone and siltstone (Z), granitic rocks, Cambrian sandstone, siltstone, chert and slate (€), Pre-Sinian schist and andesite (PZ) were more susceptible to be triggered the occurrence of slope failures, as illustrated in **Figure 2.12**; furthermore, these types of susceptible lithology on the hanging wall side were more than twice as wide as those on footwall side, as illustrated in **Figure 2.13**. Hence, the threshold value of slope failure occurrence on the hanging wall side was smaller than that of footwall side.

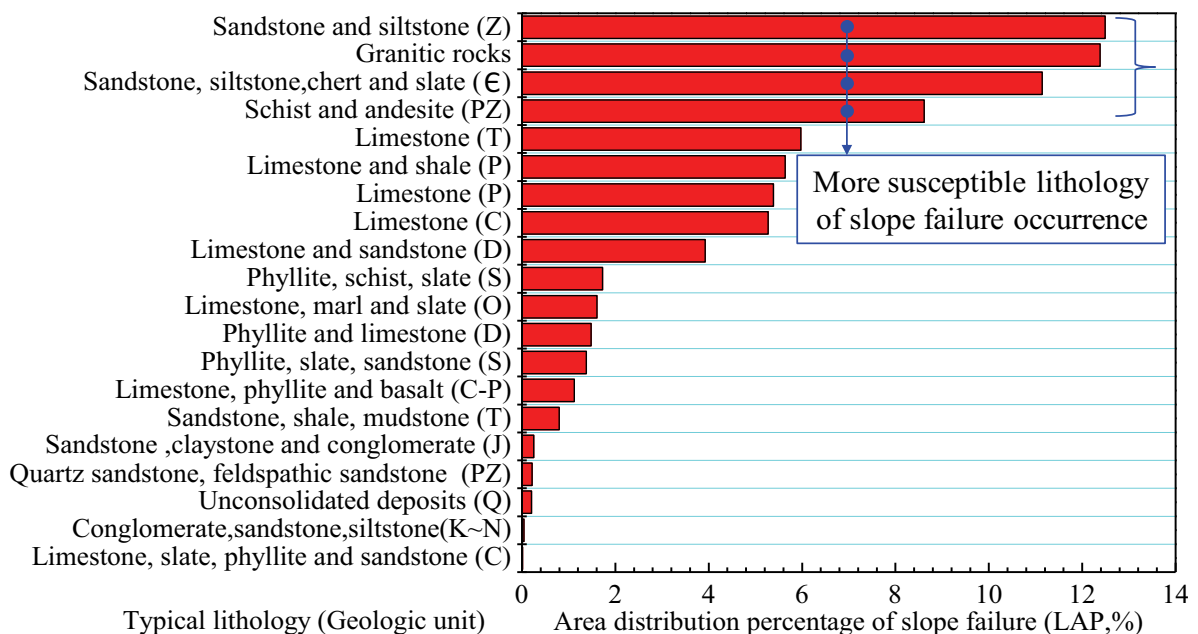


Figure 2.12 Slope failure distribution related with lithology (Data is from Xu et al. 2013); Geologic unit: Z–Sinian; €–Cambrian; PZ–Pre-Sinian; T–Triassic; P–Permian; C–Carboniferous; D–Devonian; S– Silurian; O–Ordovician; C-P– Carboniferous through Permiana; J–Jurassic; Q– Quaternary; K~N– Cretaceous through Neocene.

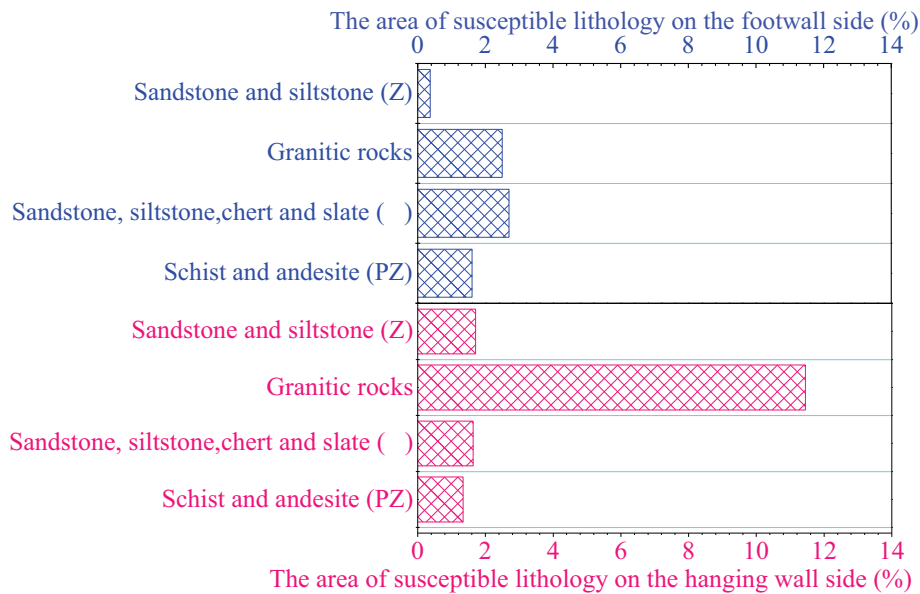


Figure 2.13 Area comparison of susceptible lithology of slope failure occurrence between hanging wall side and footwall side

Compared the statistical threshold values between vertical component and horizontal component, it suggests that threshold value of vertical component was smaller than that of horizontal values, which was attributable to that horizontal component was vectorially composed of EW and NS components at every record interval, while vertical PGA was only from UD component. Hence, it could not roughly get a conclusion that vertical acceleration was more influential than horizontal acceleration on slope stability. Contrarily, horizontal seismic inertial force was usually easier to trigger slope failure than vertical seismic inertial force.

Globally compared with 1999 Chi-Chi earthquake and 1994 Northridge earthquake, it was interestingly found that horizontal PGA threshold values of these three recent earthquakes ranged within 181.5–212.1 cm/s², while vertical PGA ranged within 89.1–123.3 cm/s², as shown in **Table 2.2**. This comparison indicated that horizontal threshold values were very similar to each other among these three earthquakes; even though their moment magnitudes were different and they occurred in different areas with different geological & geomorphological conditions and different climates. The reason was inferred that the properties of the weakest material on the slopes, such as weathered slope materials, were relatively constant in spite of different areas and different settings.

2.6 Discussions

Earthquake-induced slope failure is attributable to numerous influential factors, such as seismic ground motion, geological and topographical conditions, and so on. In generally, all of these influential factors can be classified into two categories, that is, external factor and internal factor. Earthquake plays a triggering role, belonging to external factor. This chapter explored the qualitative and quantitative relations between slope failure distribution (*LAP*, *LNC*) and seismic parameters.

Slope failure distribution with respect to epicenter generally obeyed an exponential decay, as shown in **Figure 2.4**. It may be caused by the evaluation of seismic waves, which amplitude with distance from hypocenter, R , is expressed by followed Eq. (2.3) (Taylor, et al., 1986; Trifunac, 1994):

$$\frac{A_R^{(f,\theta)}}{A_0^{(f,\theta)}} \propto \frac{F_f^\theta}{R^\alpha} \exp\left(-\frac{\pi f}{v} \frac{R}{Q(f)}\right) \quad (2.3)$$

in which $A_0^{(f,\theta)}$ is the wave amplitude close to the source, f is seismic wave frequency, F_f^θ is the radiation pattern or variation of seismic wave form with angular direction θ associated with the focal mechanism, v is the mean wave speed and Q is the quality factor. Seismic wave particle velocity and acceleration have similar correlation. Eq.(2.3) combines two mechanisms of attenuation. The first is the energy loss due to geometrical spreading, which means seismic amplitude $A_R^{(f,\theta)}$ at a radius R decays as $R^{-\alpha}$; the second is the energy loss due to medium properties, such as cracks and joints in rock mass, faults, this effect on attenuation of seismic wave is expressed as exponential decay by quality factor Q , which relies on the wave frequency and seismic wave types and path (Meunier, et al., 2007).

However, slope failures were triggered along the surface fault rupture as a zonal distribution (Huang and Li, 2008), herein, the distribution regularity of slope failures (*LNC*, *LAP*) had been further studied with respect to Yingxiu–Beichuan surface fault rupture, and explored the correlation with seismic peak ground acceleration. Based on the detailed slope failure inventory triggered by the 2008 Wenchuan earthquake, statistical results demonstrated that slope failure distribution (*LNC*, *LAP*) had a highly linear correlation with seismic peak ground acceleration

(PGA), which implied that slope failure distribution attenuation had a similar form as the seismic ground motion attenuation, as Eq.(2.1). Hence, an empirical model for slope failure distribution attenuation was developed based on the data from 2008 Wenchuan earthquake; furthermore, its validity was verified by the data from 1989 Loma Prieta, California earthquake (Keefer, 2000) and 1999 Chi-Chi earthquake (Khazai and Sitar, 2003), as shown in **Figure 12.4** and **Table 2.3**, in which, Y represents number concentration of slope failure (LNC), slope failures/ km^2 , or area distribution percentage of slope failure (LAP), in percentage; D_{rup} denotes distance from surface fault rupture (km); c_1, c_2, c_3, c_4 , are the regression coefficients; R^2 represents coefficient of determination.

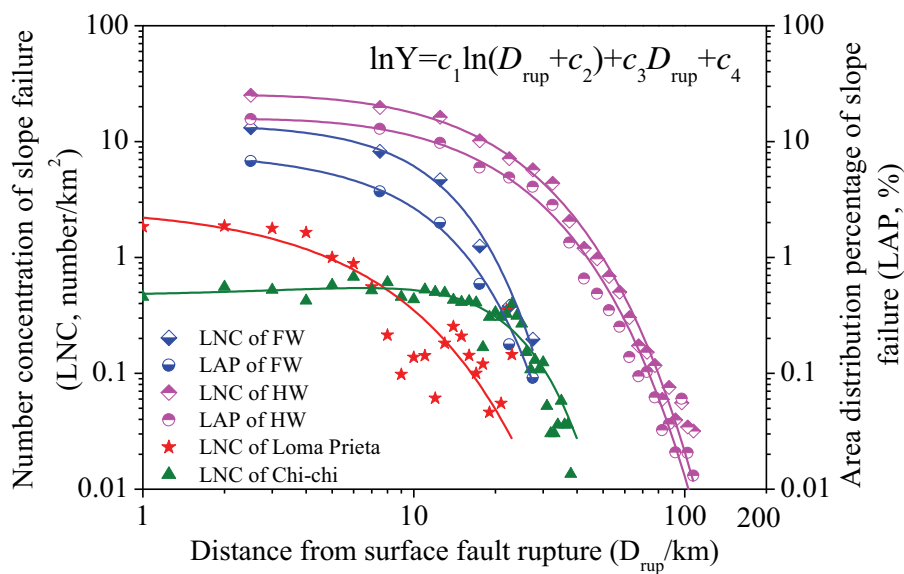


Figure 2.14 Slope failure distribution attenuation during the 2008 Wenchuan earthquake, 1989 Loma Prieta earthquake and 1999 Chi-Chi earthquake. FW means footwall side of Wenchuan earthquake; HW is hanging wall side of Wenchuan earthquake.

The best-fit regressions clearly revealed that slope failure distribution had significantly exponential correlation with distance from surface fault rupture. Although this empirical model for slope failure distribution attenuation was preliminarily explored, the regressive coefficients were quite different among these three earthquakes, which might be caused by these earthquakes with different magnitudes occurred in different regions; the geological and topographical conditions varied and resulted in the different slope failure densities, such as, Keefer (2000)

interpreted 1280 slope failures in about 2000km² triggered by the 1989 Loma Prieta, California earthquake; Khazai and Sitar (2003) analyzed 2507 slope failures in about 14000km² triggered by the 1999 Chi-Chi earthquake. In spite of different earthquake durations, tectonic settings, geological conditions and slope failure densities, slope failure distribution attenuations of these three earthquakes obeyed the same form of formula.

Table 2.3 Regression parameters of empirical model for slope failure distribution attenuation

		$\ln Y = c_1 \ln(D_{rup} + c_2) + c_3 \cdot D_{rup} + c_4$				
Earthquakes and coefficients		c_1	c_2	c_3	c_4	R^2
2008 Wenchuan earthquake	<i>LNC</i> of HW	0.1834	0.2041	-0.0795	3.2355	0.996
	<i>LAP</i> of HW	0.2026	0.3345	-0.0803	2.7379	0.995
	<i>LNC</i> of HW	18.884	34.147	-0.5701	-64.009	0.990
	<i>LAP</i> of HW	17.922	42.559	-0.4927	-65.100	0.995
1984 Loma Prieta, California earthquake	<i>LNC</i> of Loma Prieta	-0.2859	9.9023	-0.1855	1.6595	0.904
1999 Chi-Chi earthquake, Taiwan	<i>LNC</i> of Chi-chi	30.413	58.918	-0.4648	-124.74	0.901

In order to establish a more global and applicable attenuation law for predicting slope failure distribution, more influential factors, such as earthquake magnitude, focal depth, geological and topographical conditions, were recommended to be considered during improvement. Meanwhile, lithology and geological structures of rock mass had effect on failure modes (Aydan, et al., 2009), and different types of slope failure generally had variable potential to endanger different scales of area, thus, area distribution percentage of slope failure (*LAP*) was indirectly affected by lithology and geological structures. Hence, the types of slope failure had better be taken into consideration in the future. During the 2008 Wenchuan earthquake, slope failures were generally classified into four types: (a) shallow and disrupted slope failures; (b) rock falls; (c) deep-seated slope failures; (d) rock avalanches, and large majority were shallow and disrupted slope failures and rock falls (Dai, et al., 2011). Since the amount of slope failures triggered by Wenchuan earthquake was so large (197,481; Xu, et al. 2013a, b) as to be very difficult to catalog failure type of each slope, it caused one limitation of this paper, that is, the failure types of slopes were not differentiated, it need to be further analyzed in the future study.

2.7 Summary

The greatly destructive 2008 Wenchuan earthquake occurred in Longmenshan thrust fault belt and triggered a huge number of slope failures. This chapter had discussed the qualitative and quantitative relations between slope failure distribution and seismic parameters based on a detailed inventory of slope failures and strong ground motion records of 187 seismic stations, several findings were obtained, as follows:

- (1) Slope failure distribution exponentially decreased with the increment of epicentral distance and distance from surface fault rupture; the transforming section of rupturing motion and surface rupture end section had significant effect on the occurrence of slope failure.
- (2) The regressions of acceleration attenuation demonstrated that seismic ground acceleration on the hanging wall side was apparently larger than that on footwall side, which caused hanging-foot wall effect.
- (3) For Wenchuan earthquake, slope failure distribution (*LNC*, *LAP*) did not peak at epicenter but around the intersection between multiple co-seismic faults.
- (4) Slope failure distribution (*LNC*, *LAP*) with respect to surface fault rupture had highly linear correlation with seismic peak ground acceleration, implying that slope failure distribution attenuation had the same decaying form as seismic acceleration.
- (5) The threshold value of slope failure occurrence ranged within 182–212cm/s² horizontal PGA. Due to much wider area of susceptible lithology on the hanging wall, horizontal PGA of slope failure occurrence on the hanging wall side was 18% smaller than that of footwall side.

References

- Aydan, Ö., Ohta, Y., 2006. The characteristics of ground motions in the neighborhood of earthquake faults and their evaluation. Symposium on the Records and Issues of Recent Great Earthquakes in Japan and Overseas, EEC-JSCE, Tokyo, 114–20.
- Aydan, Ö., Ohta, Y., Hamada, M., et al., 2009. The characteristics of the 2008 Wenchuan earthquake disaster with a special emphasis on rock slope failures, quake lakes and damage

- to tunnels. *Journal of the School of Marine Science and Technology, Tokai University*, 7(2), 1–23.
- Chen, Y.T, Xu, L.S., Zhang, Y., et al., 2008. Analysis of the source characteristics of the Wenchuan Earthquake of May 12, 2008. Report by the institute of geophysics, China earthquake administration. (In Chinese)
- Chigira, M., Wu, X.Y., Inokuchi, T., et al., 2010. Landslides induced by the 2008 Wenchuan earthquake, Sichuan, China. *Geomorphology*, 118, 225–238.
- Dai, F.C., Xu, C., Yao, X., et al., 2011. Spatial distribution of landslides triggered by the 2008 Ms8.0 Wenchuan earthquake, China. *Journal of Asian Earth Sciences*, 40, 833–895.
- Huang, R.Q., Li, W.L., 2008. Research on development and distribution rules of geohazards induced by Wenchuan earthquake on 12th May, 2008. *Chinese Journal of Rock Mechanics and Engineering*, 27 (12), 2585–2592. (In Chinese with English abstract).
- Huang, R.Q., Li, W.L., 2009. Analysis of the geo-hazards triggered by the 12 May 2008 Wenchuan earthquake, China. *Bulletin of Engineering Geology and the Environment*, 68, 363–371.
- Hubbard, J., Shaw, J.H. and Klinger, Y., 2010. Structural setting of the 2008 Mw7.9 Wenchuan , China, earthquake. *Bulletin of the Seismological Society of American*, 100:5B, 2713–2735.
- Harp, E.L., Keefer, D.K., Sato, H.P., et al., 2011. Landslide inventories: The essential part of seismic landslide hazard analyses. *Engineering Geology*, 122, 9–21.
- Ji, C., Hayes, G, 2008. Finite fault model-preliminary result of the May 12, 2008 Mw7.9 eastern Sichuan, China earthquake. Information from website: http://earthquake.usgs.gov/earthquakes/eqinthenews/2008/us2008ryan/finite_fault.php
- Keefer, D.K., 2000. Statistical analysis of an earthquake-induced landslide distribution-the 1989 Loma Prieta, California even. *Engineering Geology*, 58, 231–249.
- Khazai, B., Sitar, N., 2003. Evaluation of factors controlling earthquake-induced landslides caused by Chi-chi earthquake and comparison with the Northridge and Loma Prieta events. *Engineering Geology*, 71, 79–95.
- Li, X. J., Zhou, Z. H., Yu, H. Y., et al., 2008. Strong motion observations and recordings from the great Wenchuan earthquake, *Earthquake Engineering and Engineering Vibration*, 7(3), 235–246.

- Meunier, P., Hovius, N., Haines, J., 2007. Regional patterns of earthquake-triggered landslides and their relation to ground motion. *Geophysical research letters*, 34(L20408), 5 pages.
- Taylor, S. R., Bonner, B. P. and Zandt, G., 1986. Attenuation and scattering of broadband P and S waves across North America, *Journal of Geophysical Research*, 91:B77309 –7325.
- Trifunac, M. D., 1994. Q and high frequency strong ground motion spectra. *Soil Dynamics and Earthquake Engineering*, 13, 149 – 61.
- Wang, W.M, Yao, Z. X., 2008. Reissues for the rupture process of the Ms8.0 Wenchuan earthquake. Information from website: http://www.csi.ac.cn/manage/html/4028861611c5c2ba0111c5c558b00001/_content/08_07/11/1215741620117.html. (In Chinese)
- Xu, Q., Huang, R.Q., 2008. Kinetics characteristics of large landslides triggered by may 12th Wenchuan earthquake. *Journal of Engineering Geology*, 16:6,721–729. (In Chinese with English abstract)
- Xu, X.W., Wen, X.Z., Ye, J.Q., et al., 2008. The Ms8.0 Wenchuan earthquake surface ruptures and its seismogenic structures, *Seismology and Geology*, 30(3), 597–629. (In Chinese with English abstract)
- Xu, X. W., Wen, X. Z., Yu, G.H., et al., 2009a. Coseismic reverse- and oblique-slip surface faulting generated by the 2008 Mw 7.9 Wenchuan earthquake, China, *Geology*, 37(6), 515 – 518.
- Xu, Q., Pei, X.J., Huang, R.Q. et al., 2009b. Large-scale landslides induced by the Wenchuan earthquake, Science press, Beijing, (In Chinese)
- Xu, C., Xu, X.W., Wu, X.Y., et al., 2013a. Detailed catalog of landslides triggered by the 2008 Wenchuan earthquake and statistical analyses of their spatial distribution. *Journal of Engineering Geology*, 21(1), 25–44. (In Chinese with English abstract)
- Xu, C., Xu, X.W, Yao, X., Dai, F.C., 2013b. Three (nearly) complete inventories of landslides triggered by the May 12, 2008 Wenchuan Mw 7.9 earthquake of China and their spatial distribution statistical analysis, *Landslides*, open access.
- Yin, Y., Wang, F., Sun, P., 2009. Landslide hazards triggered by the 2008 Wenchuan earthquake, Sichuan, China. *Landslides*, 6, 139 –151.

- Yu, H.Y., Wang, D., Yang, Y.Q., et al., 2008. The preliminary analysis of strong ground motion characteristics from the Ms 8.0 Wenchuan earthquake, China. *Technology for earthquake disaster prevention*, 3(4), 321–336. (In Chinese with English abstract)
- Yuan, R.M., Xu, X.W., Chen, G.H., et al., 2010. Ejection landslide at northern terminus of Beichuan rupture triggered by the 2008 Mw 7.9 Wenchuan earthquake. *Bulletin of the Seismological Society of America*, 100:5B, 2689–2699.

Chapter 3 Influential Factors on Slope Stability and Slope Dynamic Responses

3.1 Introduction

Landslide is one of typical geo-hazards in mountainous areas, and earthquake is a main cause to widely trigger landslides, such as 1999 Chi-Chi earthquake, 2005 Kashmir earthquake and 2008 Wenchuan earthquake. Although the regularity of earthquake-induced landslide distribution is important to understand the relationship between landslide influential factors and causal mechanisms, the cause of landslide occurrence is a comprehensive interplay among seismic parameters (i.e. earthquake magnitude, focal depth, rupturing mechanism and seismic ground motion), geological parameters (i.e. lithology, geological structures), topographical parameters (i.e. slope inclination, altitude, orientation, surface geometrical shape), geomechanical properties (i.e. density, Poisson's ratio and Young's modulus), ground water condition and land use.

Regarding to Wenchuan earthquake, there are many previous studies having discussed landslide distribution and influential factors, as reviewed in section 1.3.2, but most of these studies are limited to qualitatively analyze. In this chapter, qualitative and quantitative analyses were both conducted to explore the general tendency of landslide distribution related with influential factors and comprehensively study the effectiveness of each influential factor on slope stability based on field survey in Wenchuan County in section 3.2. However, influential factors by field investigation are not able to fully reflect the influences of numerous factors, hence, section 3.3 and 3.4 made use of theoretical derivation and finite element simulation to respectively analyze the effects of geomechanical and seismic wave parameters, and geometrical shapes on slope dynamic responses.

3.2 Influential factors on landslide distribution and slope stability

3.2.1 Landslide data collection in Wenchuan County

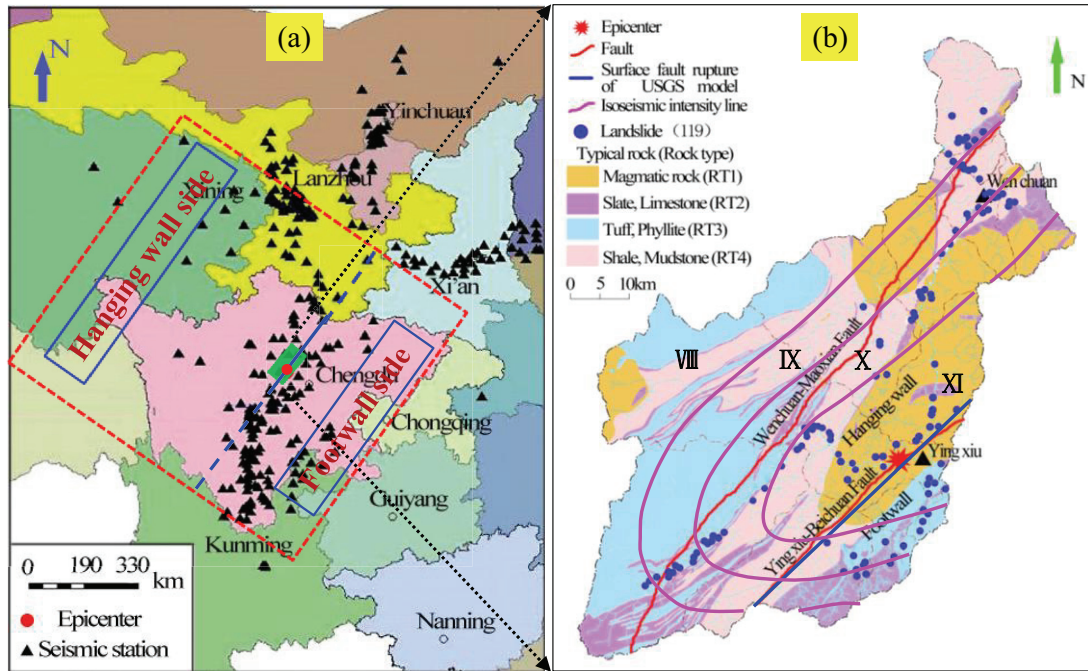


Figure 3.1 (a) The distribution of strong motion stations around Wenchuan County. (b) The distribution of investigated landslides in Wenchuan County.

Wenchuan County, indicated by green rectangle in **Figure 3.1(a)**, locates in the south segment of Longmenshan fault zone. Surface fault rupture of Wenchuan earthquake initiated from this County to north-northeast direction. Seismic intensity of this county was in the range of VIII–XI scale (China Seismic Intensity Scale, CSIS, GB/T17742-1999). Two thrust faults are crossing Wenchuan County, the N25–45°E trending Wenchuan–Maoxian fault and the N35–45°E trending Yingxiu–Beichuan fault. The Wenchuan earthquake occurred on the Yingxiu–Beichuan fault. The attention of investigation carried out in Wenchuan County was paid to two kinds of landslides: firstly, relatively large landslides with a sliding volume bigger than 10^4m^3 ; secondly, landslides that had destroyed the infrastructure. When several landslides were located at close distances and their gradients were almost the same, they were regarded as one landslide zone. 119

landslides were investigated over the area shown in **Figure 3.1(b)**, where the blue solid line represents the strike of the surface fault rupture of the USGS model by Ji and Hayes (2008).

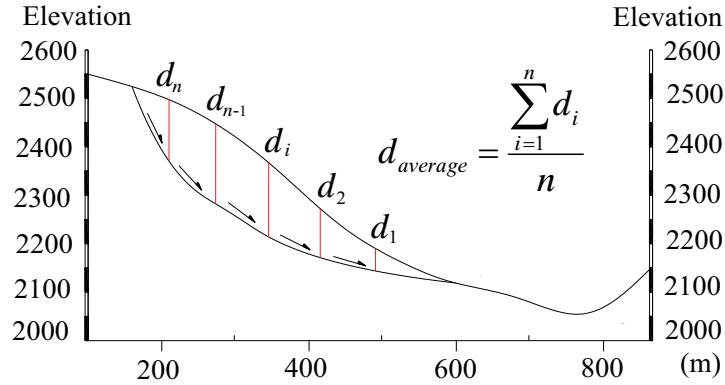


Figure 3.2 Typical longitudinal profile of slope

Table 3.1 Classification standard of rock type (Chang et al., 2006)

Rock type	Weathered degree and typical rock	Uniaxial compression strength (σ_c , MPa)
Hard rock	RT1 Non-weathered~slightly weathered magmatic rock, diorite, basalt, andesite, gneiss and quartzite, etc.	$\sigma_c > 60$
	RT2 1) Non-weathered~slightly weathered marble, slate, limestone, dolomite, metamorphic quartz rock, etc. 2) Moderately weathered magmatic rock, diorite, basalt, andesite, gneiss and quartzite, etc.	$30 < \sigma_c \leq 60$
Soft rock	RT3 1) Non-weathered or slightly weathered tuff, phyllite, marl, sandy mudstone, etc. 2) Moderately ~ strongly weathered hard rock	$15 < \sigma_c \leq 30$
	RT4 1) Non-weathered~slightly weathered shale, mudstone, shaly sand, etc. 2) Strongly weathered hard rock 3) Moderately~strongly weathered tuff, phyllite, marl, sandy mudstone, etc.	$\sigma_c \leq 15$

The sliding source area of each landslide outlined on the map was calculated by using ArcGIS software, and the sliding source volume was estimated by multiplying the sliding source area by the average collapse depth of the sliding body. The average collapse depth was obtained from the typical longitudinal profile of slope, as shown in **Figure 3.2**.

According to rock strength and the degree of weathering, rock materials were assorted into two types, such as hard rock and soft rock, furthermore, they were divided into two subclasses, respectively, as listed in **Table 3.1**.

The horizontal peak ground acceleration attenuation model was obtained in section 2.4 in chapter 2, as following Eq. (3.1), it is same as Eq.(2.1); it was used to estimate horizontal peak ground acceleration of each landslide in Wenchuan County.

$$\ln PHA = a_1 \ln(D_{rup} + a_2) + a_3 \cdot D_{rup} + a_4 \quad (3.1)$$

where *PHA* refers to horizontal peak ground acceleration (cm/s²); *D_{rup}* represents nearest distance from site to Yingxiu–Beichuan surface fault rupture (km), which was located by USGS data (Ji and Hayes, 2008), as shown in **Figure 3.1(b)**; *a₁*, *a₂*, *a₃*, *a₄* are the regression coefficients, partly re-listed in **Table 3.2**, in which *R*² stands for coefficient of determination.

Table 3.2 Regression parameters of horizontal acceleration attenuation model

Hanging wall or footwall	<i>a₁</i>	<i>a₂</i>	<i>a₃</i>	<i>a₄</i>	<i>R</i> ²
Hanging wall	-0.8203	13.767	-0.0042	9.1689	0.639
Footwall	-0.6907	5.6180	-0.0072	7.9393	0.555

All of the parameters of 119 investigated landslides in Wenchuan County were listed in **Appendix Table 2**.

3.2.2 Qualitative analysis of influential factors on landslide distribution

Each influential factor was classified into several groups to calculate landslide area distribution percentage and landslide frequency. Landslide area distribution percentage was expressed as sliding area (LA) divided by the total area of corresponding group (TA), in units of percentage. It represents landslide occurrence probability. The area refers to planar projection area, obtained by ArcGIS based on geological map or topographic map. Landslide frequency means the number of landslides in each classified group out of the total. The following part would qualitatively analyze landslide distribution related with five influential factors.

3.2.2.1 The effect of seismic acceleration

The distance from surface fault rupture was classified into 8 groups with 5 km interval. Landslides area distribution percentage and frequency of each group were shown in **Figure 3.3**, it

suggests that most of landslides occurred in 0–20km from Yingxiu–Beichuan surface fault rupture in Wenchuan County, and landslide occurrence probability in the zone of 0–10km is the highest and decreased with the increase of distance from surface fault rupture. The reason might be explained by the fact that the horizontal peak ground acceleration decreased with the distance increment.

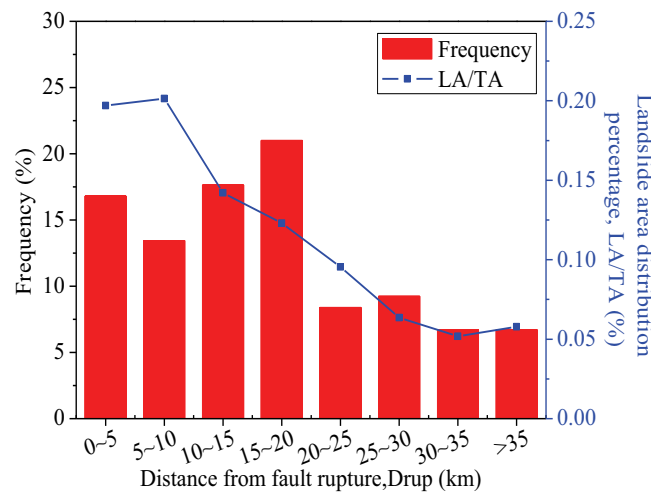


Figure 3.3 Landslide distribution related with the distance from surface fault rupture

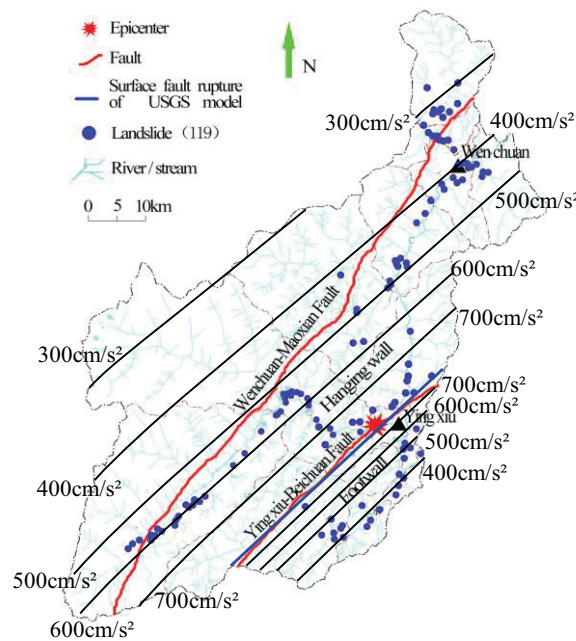


Figure 3.4 The distribution of estimated horizontal PHA in Wenchuan County

In order to have insight into the relationship between landslide distribution and horizontal peak ground acceleration, the acceleration in Wenchuan County was divided into 6 groups, by using

Eq.(3.1) to estimate, as illustrated in **Figure 3.4**. Statistical results about landslide area distribution percentage and frequency were shown in **Figure 3.5**. It suggests landslide occurrence probability increased with the increment of horizontal peak ground acceleration, but landslide frequencies in 300–600cm/s² were much larger than those in bigger than 600cm/s² groups, it might be attributed to that the area within 300–600cm/s² is very large, resulting in including more landslides. It also might be due to investigation methodology, because attention was paid to those landslides having destroyed infrastructure or landslide scale bigger than 10⁴m³.

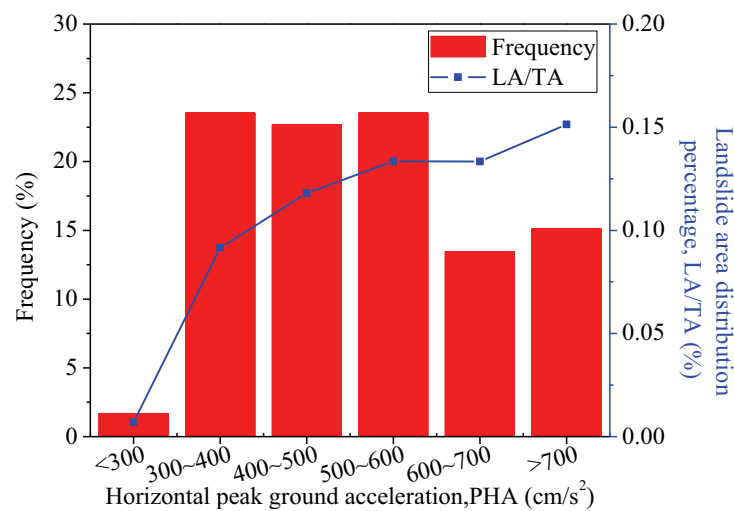


Figure 3.5 Landslide distribution related with horizontal peak ground acceleration

3.2.2.2 The effects of slope angle and height

In order to analyze the effects of slope angle and slope height on landslide distribution, a digital elevation model (DEM) with 40m×40m grid spacing produced from topographic map was used to obtain the total area (TA) of each slope angle or slope height group. During investigation, the slope angle was estimated by taking average gradient of typical longitudinal section and referring to the gradients of the adjacent slope. For the slope height, it was estimated by elevation difference between slope top and toe, where the slope toe was defined as the location of the valley against the sliding direction.

The range of slope angle was classified into 5 groups. Landslide area distribution percentage and frequency of each group were shown in **Figure 3.6**, which suggests most of landslides were

triggered within 20–50° slopes, but landslide area distribution percentage increased with slope angle, it means landslide occurrence probability increased with the increment of slope angle.

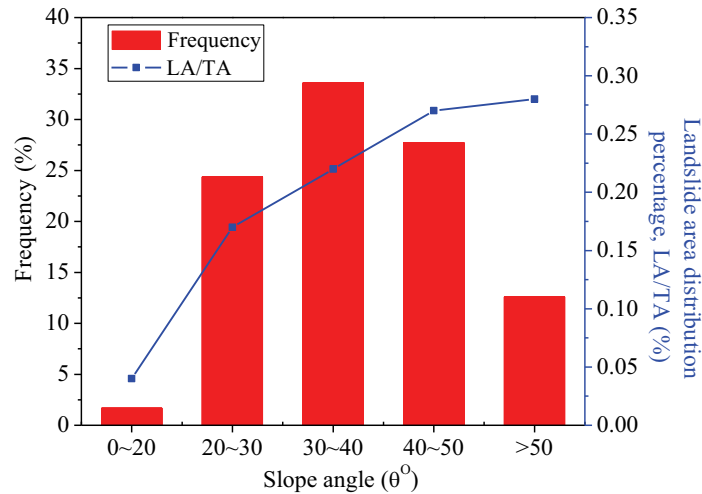


Figure 3.6 Landslide distribution related with slope angle

Slope height was divided into 7 groups. Elevation contour lines in the topographic map were applied to get the total area (TA) of each slope height group. Local maximum elevation was regarded as benchmark to calculate elevation difference between slope crest and surrounding valleys in a segmental zone, and the segmental total area of each height group can be obtained from the topographic map. Using this method, one by one the segmental zones were analyzed to calculate the aggregate total area (TA) of each group.

Figure 3.7 shows that 62% landslides occurred in the slope height range of 50–150m, and landslide area distribution percentage generally increased with the increase of slope height, which reveals landslide occurrence probability increased with slope height during the earthquake. The first reason may be due to topographic amplification effect, that is, seismic acceleration was significantly amplified from slope base towards slope crest. Davis and West (1973) firstly observed this phenomenon, and Lin and Wang (2006), Xu et al. (2008a, 2008b) have already made use of shaking table model test and finite element model to explore and demonstrated acceleration amplification effect was attributed to topography and elevation increment. The second reason may be caused by that higher slopes can accommodate larger landslides because of larger space availability.

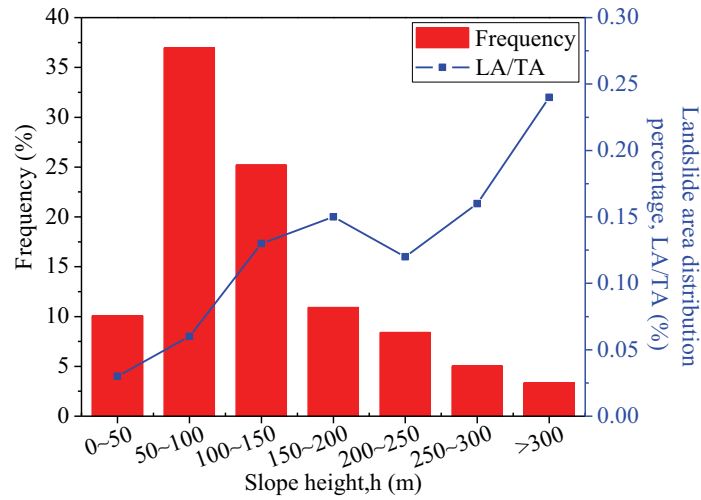


Figure 3.7 Landslide distribution related with slope height

3.2.2.3 The effects of rock type and geological structure

Figure 3.8 shows landslide area distribution percentage and frequency related with rock type, which was divided into four groups as shown in **Table 3.1**. Statistical results reveal that landslide area distribution percentage and frequency increased from hard rock to soft rock and landslide occurrence probability was much higher for soft rocks than for the others.

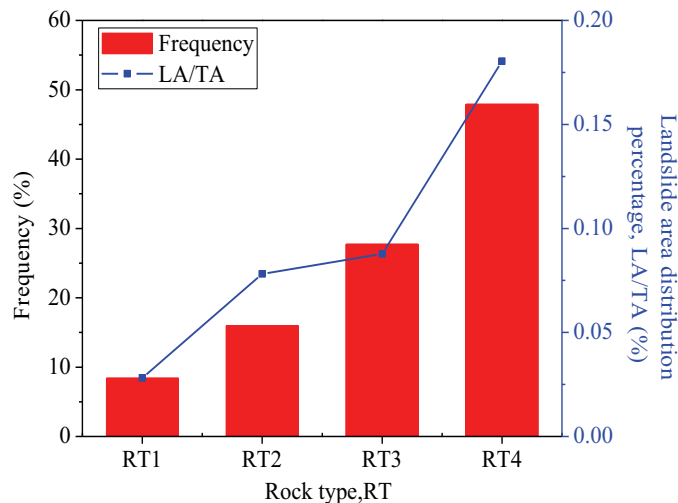

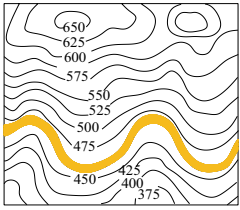
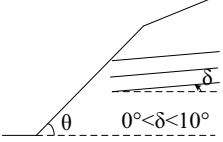
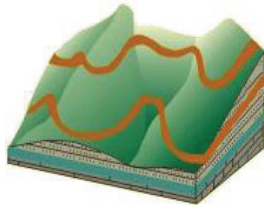
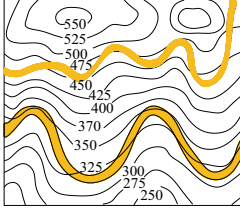
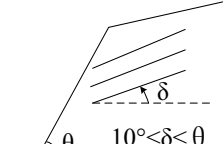
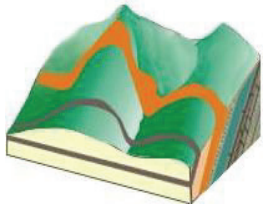
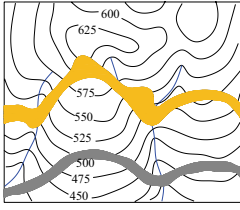
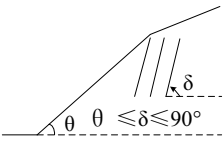
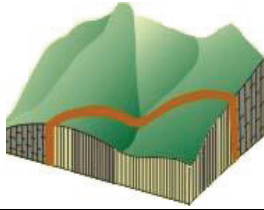
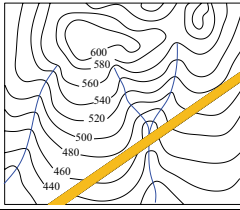
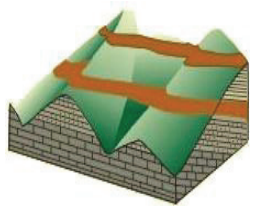
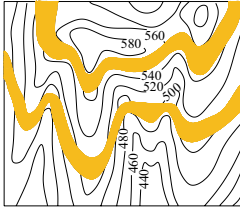
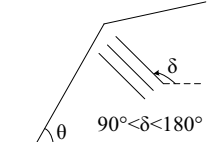
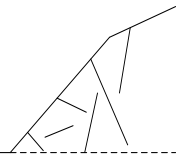
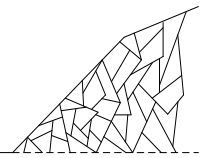


Figure 3.8 Landslide distribution related with rock type

Table 3.3 Sketches of geological structure

Category	3D sketch	Geological map	Cross section	Memo
			 (a) GS1	Stratigraphic boundary lines are parallel or nearly parallel to elevation contour lines.
			 (b) GS2	Curvature magnitude of stratigraphic boundary lines is bigger than that of elevation contour lines, with the same curving direction.
Layer structure			 (c) GS3	The curving direction of stratigraphic boundary lines is opposite to that of elevation contour lines.
				Stratigraphic boundary lines are straight lines on the geological map.
			 (d) GS4	Curvature magnitude of stratigraphic boundary lines is smaller than that of elevation contour lines, with the same curving direction.
Others			 (e) Block structure	Total area (TA) is equal to County area subtracts area of layer structure, in the aid of field survey to outline.
			 (f) Fractured structure	

During investigation, geological structures were found to affect landslide scale and the type of failure modes. According to the assembled characteristics of stratum joints in the vertical and axial direction, slope geological structures were classified into two categories, ‘layer structure’ and ‘others’, as illustrated in **Table 3.3**. ‘layer structure’ was further divided into four subclasses according to the relation between slope angle (θ) and inclination of rock layer (δ).

Figure 3.9 shows a plot of the relation between slope angle and inclination of rock layer for failure modes. It suggests there was almost no slope failure when slope angle is smaller than 20° , landslides mostly occurred in the range of $20\text{--}50^\circ$ slope angle and $20\text{--}60^\circ$ or $90\text{--}140^\circ$ inclination of rock layer. When $\delta < \theta < 90^\circ$, slope failure mostly occurred as sliding failure, when $\delta > 90^\circ$ and $\theta > \delta - 90^\circ$, failure mode mostly appears as topping failure. Given friction angle of stratum joint $\varphi_j = 20^\circ$, 10 failed slopes satisfy the empirical equation of topping failure mode proposed by Goodman and Bray (1976), that is, $\theta > \delta + \varphi_j - 90^\circ$.

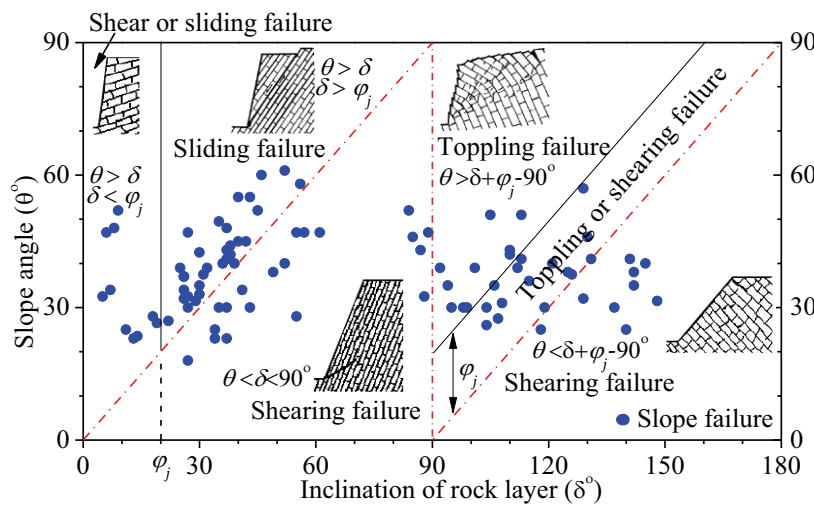


Figure 3.9 The relation between slope angle and inclination of rock layer for failure modes (Based on Aydan, 2009a, b)

Figure 3.10 shows the results of landslide area distribution percentage and frequency related with geological structure, it reveals that slopes with GS2 ($10^\circ < \delta < \theta$) geological structure presented the highest probability of landslide occurrence during the earthquake, and the second highest susceptibility of geological structure is GS4, where the rock layer has adverse inclination direction compared to the topographic gradient. For geological structures of GS1 ($0^\circ < \delta < 10^\circ$) and

GS3 ($\theta < \delta < 90^\circ$), landslide area distribution percentages are both smaller than that of ‘others’; this suggests that slopes with GS1 or GS3 geological structure were more stable during the earthquake.

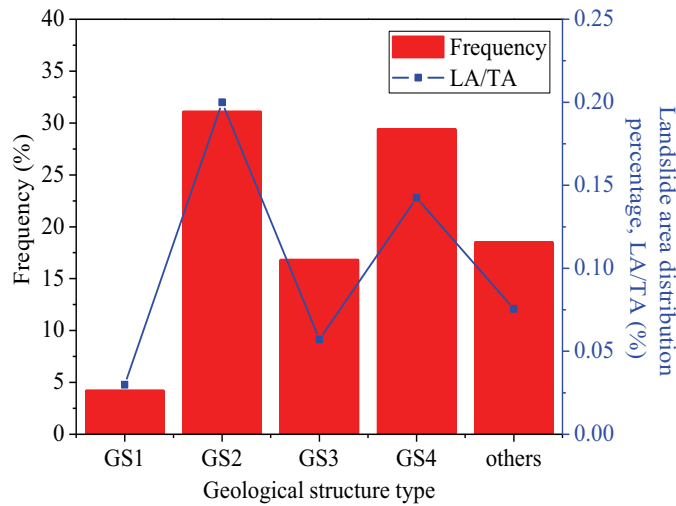


Figure 3.10 Landslide distribution related with geological structure

3.2.3 Multivariable analysis of influential factors on slope stability

Sliding area and volume are the two most important characteristics, marking the potential danger of a mass movement. In this section, there are several relationships between influential factors and landslide area and volume. multivariable regression method would be used to quantitatively discuss these relationships. The parameters of 97 landslides were used for the regression, the other 22 landslides were excluded from the following regression analysis since the geological structure is ‘others’, lacking of the angle of inclination of rock layer (δ).

Based on the assumption of square root of sliding area and cubic root of sliding volume are both linearly correlated with influential factors, multiple linear regression was conducted and a backward elimination approach was applied to obtain the optimization model on the basis of F-test and t-test. The regression procedures and results are shown in **Table 3.4** and **Table 3.5**, in which, A refers to landslide source area (m^2), V refers to landslide source volume (m^3). PHA refers to horizontal peak ground acceleration (m/s^2), estimated from Eq. (3.1). h represents slope height (m), θ represents slope angle ($^\circ$). δ denotes the inclination angle of rock layer ($^\circ$). RT refers to rock type, it was qualitatively considered, 4, 3, 2, and 1 were respectively assigned to RT1, RT2, RT3 and RT4. Multiple R means multiple correlation coefficient, which represents the

correlated level between dependent and independent variables. Adjusted R^2 represents adjusted coefficient of multiple determination, namely, adjusted squared multiple correlation, which reveals the goodness of fit. F-stat denotes regressive F-value, $F_{0.05}$ denotes F-test threshold value with 95% significance level; if F-stat is bigger than $F_{0.05}$, it suggests overall regression satisfies significance level. t-stat denotes regressive t-value of each regression coefficient, $t_{0.05}$ denotes t-test threshold value with 95% significance level; if t-stat is bigger than $t_{0.05}$, it suggests the corresponding regression coefficients (e_i, g_i) satisfy statistical significance level. However, not all regression coefficients are significant during regression procedures; therefore, the variable with smallest absolute t-stat value (bold digit in the **Table 3.4** and **Table 3.5**) was eliminated and then re-regressed, step-by-step until overall regression (F-test) and all regressive coefficients (t-test) both satisfy the significance level. These procedures are named as backward elimination regression. Since the units of independent variables affect regression coefficients (e_i, g_i), standardized regression coefficients (e'_i, g'_i) were applied to exclude the effectiveness of the unit dimension so as to have insight into the influence of each independent variable on the dependent variable.

Out of the four models compared in **Table 3.4** and **Table 3.5**, respectively, F-tests suggest that two hypothetical models have statistical meaning and satisfy linear assumption. Furthermore, the models with 2 variables satisfy not only overall regression significance but also the significance of regression coefficients. Therefore, the models with 2 variables are more convenient and efficient to be applied for prediction.

Table 3.4 Multivariable analysis of sliding area related with influential factors

$A^{1/2} = e_1h + e_2PHA + e_3\sin\delta + e_4\tan\theta + e_5RT$										
Variable and parameter	e_1	e_2	e_3	e_4	e_5	Multiple R	Adjusted R^2	F-stat ($F_{0.05}$)	t-test ($t_{0.05}$)	
5 variables	e_i	0.67	12.97	49.60	-21.95	-4.05	0.891	0.774	71.010 (2.313)	1.986
	t-stat	6.50	2.88	1.30	-0.78	-0.44				
	e'_i	0.59	0.22	0.12	-0.07	-0.04				
4 variables	e_i	0.67	12.36	45.62	-22.95		0.891	89.493 (2.470)	1.986	
	t-stat	6.52	2.90	1.24	-0.83	-				
	e'_i	0.59	0.21	0.11	-0.07					
3 variables	e_i	0.66	10.73	33.39			0.890	119.502 (2.701)	1.986	
	t-stat	6.47	2.84	0.99	-	-				
	e'_i	0.58	0.19	0.08						
2 variables	e_i	0.71	13.55				0.889	178.794 (3.092)	1.985	
	t-stat	7.94	5.45	-	-	-				
	e'_i	0.62	0.23							

Table 3.5 Multivariable analysis of sliding volume related with influential factors

$$V^{1/3} = g_1h + g_2PHA + g_3\sin\delta + g_4\tan\theta + g_5RT$$

Variable and parameter	g_1	g_2	g_3	g_4	g_5	Multiple R	Adjusted R ²	F-stat (F _{0.05})	t-test (t _{0.05})	
5 variables	g_i	0.20	3.39	23.32	-6.11	0.49	0.895	74.481 (2.313)	1.986	
	t-stat	5.97	2.28	1.85	-0.66	0.16				
	g'_i	0.55	0.18	0.18	-0.06	0.01				
4 variables	g_i	0.20	3.46	23.84	-5.99	0.895	0.785	94.080 (2.470)	1.986	
	t-stat	6.02	2.46	1.96	-0.65					-
	g'_i	0.55	0.19	0.18	-0.06					-
3 variables	g_i	0.20	3.04	20.61	-	-	0.895	126.068 (2.701)	1.986	
	t-stat	6.01	2.44	1.86	-	-				
	g'_i	0.55	0.16	0.16	-	-				
2 variables	g_i	0.23	4.78	-	-	-	0.891	182.655 (3.092)	1.985	
	t-stat	7.79	5.77	-	-	-				
	g'_i	0.63	0.26	-	-	-				

Based on above stepwise regression and analysis, the optimization procedures and absolute values of standardized regression coefficients in the 5 variables models both suggest slope height, horizontal peak ground acceleration and geological structure are more influential to sliding source area and volume than slope angle and rock type. Because sliding source area and sliding volume are the two most important slope failure impact factors, it implies that slope height, horizontal peak ground acceleration and geological structure are the most important factors to affect slope stability during the earthquake among these five influential factors.

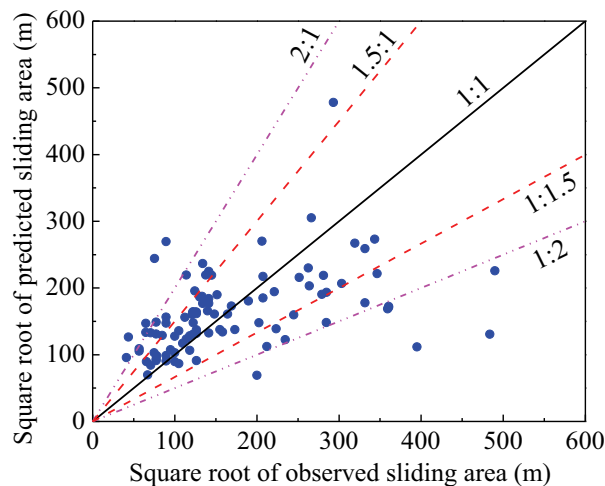


Figure 3.11 Comparing square root of observed sliding source area with the predicted values

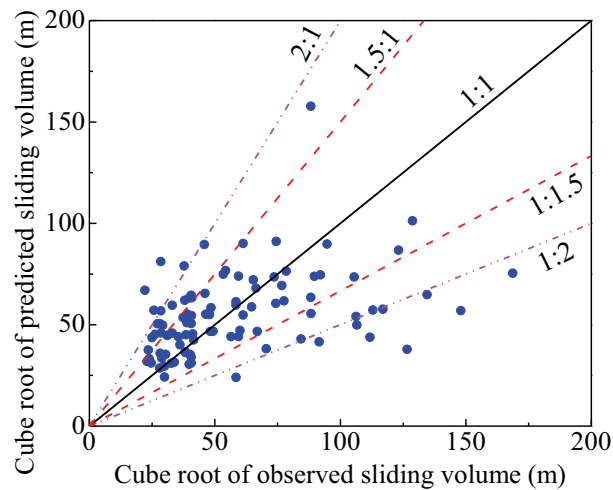


Figure 3.12 Comparing cube root of observed sliding source volume with the predicted values

By using empirical optimization models, the predicted square root of sliding source area and cubic root of sliding source volume are compared with observed results, as shown in **Figure 3.11** and **Figure 3.12**, respectively. In these two plots, some points scatter a little large, such as those points below the red dot line with 1:2 slope, it means observed results are much bigger than predicted results, it might be caused by that several adjacent landslides with almost the same slope angle were regarded as one sample during investigation; while some points above 2:1 gradient red dot line may be due to regression error.

There are numerous influential factors on slope stability and landslide scale, some of which have been discussed in this section; however, some other factors are not mentioned here, such as ground water, vegetation, human activity, slope aspect and so on. It is hard to gather information on all influential factors; this section tried to make use of limited data to analyze the quantitative relationship between sliding source area and volume with influential factors. Even if the predicted results based on multiple linear regression models are not perfect, the stepwise regression demonstrated that these two hypothetical models satisfied the overall significance level and the significance of regression coefficients. Moreover, 0.78 adjusted R^2 represents a reasonable acceptance level, and 0.9 multiple correlation coefficient suggests square root of sliding source area and cubic root of sliding source volume strongly correlate with the influential factors. Therefore, the aforementioned quantitative analysis procedures and results are acceptable. Nevertheless, further research needs to be carried out to refine the predicted models.

3.3 Theoretical analysis of influential factors on slope dynamic responses

Based on the number of the inclined free air surface, slope is divided into single surface slope and double surface slope. In this section, seismic wave was regarded as elastic wave to research dynamic responses of slope with single free air surface. Several influential factors were taken into consideration, namely, geomechanical properties (i.e. Poisson's ratio, Young's modulus and density), seismic parameters (wave frequency and input angle) and slope angle, which supplemented the research conducted in section 3.2 to explore more influential factors on slope stability and its dynamic responses.

3.3.1 Wave mode conversion on the free air surface

Earthquake shaking energy is transmitted by P-wave and S-wave. In generally, horizontal earthquake loading is applied when analyzing slope dynamic responses, hence, the following will regard S-wave as source wave which acts on the slope. When seismic S-wave inputs into the slope and encounters with the inclined surface (free air surface), it will be reflected, meanwhile, generating P-wave, as shown in **Figure 3.13**, in which, XOY is the global coordinate system, $lo'm$ is the local coordinate system. ϕ denotes S-wave input angle and its reflected S-wave angle related to the perpendicular line to slope inclined surface, ψ refers to the angle of transmitting direction of reflected P-wave related to the perpendicular line to slope inclined surface. θ represents slope angle.

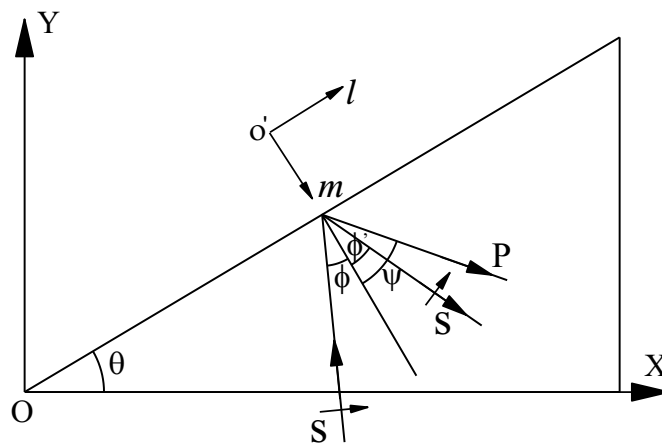


Figure 3.13 Sketch of S-wave mode conversion on the inclined free air surface

The displacement formulae of seismic wave can be expressed as follows, which all are expressed in the local coordinate system, $lo'm$.

$$\text{Input S-wave: } S_d = Z e^{i(k_l l + k_m m - \omega t)}, \text{ in which } k_l = \frac{\omega}{v_s} \sin \phi, k_m = \frac{\omega}{v_s} \cos \phi \quad (3.2)$$

$$\text{Reflected S-wave: } S_d' = Z' e^{i(k_l' l + k_m' m - \omega' t)}, \text{ in which } k_l' = \frac{\omega'}{v_s} \sin \phi', k_m' = \frac{\omega'}{v_s} \cos \phi' \quad (3.3)$$

$$\text{Reflected P-wave: } S_d'' = U e^{i(k_l'' l + k_m'' m - \omega'' t)}, \text{ in which } k_l'' = \frac{\omega''}{v_s} \sin \psi, k_m'' = \frac{\omega''}{v_s} \cos \psi \quad (3.4)$$

In above all formulae, S_d , S_d' , S_d'' mean seismic wave displacement; k , k' , k'' represent wave number; ω , ω' , ω'' , refer to wave circular frequency; v_s , v_p denote velocity of S-wave and P-wave, respectively. According to elastic wave theory, all of the aforementioned three formulae should obey wave equation (Hu, J.X. et al., 2006), and the boundary conditions on the inclined free air surface are shown as Eq. (3.5):

$$\omega = \omega' = \omega'' \text{ and } k_l = k_l' = k_l'' \quad (3.5)$$

Therefore, deriving from wave equation combined with boundary conditions, Eq. (3.6) can be obtained:

$$\phi = \phi' \text{ and } \frac{\sin \phi}{v_s} = \frac{\sin \psi}{v_p} \quad (3.6)$$

Meanwhile, the displacement reflection coefficients of P-wave and S-wave are shown as following Eq. (3.7) and Eq. (3.8), respectively,

$$\eta_{pd} = \frac{U}{Z} = \frac{-D^2 \sin 4\phi}{D^2 \cos^2 2\phi + \sin 2\psi \sin 2\phi} \quad (3.7)$$

$$\eta_{sd} = \frac{Z'}{Z} = \frac{\sin 2\phi \sin 2\psi - D^2 \cos^2 2\phi}{D^2 \cos^2 2\phi + \sin 2\psi \sin 2\phi} \quad (3.8)$$

In which, $D = \frac{v_p}{v_s} = \sqrt{\frac{2-2\nu}{1-2\nu}}$. η_{pd} , η_{sd} refer to amplification ratio of reflected P-wave and reflected S-wave to input S-wave, respectively, they are named as displacement reflection coefficients. Subscript p and s refer to 'P-wave' and 'S-wave', respectively; subscript d refers to 'displacement'. Eq. (3.7) and Eq. (3.8) reveal P-wave reflection coefficient and S-wave reflection coefficient are both only related to Poisson's ratio and seismic wave input angle, as illustrated in **Figure 3.14**.

The Eq. (3.6) is the Snell law, it can be used to deduce the input critical angle, expressed as $\arcsin(v_s/v_p)$. It means when S-wave inputs into slope, it will be reflected on the slope inclined free air surface, only if input angle $\phi < \arcsin(v_s/v_p)$, P-wave will be generated. Therefore, Eq. (3.7) and Eq. (3.8) are valid when input angle smaller than this input threshold angle.

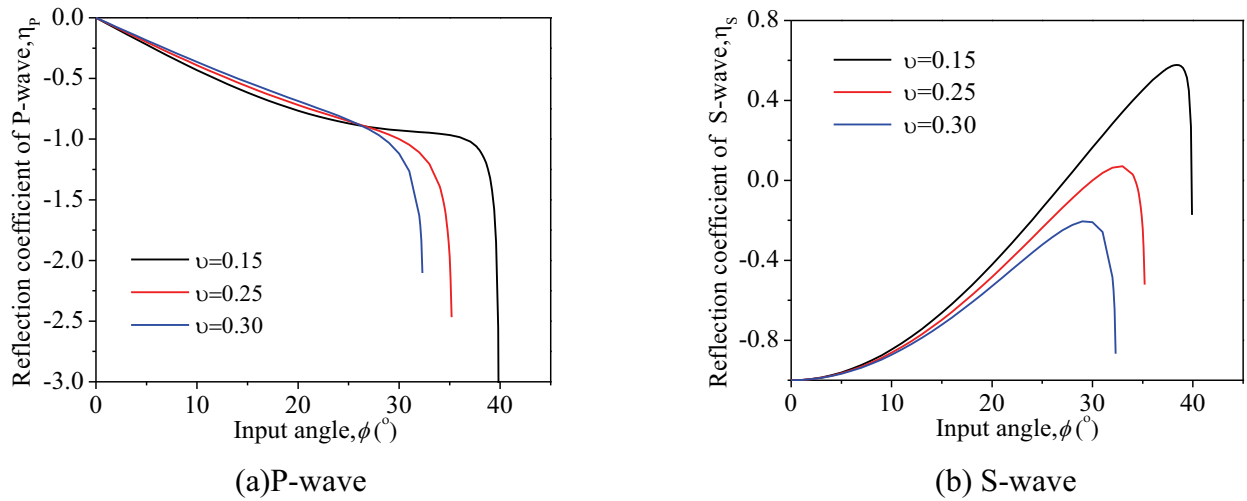


Figure 3.14 P-wave and S-wave reflection coefficients related to Poisson's ratio and input angle

According to the elastic wave hypothesis, the displacement formula of seismic wave (S_d) is taken first and second order derivation of time, velocity and acceleration formulae are obtained, as following Eq. (3.9), respectively:

$$S_v = -i\omega S_d \quad \text{and} \quad S_a = -\omega^2 S_d \quad (3.9)$$

$$\mathbf{S}_D = \mathbf{S}_d + \mathbf{S}'_d + \mathbf{S}''_d \quad (3.11)$$

In which, \mathbf{S}_d , \mathbf{S}'_d , \mathbf{S}''_d represent displacement vector of input S-wave, reflected S-wave and reflected P-wave, respectively.

Supposed displacement function of input wave is $f(t)$, then each wave at point D can be expressed as Eq.(3.12):

$$S_d = f(t+t_s) \quad S'_d = \eta_{sd} f(t+t_{ss}) \quad S''_d = \eta_{pd} f(t+t_{sp}) \quad (3.12)$$

In which t_s denotes duration of input S-wave from point C to point D; t_{ss} denotes duration from B passing point O_2 to point D; t_{sp} stands for duration from A passing point O_1 to point D. η_{pd} and η_{sd} are the P-wave and S-wave displacement reflection coefficients, respectively calculated by Eq. (3.7) and Eq.(3.8).

As shown in **Figure 3.15**, the global coordinate of point D is (x, y), then all of the durations can be calculated by Eq. (3.13).

$$\begin{cases} t_s = \frac{y}{v_s \cos(\phi - \theta)} \\ t_{ss} = \frac{y \cos \phi + (x \sin \theta - y \cos \theta) \cos(\phi + \theta)}{v_s \cos(\phi - \theta) \cos \phi} + \frac{x \sin \theta - y \cos \theta}{v_s \cos \phi} \\ t_{sp} = \frac{y \cos \psi + (x \sin \theta - y \cos \theta) \cos(\psi + \theta)}{v_s \cos(\phi - \theta) \cos \psi} + \frac{x \sin \theta - y \cos \theta}{v_p \cos \psi} \end{cases} \quad (3.13)$$

According to the principle of vectorial superposition, horizontal and vertical displacement at point D can be expressed as Eq. (3.14):

$$\begin{cases} S_{hor} = S'_d \cos(\phi + \theta) + S''_d \sin(\psi + \theta) - S_d \cos(\theta - \phi) \\ S_{ver} = S'_d \sin(\phi + \theta) - S''_d \cos(\psi + \theta) - S_d \sin(\theta - \phi) \end{cases} \quad (3.14)$$

where S_{hor} refers to horizontal component of displacement; S_{ver} refers to vertical component of displacement.

Therefore, displacement amplification ratio at point D is calculated by Eq. (3.15):

$$\xi_d = \frac{\sqrt{\max|S_{hor}^2 + S_{ver}^2|}}{\max|S_d|} \quad (3.15)$$

If seismic wave was considered as a simple harmonic wave, not taking damping into consideration, the velocity (ξ_v) and acceleration (ξ_a) amplification ratios are the same as the displacement amplification ratio, that is, $\xi_d = \xi_v = \xi_a$. Although this theoretical solution of slope dynamic responses is not completely consistent with the actual, however, the regularity of slope dynamic responses and the effects of parameters on slope stability can be revealed by making use of this theoretical solution. Therefore, Eq.(3.15) will be applied in following part.

3.3.3 The cases of analysis

Slope dynamic responses are affected by geomechanical parameters, seismic parameters and slope geometry shape. Young's modulus(E_d), Poisson's ratio (ν) and density (ρ) are representative variations of slope material parameters. Seismic wave parameters are comprised of wave amplitude, frequency (f) and transmitting duration (t) in the slope. According to Eq.(3.13), wave transmitting duration to wave superposition point is decided by input angle (ϕ) when geomechanical parameters and slope shape are constant, meanwhile, under the elastic hypothesis, wave amplitude do not affect displacement amplification ratio based on Eq.(3.15). Therefore, frequency (f) and input angle (ϕ) were used to stand for seismic wave parameters. The geometry shape of single linear surface slope can be described by slope angle (θ). Hence, displacement amplification ratio of dynamic responses can be expressed as following Eq. (3.16):

$$\xi_d = F(E_d, \nu, \rho, f, \phi, \theta) \quad (3.16)$$

In order to analyze the effect of each parameter on displacement amplification ratio, Eq.(3.15) was used to calculate 144 cases, which are the combination of different values of each parameter,

namely, $\theta=20^\circ, 30^\circ$; $E_d=3\text{GPa}, 6\text{GPa}$; $\nu=0.15, 0.25$; $\rho=2000\text{ kg/m}^3, 2700\text{ kg/m}^3$; $f=10\text{Hz}, 20\text{Hz}, 50\text{Hz}$; $\phi=10^\circ, 20^\circ, 30^\circ$. The parameters of nine typical cases out of 144 were listed in the **Table 3.6**, and the corresponding distribution regularity of displacement amplification ratios are shown in **Figure 3.16**.

Table 3.6 Different parameters of compared slopes

Case	Slope angle $\theta(^{\circ})$	Geomechanical parameters			Frequency f (Hz)	Seismic wave Input angle $\phi(^{\circ})$	Max(η_d)
		Young's modulus E_d (GPa)	Density ρ (kg/m ³)	Poisson's ratio, ν			
(a)	20	6	2700	0.15	10	20	1.94
(b)	20	3	2700	0.15	10	20	1.94
(c)	20	6	2000	0.15	10	20	1.94
(d)	20	6	2700	0.25	10	20	1.97
(e)	20	6	2700	0.25	20	20	1.97
(f)	20	6	2700	0.25	50	20	1.97
(g)	30	6	2700	0.15	10	10	1.99
(h)	30	6	2700	0.15	10	20	1.94
(i)	30	6	2700	0.15	10	30	1.86

*Hint: the cases with the same shading color were compared

3.3.4 The results and analyses of dynamic responses

3.3.4.1 Displacement amplification ratio related with parameters

Analytical results show that elevation amplification effect has been proved by this theoretical solution, that is, displacement amplification ratio increases with elevation in vertical direction. Meanwhile, displacement amplification ratio increases from slope inner to outer in the horizontal direction. The maximum of displacement amplification ratio, as shown in the Max(η_d) column of **Table 3.6**, relies on Poisson's ratio, input angle and slope angle. According to Eq. (3.12–3.15), the reason is inferred that displacement amplification ratio depends on the reflection coefficients of wave mode conversion, slope angle and input angle. Herein, reflection coefficients are further decided by Poisson's ratio, input angle and slope angle, as shown in Eq. (3.7) and (3.8).

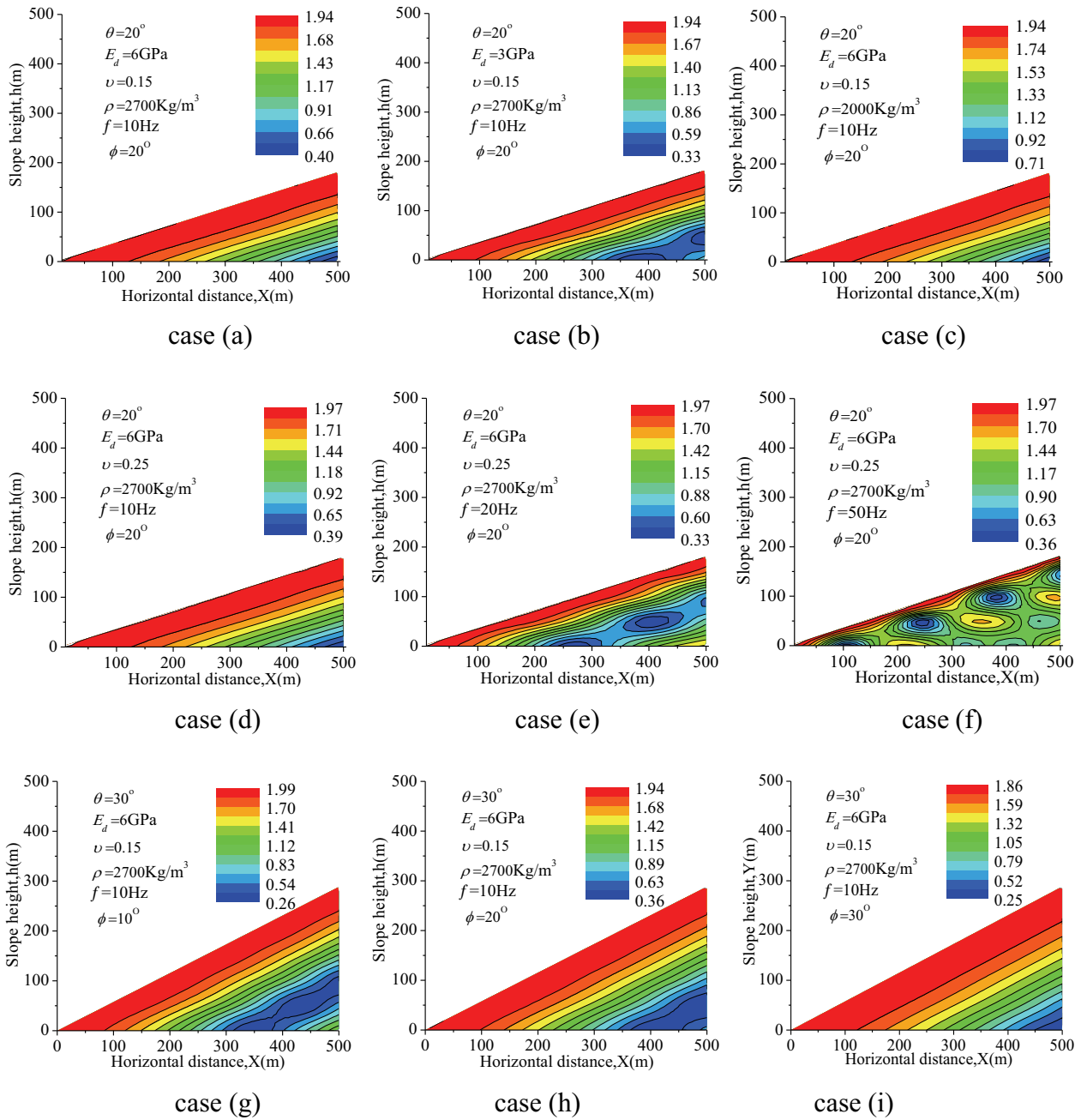


Figure 3.16 Contour plots of displacement amplification ratio related to different parameters

3.3.4.2 The effects of geomechanical parameters

Compared **Figure 3.16(a)** and **Figure 3.16(b)**, it suggests the distribution regularity of displacement amplification ratios and maximum value are almost the same even if Young's modulus reduces an half, but with Young's modulus increase, the thickness of the saliently

affected region(represented by red color in **Figure 3.16**) becomes thicker. The effect of density can be revealed by comparison between **Figure 3.16(a)** and **Figure 3.16(c)**. When density reduces 26%, the distribution regularity of displacement amplification ratios is similar to each other, maximum value is the same and minimum slightly increases. In a word, density has weaker effect on slope dynamic responses than Young's modulus, which can be explained by following Eq. (3.17):

$$v_p = \sqrt{\frac{E_d(1-\nu)}{\rho(1-2\nu)(1+\nu)}} \text{ and } v_s = \sqrt{\frac{E_d}{2\rho(1+\nu)}} \quad (3.17)$$

Eq.(3.17) suggests the velocity of P-wave and S-wave increases with Young's modulus and increases with the decrease of density, if the parameters of seismic wave, slope angle and Poisson's ratio keep constant, the seismic wave superposition point with the same displacement amplification ratio will be deeper away from slope inclined surface as a result of the velocity increase. Therefore, the saliently affected region in **Figure 3.16(a)** and (c) is thicker than that in **Figure 3.16(b)**. In generally, the absolute value variation of Young's modulus is much larger than that of density when slope material changing, therefore, Young's modulus is more influential than density on slope dynamic responses. The comparison of **Figure 3.16(a)** and **Figure 3.16(d)** suggests that the maximum of displacement amplification ratio slightly increases with the increment of Poisson's ratio and their distribution regularities of displacement amplification ratio are almost the same.

3.3.4.2 The effects of seismic wave parameters

With increment of seismic wave frequency, contour plots of displacement amplification ratios change from nearly parallel to the slope inclined surface to rhythm distribution with multiple peak values, the thickness of saliently affected region becomes shallower with frequency increase, as shown in **Figure 3.16(d)**, **Figure 3.16(e)**, and **Figure 3.16(f)**, which is consistent with that lower frequency causes severe damage during earthquake. **Figure 3.16(g)**, **Figure 3.16(h)**, and **Figure 3.16(i)** reveal that the maximum of displacement amplification ratio decreases with the

increment of input angle and the thickness of saliently affected region becomes thicker with input angle increase.

3.3.4.2 The effect of slope angle

Compared **Figure 3.16(a)** and **Figure 3.16(h)**, the result suggests that the distribution regularity and the values of displacement amplification ratio are almost the same, and the saliently affected region slightly becomes deeper when slope angle increases.

3.4 FEM analysis of slope shape on dynamic responses

Previous seismic observation suggests that topography played an important role in ground motion (Rogers et al., 1974; Griffiths and Bollinger, 1979; Tucker et al., 1984). In section 3.2 and 3.3, some topographical parameters of slope have been discussed, such as, slope angle, slope height. However, slope surface is so variable that it is difficult to be directly analyzed by investigation or theoretical derivation. Numerical analysis by software simulation is an effective approach to explore the seismic responses of slopes. Herein, it was applied to analyze the dynamic responses of different slopes with variable ground surface in this section, which is a supplementary of preceding analyses of influential factors on slope stability and dynamic responses in section 3.2 and 3.3.

3.4.1 Simplification of slope ground surface and numerical models

Although slope ground surface is very changeable, it may be generally simplified into five types according to geometrical shape, namely, step-like, concave, convex, S-like and inverse S-like, as shown in **Figure 3.17**. The 2-D numerical model of step-like slope is 45° slope angle, 30m slope height and 15m thickness of bedrock, as illustrated in **Figure 3.18**. The models of other four slopes were generated by replacing the inclined surface of step-like slope. Slope consisted of alluvial soil-rock aggregate and bedrock. The geomechanical parameters of these two rock types are listed in **Table 3.7**.

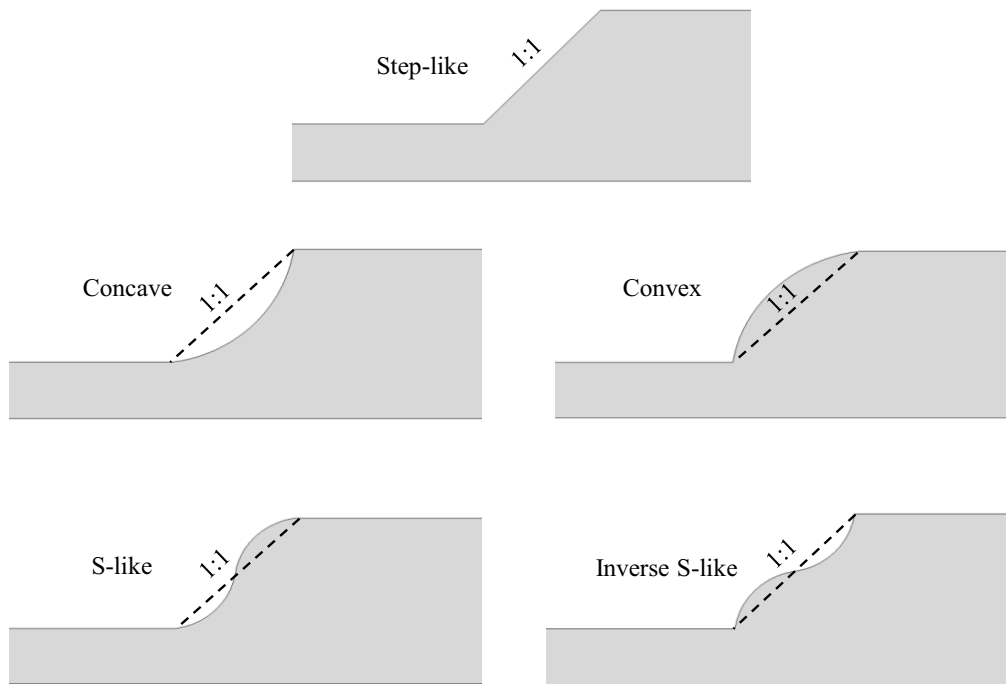


Figure 3.17 Sketches of five slopes with simplified ground surface

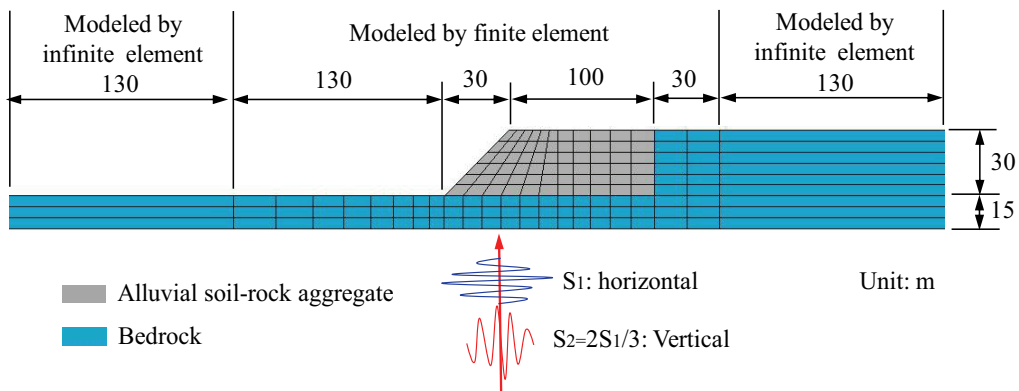


Figure 3.18 2-D numerical model of step-like slope

Table 3.7 Geomechanical parameters of slope materials

Rock type	Mass density, ρ (t/m^3)	Young's modulus, E_d (MPa)	Poisson's ratio, ν	Friction angle ($^\circ$), ϕ	Cohesion, c (KPa)
Alluvial soil-rock aggregate	2	40	0.3	35	40
Bedrock	2.5	8000	0.27	43	850

Because boundary conditions at the truncated edges of the finite element mesh may reflect energy back, meanwhile, it is not always reliable to extend the finite element mesh to deal with the boundary of numerical model, particularly in dynamic analysis. Hence, a better approach is to use “infinite element”, which was defined over semi-infinite domains with suitably chosen decay functions. These functions were considered in infinite element of Abaqus software by setting boundary damping. This approach is based on the work of Lysmer and Kuhlemeyer (1969) for dynamic analysis. The infinite elements modeling the far-field region are used in conjunction with standard finite elements, which simulates the area around the region of interest. In **Figure 3.18**, the elements located in lateral sides are infinite elements with 130m length, as long as the distance between finite element edges and slope top or foot, as so to meet the smallest region requirement of infinite element usage. Since the solution in the far field is assumed to be linear, hence, only linear behavior parameters are needed for infinite elements.

For the interest domain, it was simulated by finite element, and its damping was considered as classical Rayleigh damping, which uses a system damping matrix $[C]$ defined as:

$$[C]=\alpha [M] +\beta [K] \quad (3.18)$$

where

α is the mass proportional Rayleigh damping coefficient;

β is the stiffness proportional Rayleigh damping coefficient;

$[M]$ is the system structural mass matrix;

$[K]$ is the system structural stiffness matrix.

Classical Rayleigh damping results in different damping ratios for different frequencies according to the following equation:

$$\xi = \frac{\alpha}{2\omega} + \frac{\beta\omega}{2} \quad (3.19)$$

where, ξ is damping ratio, a value of 1 corresponds to critical damping. It is generally accepted that slope has damping ratio of about 2%–5%. During simulation, $\xi=2\%$ was used; ω is circular frequency (rad/s). Significant dynamic response is usually corresponded to the range of 0.5–5Hz, herein, supposed $f_1=0.5\text{Hz}$ and $f_2=5\text{Hz}$. Substituting these two boundary frequencies into Eq.(3.19), then

$$\left. \begin{aligned} \xi &= \frac{\alpha}{2\omega_1} + \frac{\beta\omega_1}{2} \\ \xi &= \frac{\alpha}{2\omega_2} + \frac{\beta\omega_2}{2} \end{aligned} \right\} \quad (3.20)$$

that is,

$$\left. \begin{aligned} \alpha &= \frac{2\xi\omega_1\omega_2}{\omega_1 + \omega_2} \\ \beta &= \frac{2\xi}{\omega_1 + \omega_2} \end{aligned} \right\}$$

Solving Eq. (3.20), obtaining damping coefficients for numerical models, $\alpha=0.11424$, $\beta=1.157 \times 10^{-3}$.

3.4.2 Seismic source waves

Seismic ground motion was inputted into numerical model from bottom by recorded acceleration time history. In order to make results be relatively more universal, three typical earthquake seismic records would be applied. The first is from 2008 Wenchuan earthquake at Wolong station in EW direction, illustrated in **Figure 3.19**. The peak ground acceleration is 965.06gal, and lasted more than 150s, but previous 50s recorded data were used. The second is from 1940 El Centro (Imperial Valley) Earthquake, as shown in **Figure 3.20**, and making use of previous 40s data as source wave. The third one is from 1995 Kobe earthquake (Great Hanshin earthquake), as shown in **Figure 3.21**. All of these records were adjusted PGA to 0.1g, and then inputted into aforementioned five slopes in horizontal direction, respectively; meanwhile, vertical acceleration, 2/3 of horizontal acceleration, was implemented simultaneously on each slope from model bottom.

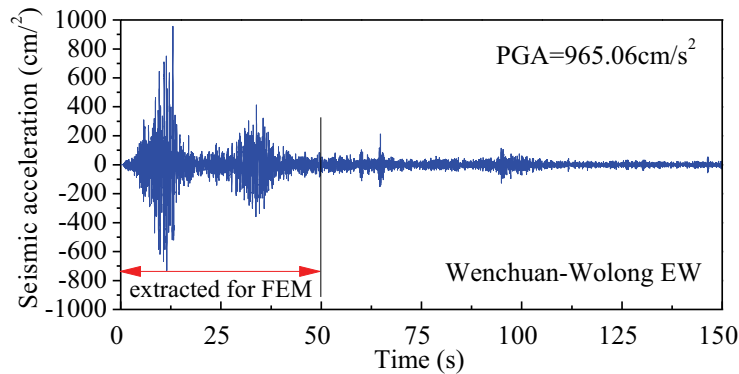


Figure 3.19 Typical acceleration time history of Wenchuan earthquake

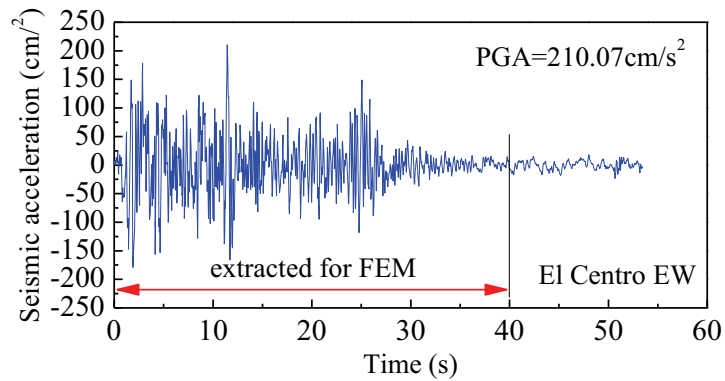


Figure 3.20 Typical acceleration time history of El Centro earthquake

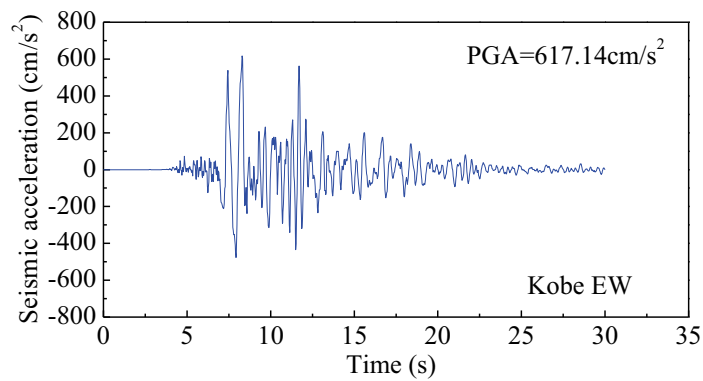


Figure 3.21 Typical acceleration time history of Kobe earthquake

3.4.3 The influence on vibration mode

The vibration modes of five typical slopes were extracted and shown in **Figure 3.22**, which suggests that natural frequencies of preceding five modes among these slopes are almost the same; with the mode increase, the natural frequencies of each slope are slightly different from each other. Generally, the natural frequency of concave slope is larger than others and followed by step-like slope, inverse S-like slope, S-like slope, and convex slope has relatively smallest natural frequency.

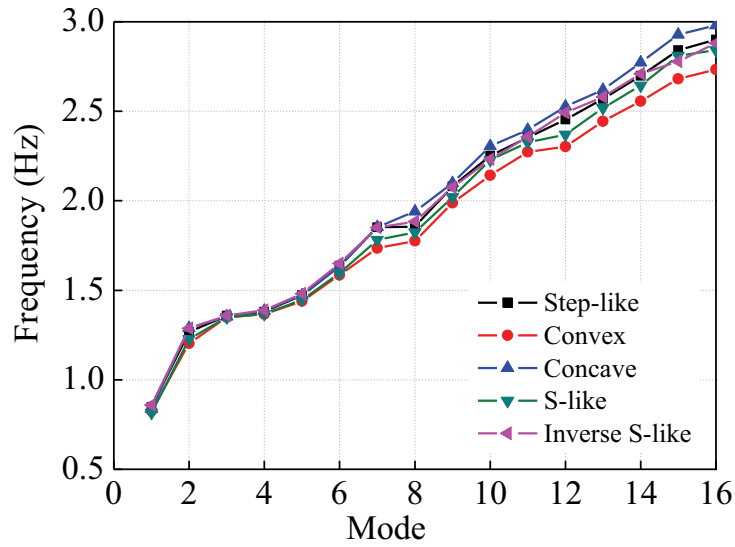


Figure 3.22 Natural frequency comparison among five typical slopes

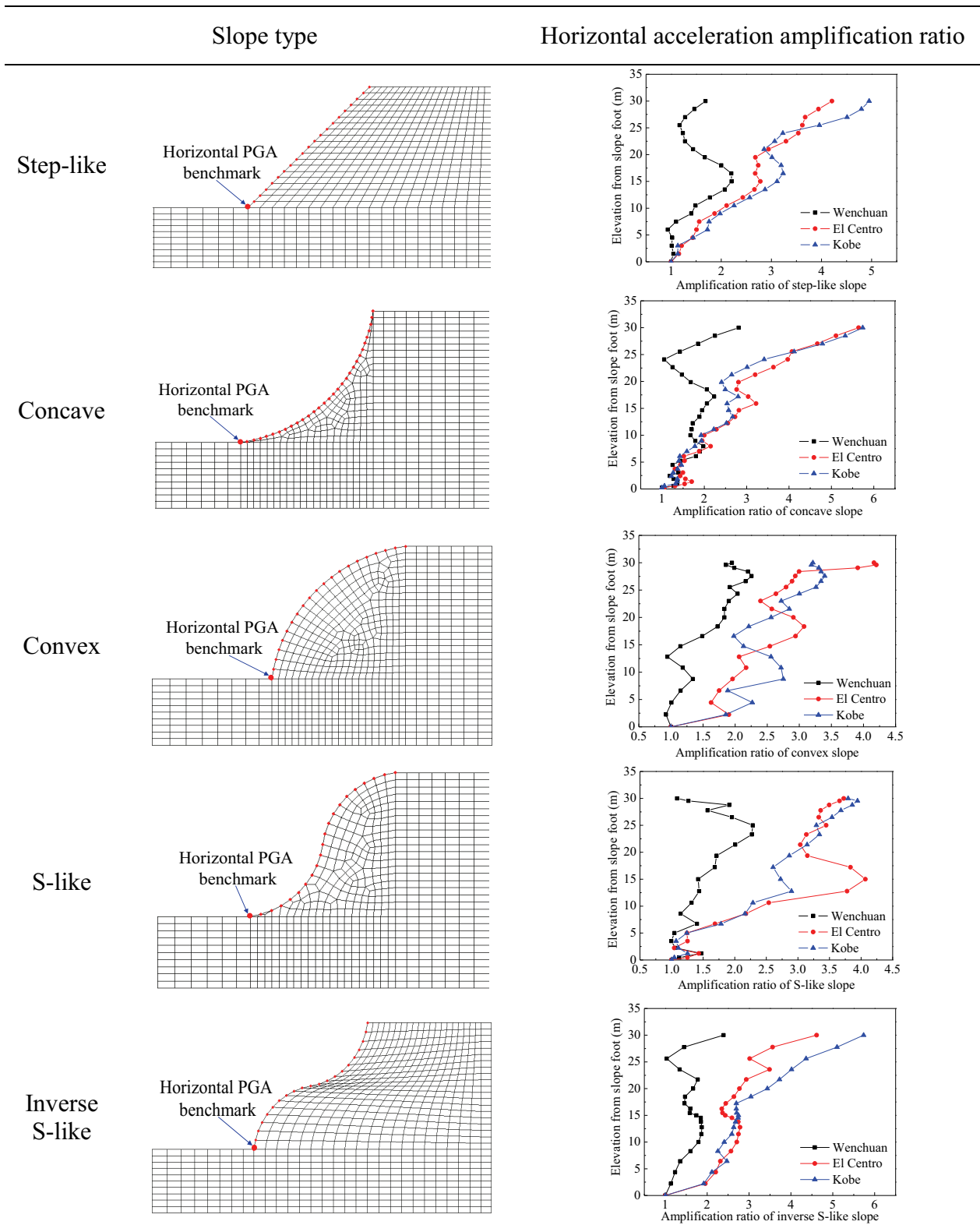
3.4.4 The influence on acceleration amplification

Topographical amplification effect of five typical slopes was explored by using acceleration amplification ratio (ξ_a), which was termed as the ratio of horizontal peak ground acceleration of each node along slope inclined ground surface to the horizontal peak ground acceleration of slope toe, namely,

$$\xi_a = \frac{\text{Horizontal PGA along slope inclined ground surface}}{\text{Horizontal PGA at slope toe}}$$

The acceleration amplification ratio of each slope along inclined ground surface was listed in **Table 3.8**, which suggests that seismic acceleration was generally amplified with the increment of slope elevation, especially, at the steep section, i.e. the top section of concave slope and inverse S-like slope, and ground surface curvature sharp changing section, i.e. the middle section of S-like slope and inverse S-like slope; meanwhile, the amplification effects of different seismic source waves are different from each other. The effects of El Centro seismic wave and Kobe seismic wave are much more apparent than that of Wenchuan seismic wave; it may be caused by the spectral characteristics of seismic source wave.

Table 3.8 Acceleration amplification ratio of five simplified slopes with different shapes



3.4.5 The influence on equivalent plastic strain

Slope becomes instability due to the degradation of slope materials; hence, the plastic zone of five typical slopes would be explored by the distribution of equivalent plastic strain. Three types of seismic source wave with 0.1g horizontal PAG and 0.067g vertical PGA were inputted into each slope simultaneously, and the contour plots of equivalent plastic strain were listed in **Table 3.9**, which suggests that convex slope and S-like slope are much easier to develop plastic strain under anyone of these three seismic source waves, and followed by concave slope and inverse S-like slope; step-like slope appears weakest invulnerability among five typical slope. This comparison of equivalent plastic strain implies that slopes with convex and S-like shape are much more unstable than other three shapes of slope during earthquakes; step-like slopes have relatively higher stability; concave slopes and inverse S-like slopes have medium stability.

3.5 Summary

This chapter made use of three kinds of method to analyze the influential factors on slope stability and dynamic responses; some findings were summarized as follows:

- Based on the statistical analysis of 119 landslides in Wenchuan County
 - (1) Landslide occurrence probability decreased with the increment of distance from the surface fault rupture, and increased with the horizontal peak ground acceleration.
 - (2) High and steep slopes consisting of soft rock were more likely to be triggered as landslides.
 - (3) Geological structures had significant effect on slope stability, and rock layer with more than 10° gradient in the same direction of slope inclination, namely GS2 geological structure, were relatively more susceptible to sliding.
 - (4) The multivariable analysis revealed that the square root of sliding source area and cubic root of sliding source volume were linearly correlated with the combination of slope height, horizontal peak ground acceleration, inclination of rock layer, slope angle and rock type.
 - (5) Stepwise regression results suggested that slope height, horizontal peak ground acceleration and geological structure were more influential to sliding source area and volume than slope angle and rock type during earthquake. Since sliding source area and volume are two most important impact factors of slope failure, the results implied that slope height, horizontal peak ground acceleration and geological structure had predominant influence on slope stability during earthquake among investigated five influential factors.
- Based on the theoretical derivation of slope dynamic responses
 - (1) Theoretical solution has proved the elevation amplification effect. With elevation increase, displacement (velocity, acceleration) amplification ratio becomes larger; meanwhile, amplification ratio turns larger from slope inner to the outer.
 - (2) The shape of contour plot of displacement amplification ratio is determined by seismic wave frequency; with the increment of frequency, the contour plot changes from nearly parallel to slope surface to rhythm distribution with multiple peak values. Lower frequency induces more dangerous dynamic responses.

- (3) The maximum displacement amplification ratio relies on Poisson's ratio, input angle of seismic wave and slope angle.
 - (4) Mass density has smaller effect on slope dynamic responses than Young's modulus.
 - (5) The thickness of saliently affected region by earthquake becomes larger with the increase of Young's modulus and seismic wave input angle, and with the decrease of seismic wave frequency.
- Based on numerical simulation of slope dynamic responses
 - (1) Slope surface geometry shape has very limited influence on natural frequency of low order vibration mode.
 - (2) Seismic acceleration was generally amplified with the increment of slope elevation, especially, at the steep section and ground surface curvature sharp changing section.
 - (3) Slopes with convex and S-like shape are much more unstable than other three shapes of slope during earthquakes; step-like slopes have relatively higher stability; concave slopes and inverse S-like slopes have medium stability.

References

- Aydan, Ö., Ohta, Y., Hamada, M., et al., 2009a. The characteristics of the 2008 Wenchuan earthquake disaster with a special emphasis on rock slope failures, quake lakes and damage to tunnels, *Journal of the School of Marine Science and Technology, Tokai University*, 7(2), 1–23.
- Aydan, Ö., Hamada, M., Itoh, J. et al., 2009b. Damage to civil engineering structures with an emphasis on rock slope failures and tunnel damage induced by the 2008 Wenchuan earthquake. *Journal of Disaster Research*, 4(2), 153–164.
- Chang, S.B., Zhang, S.M., et al., 2006. *Manual of Engineering Geology (Fourth edition)*, China architecture & building press, 17-18. (In Chinese)
- Davis, L. L., West, L. R., 1973. Observed effects of topography on ground motion. *Bulletin of the Seismological Society of American*, 63(1), 283-298.

- Goodman, R.E., Bray, J.W., 1976. Toppling of rock slopes in rock engineering for foundation and slopes. Proc. of a specialty conference, Vol.2, pp.201-233, Am. Soc. Civ. Eng., New York.
- Griffiths, D. W. and Bollinger, G. A., 1979. The effect of appalachian mountain topography on seismic waves. Bulletin of the Seismological Society of America, 69(4), 1081-1105.
- Hu, J.X. et al. ,2006. Earthquake engineering, Seismological Press, Beijing. PP16-24
- Ji. C., Hayes, G., 2008. Finite fault model-preliminary result of the May 12, 2008 Mw7.9 eastern Sichuan, China earthquake. Information from website: <http://earthquake.usgs.gov/earthquakes/eqinthenews/2008/us2008ryan/>
- Lysmer, J. and Kuhlemeyer, R.L., 1969. Finite dynamic model for infinite media. Journal of the Engineering mechanics Division, Proc. ASCE, 95(4), 859-878.
- Lin, M.L., Wang, K.L., 2006. Seismic slope behavior in a large-scale shaking table model test. Engineering geology, 86, 118-133.
- Rogers, A. M., Katz, L. J. and Benett, T. J., 1974. Topographic effect on ground motion for incident P waves: a model study. Bulletin of the Seismological Society of America, 64(2) 437-456.
- Tucker, B. E., et al., 1984. Observations of hard rock site effects, Bulletin of the Seismological Society of America, 74(1), 121-136.
- Xu, G. X., Yao, L.K., Gao, Z.N., 2008a. Large-scale shaking table model test on the dynamic characteristics and seismic responses of slope. Chinese Journal of Rock Mechanics and Engineering, 27(3), 624-632. (In Chinese with English abstract)
- Xu, G. X., Yao, L.K., Li, Z.H., 2008b. Dynamic response of slopes under earthquakes and influence of ground motion parameters. Chinese Journal of Rock Mechanics and Engineering, 30(6), 918-923. (In Chinese with English abstract)

Chapter 4 Influential Factors on Landslide Mobility and Travel Distance

4.1 Introduction

Landslide travelling at “rapid” post-failure velocity or long runout may result in loss of life, destruction of property, damage to the natural environment; because persons in the travel path of these types of landslide cannot timely evacuate and the kinetic energy of failed mass is so large that it can severely destroy buildings and other infrastructure, even small landslide. After Wenchuan earthquake, numerous authors have analyzed the relations between landslide spatial distribution and influential factors (Huang and Li, 2008, 2009a, 2009b; Xu et al., 2009b, 2010; Chigira et al., 2010; Qi et al., 2010; Dai et al., 2011; Gorum et al., 2011; Xu and Xu, 2012; Xu, et al., 2013a, b). However, there are few studies on landslide mobility and travel distance, expect that Qi et al. (2011) delineated six typical destructive long travel landslides and listed 66 valuable cases, but just analyzed the relationships between elevation loss & sliding area and travel distance. In fact, at least 112 relatively large landslides (volume $>5\times 10^4\text{m}^3$) have been triggered during Wenchuan earthquake along seismic source faults (Xu et al., 2009a). High mobility landslide had large potential to travel long away, resulting in the debris to block the valley and then generate landslide dam to endanger down-stream area, such as Tangjiashan landslide dam. During Wenchuan earthquake, 34 landslide dams accompanied with those relatively large landslides (Xie et al., 2008); meanwhile, at least 4,970 sites had high potential to develop into slope failures (Yin et al., 2009). September 24, 2008 in Beichuan County, heavy rain induced 72 landslides (mainly debris flow) and caused 42 deaths and severe damage in the relocation area; August 8, 2010 in Zhouqu City, one of the earthquake-affected area, a huge debris flow caused 1434 deaths (Tang, et al., 2012). Two fatal events suggested that the area affected by Wenchuan earthquake was seriously vulnerable. Hence, it is essential to explore the mobility of sliding mass after slope failure. In order to assess the hazard caused by high mobility or long travel landslides, it is

necessary to firstly identify what factors had effect on landslide mobility, and then explore how to evaluate the mobile ability of sliding mass after slope failure, and how to estimate its post-failure travel distance. Hence, this chapter would discuss these issues.

4.2 Data source

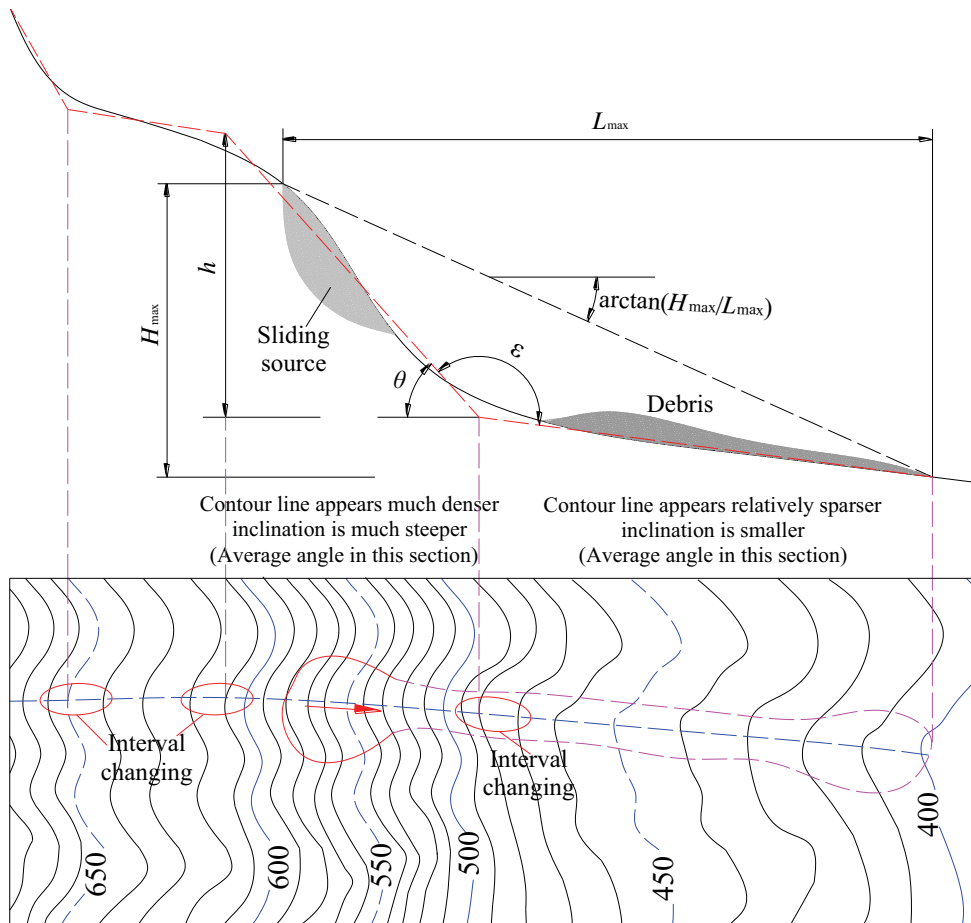


Figure 4.1 The sketch of landslide and its deposit for terminological definition

In this section, some terminologies and methodology of data collection would be briefly introduced.

Making use of topographic map to obtain the longitudinal profile of a slope; based on the density of contour lines, slope was divided into several segments. Contour lines appear relatively sparser, the inclination of corresponding segment will be smaller, and the contour lines become

much denser, the corresponding segment has relatively larger slope angle. The interval changing segments of contour lines (marked by ellipse in **Figure 4.1**) along longitudinal section correspond with the inclination changing segments along a slope. The boundary of contour line interval apparent changing in the topographic map along slope longitudinal section was regarded as the turning point of different segments of a slope, hence, a slope will be divided into several segments, and the average inclination and slope height of each segment will be obtained. Slope angle, θ , is the average inclination of the sectional slope with failed part. Slope height, h , is the elevation difference of the sectional slope with failed part. Slope transition angle, ε , is the angle between the upper slope (failed section) and lower slope, which represents the change degree of slope inclination. Travel distance, L_{\max} , is the horizontal distance between the crest of the sliding source and the distal of debris. Landslide height, H_{\max} , is the maximum elevation loss between sliding source and debris. $\arctan(H_{\max}/L_{\max})$ represents fahrböschung (Heim, 1932) or travel distance angle (Hunter and Fell, 2003). All of these notations are shown in **Figure 4.1**.

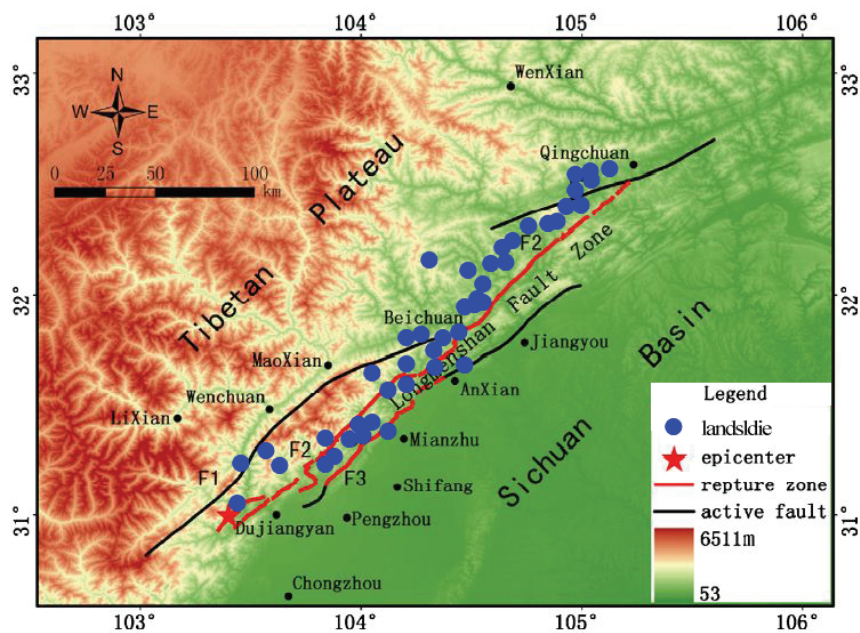


Figure 4.2 The location of 46 landslides in Wenchuan earthquake area; F1 represents Wenchuan-Maoxian fault, F2 represents Yingxiu-Beichuan fault, F3 represents Guanxian-Anxian fault. (Based on Qi. et al., 2011)

In this chapter, the collected data excluded not only landslides obstructed by relatively large river, valley and infrastructure but also travel path sharply confined by lateral steep slope and landslides with big deflection travel path, as a result of that the attributes of travel path had significant effect on the mobilization of failed mass (Shaller, 1991; Corominas, 1996). However, the characteristics of confinement are difficult to be quantitatively expressed, hence, the travel path of selected landslides was relatively open or confined by gentle lateral slope, and the travel path with relatively small deflection. Totally, 46 landslides with 9 parameters were collected based on remote sensing interpretation, field investigation and descriptions of published papers and books. The source volume range of these landslides is $4.5 \times 10^4 - 2.75 \times 10^7 \text{m}^3$; horizontal travel distance is within 347–4170m. The distribution of these 46 landslides in Wenchuan earthquake area was illustrated in **Figure 4.2**.

The sliding source area of a landslide was calculated by ArcGIS software based on topographic map. Landslide source volume was estimated from sliding source area multiplied by average collapse depth of sliding source body. The average collapse depth was obtained from slope typical longitudinal profile, as shown in **Figure 4.3**.

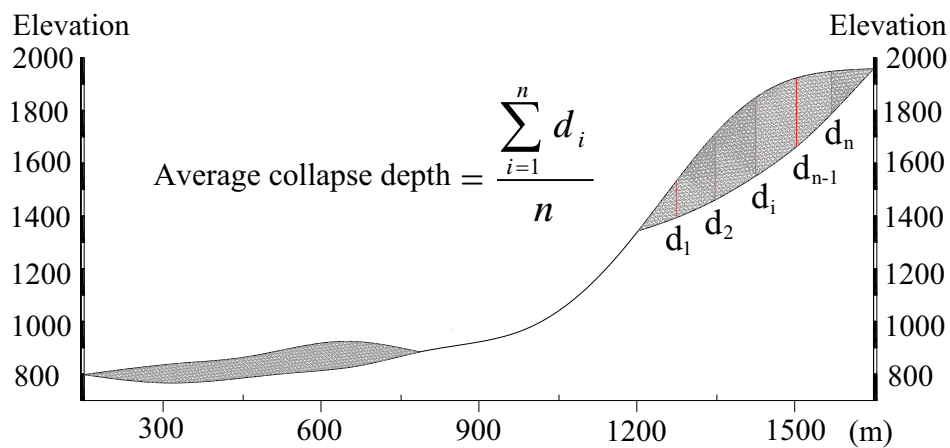


Figure 4.3 Typical longitudinal profile of a long travel landslide

According to the strength and weathered degree, rock materials were classified into two types, such as hard rock and soft rock, further, divided into two subclasses, respectively, as listed in **Table 3.1**.

In order to estimate seismic acceleration, Eq. (3.1) with parameters listed in **Table 3.2** was used to calculate horizontal peak ground acceleration (PHA) of each landslide.

The parameters of 46 investigated landslides triggered by the 2008 Wenchuan earthquake were listed in **Appendix Table 3**.

4.3 Relationships between landslide travel distance and landslide parameters

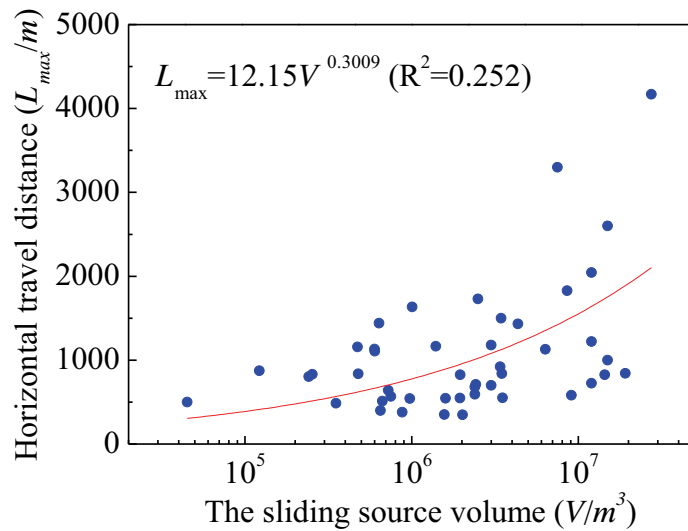


Figure 4.4 Landslide travel distance related with sliding source volume

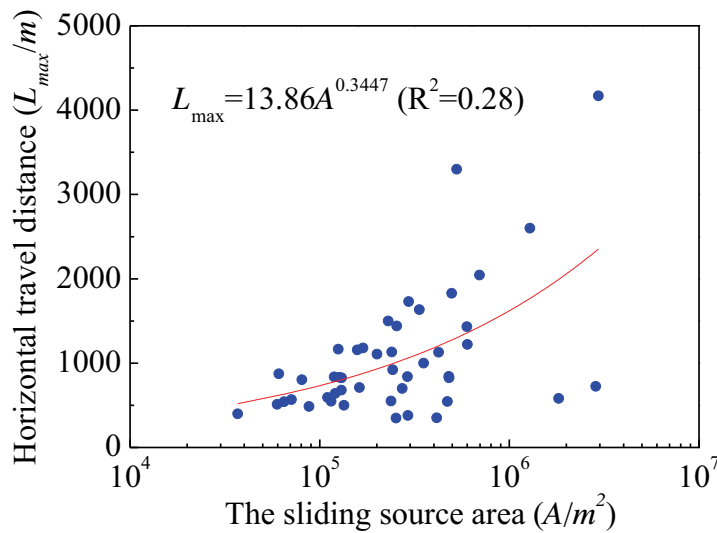


Figure 4.5 Landslide travel distance related with sliding source area

Figure 4.4 and **Figure 4.5** illustrate the relations between landslide travel distance and sliding source volume and area, respectively; nevertheless, the statistical significance level is relatively weak, but they both suggest that landslide travel distance had an exponential correlation with landslide scale (sliding source volume and area); it means landslide travel distance generally and rapidly increased with landslide scale.

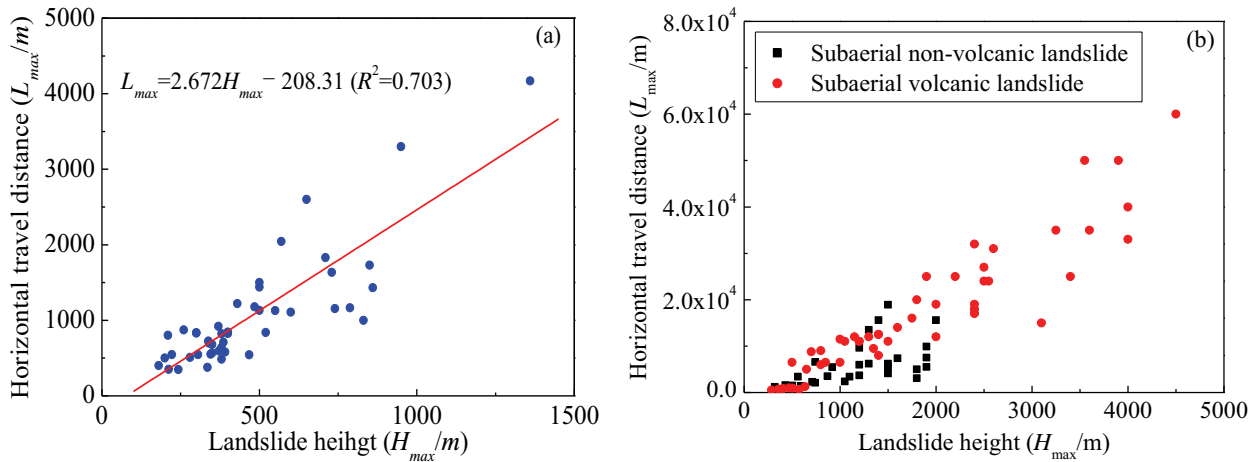


Figure 4.6 Landslide travel distance related with landslide height. (a) Wenchuan earthquake-induced 46 landslides; (b) non-volcanic and volcanic landslides (data from Hayashi and Self, 1992; Legros, 2002)

Figure 4.6(a) illustrates that horizontal travel distance (L_{max}) of these 46 landslides triggered by Wenchuan earthquake had a relatively strong linear correlation with landslide height (H_{max} , total elevation loss). The relation between landslide horizontal travel distance and landslide height were further explored based on non-volcanic and volcanic landslides (Hayashi and Self, 1992; Legros, 2002), as shown in **Figure 4.6(b)**, which also suggests that landslide travel distance increased with the elevation loss of failed mass. The reason was attributed to that failed mass was forced to travel down by gravity, and the potential energy was transformed to kinetic energy, which was consumed by friction and collision; finally, failed mass was decelerated and deposited. Total elevation loss (H_{max}) implies the total loss of potential energy on the existing topography, hence, the larger landslide height (H_{max}) was, the farther failed mass traveled.

Because of strong correlation between landslide travel distance and total elevation loss, equivalent coefficient of friction, the ratio of total elevation loss to maximum travel distance ($\mu =$

H_{\max}/L_{\max} ; Shreve, 1968; Scheidegger, 1973), was used to indirectly express landslide mobility after slope failure in the following discussion. This index is equal to the tangent of fahrböschung angle (Heim, 1932), $\arctan(H_{\max}/L_{\max})$, namely, angle of reach (Corominas, 1996), travel distance angle (Hunter and Fell, 2003). The inverse of equivalent coefficient of friction ($1/\mu$) expresses landslide mobility, that is, the small μ , the stronger landslide mobility.

4.4 Qualitative analysis of influential factors on landslide mobility

4.4.1 The effects of topographical factors

Topographical factors play an important role in landslide mobility (Okura et al., 2003), herein, three parameters would be discussed, such as slope angle (θ), slope transition angle (ε) and slope height (h).

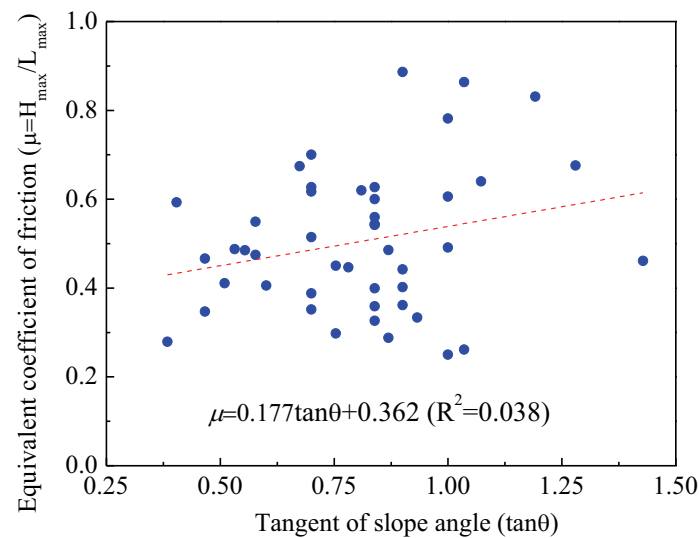


Figure 4.7 Equivalent coefficient of friction related with tangent of slope angle

Statistical result, shown in **Figure 4.7**, suggests that equivalent coefficient of friction of landslide induced by Wenchuan earthquake had a positive, but weak, correlation with tangent of slope angle. It implied that landslide mobility ($1/\mu$) decreased with the increment of slope angle (θ), which is attributable to the positive correlation between internal friction coefficient and slope angle (Okura et al., 2003), that is to say, kinetic energy consumed by internal friction has

positive correlation with slope angle; meanwhile, the steeper the slope is, the higher consumption of kinetic energy due to impact at the foot of upper slope. Therefore, the likelihood of high mobilization landslide was relatively low to occur on the steep or very steep slope. This general tendency related with the tangent of slope angle of earthquake-induced landslides is consistent with previous studies on non-seismic landslide (Okura et al., 2003; Hunter and Fell, 2003; Hattanji and Moriwaki, 2009, 2011).

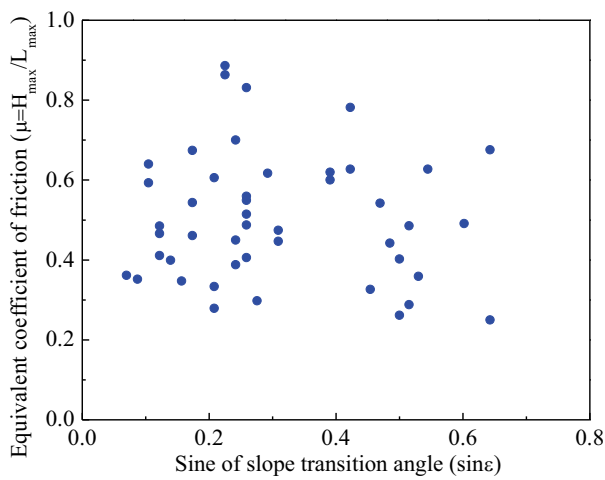


Figure 4.8 Equivalent coefficient of friction related with sine of slope transition angle

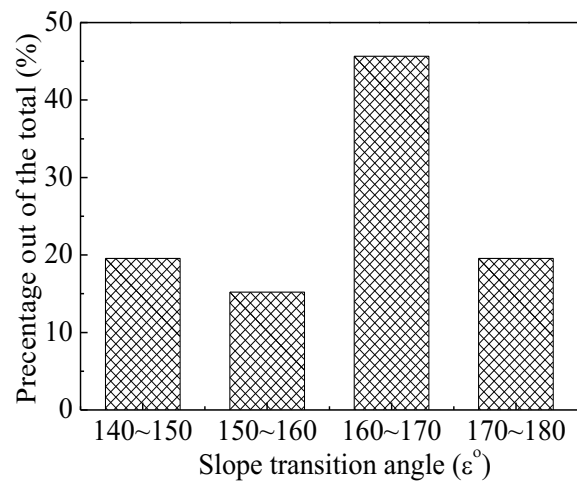


Figure 4.9 Statistical histogram of slope transition angle

The changing degree of slope inclination was represented by slope transition angle (ϵ). The relationship between equivalent coefficient of friction and sine of slope transition angle was illustrated in **Figure 4.8**, which suggests that there was no statistical correlation and tendency. However, the histogram in **Figure 4.9** shown that 45% landslides in this data set concentrated in the range of 160° - 170° slope transition angle. It may be explained by that when slope transition angle was relatively small, a large amount of kinetic energy was dissipated by serious impact due to the large inclination change between upper slope and lower slope. With the increment of slope transition angle, energy consumed by impact at slope foot decreased, and the falling mass was crushed and resulted in the transform of mobile motion from sliding to rolling or flowing, then residual energy driven rolling or flowing mass to travel relatively longer. However, when slope transition angle was large enough to ignore the topographical slope change, the motion of failure mass was highly probable to slide as a relatively intact quasi-rigid body, then kenetic energy

would be consumed by sliding friction. As a result of sliding motion generally consumed more kinetic energy than rolling or flowing motion, then sliding mass would be decelerated faster than rolling or flowing mass, therefore, landslides within the group of 170° – 180° slope transition angle became fewer than those in 160° – 170° .

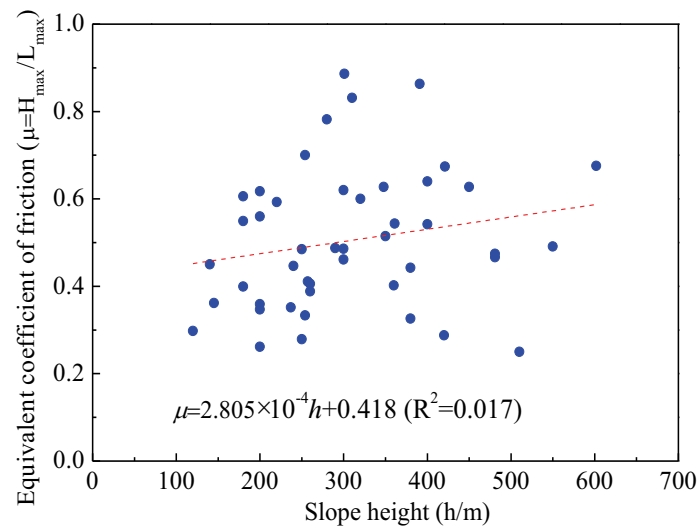


Figure 4.10 Equivalent coefficient of friction related with slope height

The relation between equivalent coefficient of friction and slope height was shown in **Figure 4.10**. Although statistical correlation is very weak, the general tendency suggests that equivalent coefficient of friction increased with the increment of slope height. It may be explained by that slope height implies the potential energy of failed mass and governs the available space to accelerate the failed mass, the higher slope height was, the larger velocity was, resulting in the loss of kinetic energy by impact increased with slope height. When larger kinetic energy was consumed, landslide mobility ($1/\mu$) would be lower, namely, it caused equivalent coefficient of friction (μ) had positive correlation with slope height.

4.4.2 The effect of seismic acceleration

In order to explore the trend between landslide mobility and seismic ground motion, the formulae, as Eq.(3.1), were used to estimate horizontal peak ground acceleration of each

landslide. The result was illustrated in **Figure 4.11**, which suggests that equivalent coefficient of friction had no correlation with peak ground acceleration. It implies that seismic acceleration had little effect on landslide movement. Backward analyzing the scale of 46 landslides, it was found that the volumes of these landslides were in the range of $4.5 \times 10^4 - 2.75 \times 10^7 \text{ m}^3$, 65% landslide volumes are larger than 10^6 m^3 , and 39 volumes out of the total were larger than $5.0 \times 10^5 \text{ m}^3$. From the viewpoint of earthquake energy, Kokusho et al. (2009) proposed that the potential energy of very large landslide would be big enough to ignore the effectiveness of earthquake energy on landslide movement; the effect of earthquake was playing a trigger role rather than making landslide have higher mobility and drive sliding mass to travel long away. Herein, the results of these 46 landslides gave an evidence to the statement of Kokushao et al.(2009).

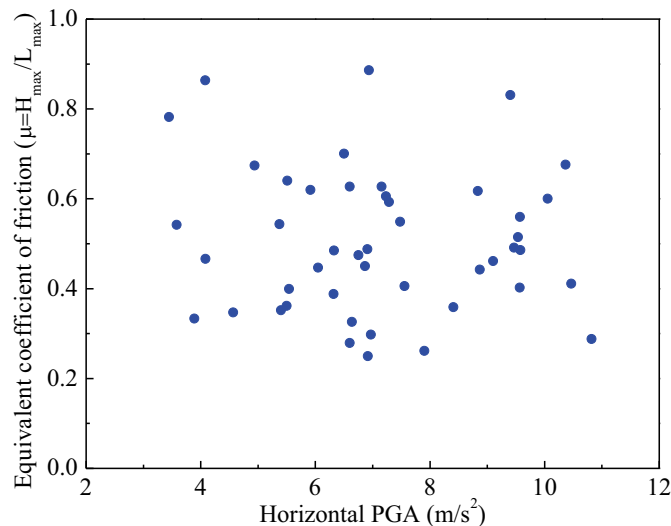


Figure 4.11 Equivalent coefficient of friction related with seismic acceleration

4.4.3 The effect of rock type

Rock type is another influential factor on landslide mobility. Because landslide usually had very changeable rock type along travel path, herein, discussed lithology was limited within the sliding source range for the typical rock type. According to rock strength and weathered degree, rock materials were classified into two types and four sub-classes, as shown in **Table 3.1**. The statistical result was illustrated in **Figure 4.12**, which suggests that equivalent coefficient of friction of hard rock was within a smaller range than that of soft rock, indicating that landslides

consisting of hard rock had higher mobility (smaller μ) than those consisting of soft rock. The reason might be caused by that the sliding friction coefficient between soft rock and travel path was larger than that of hard rock; besides, it might be caused by the difference of mobile mechanics. The behavior of soft rock was possible to be viscoplasticity, while the behavior of hard rock was probable to be plasticity; hence, soft rock consumed more kinetic energy than hard rock along travel path, resulting in equivalent coefficient of friction of soft rock landslide distributed within a larger range.

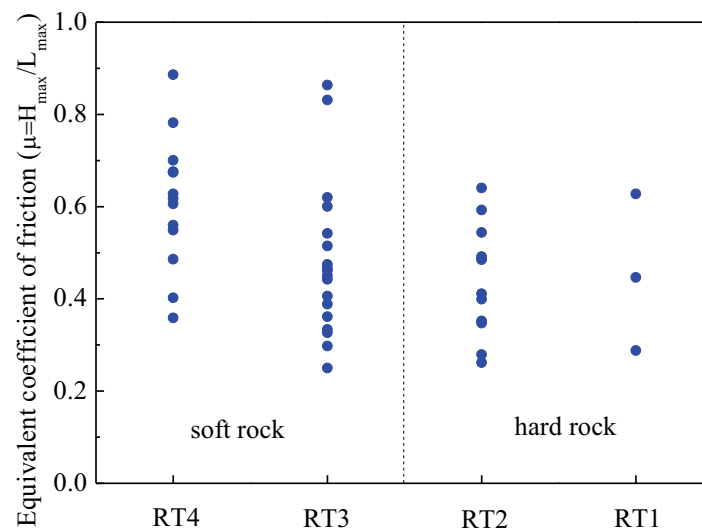


Figure 4.12 Equivalent coefficient of friction related with rock type

4.4.4 The effect of landslide volume

There are lots of previous studies on the relationship between landslide mobility and sliding volume induced by non-seismic causes (Scheidegger, 1973; Hsü, 1975; Corominas, 1996; Legros, 2002; Okura et al. 2003). Scheidegger (1973) stated a log-log linear correlation between landslide volume and equivalent coefficient of friction when volume beyond 10^5m^3 ; Hsü (1975) stated the threshold value of landslide volume was $5 \times 10^5\text{m}^3$. However, there are few studies on the relationship between landslide volume and its mobility induced by earthquake. Based on these 46 landslides induced by the 2008 Wenchuan earthquake, an empirical formula with highly statistical significance cannot be obtained, nevertheless, **Figure 4.13** suggests there was a generally

decreasing tendency between equivalent coefficient of friction and sliding source volume, especially, excluding four landslides smaller than $2.55 \times 10^5 \text{ m}^3$.

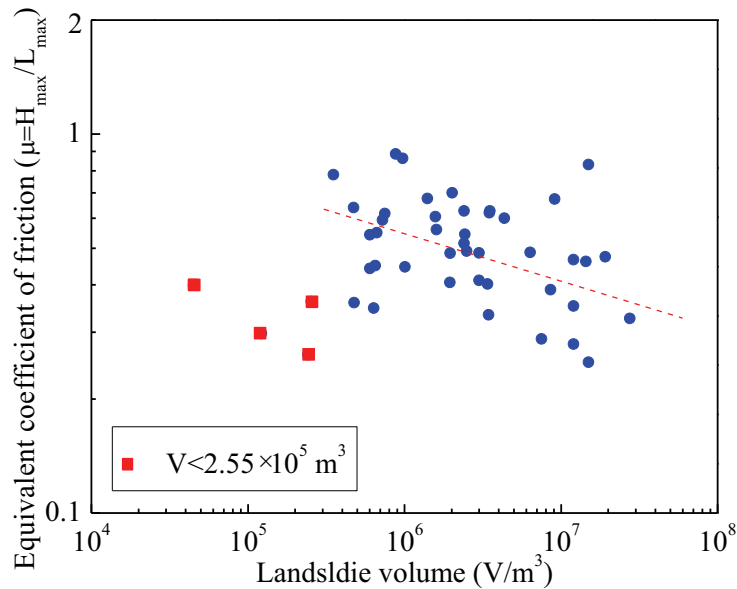


Figure 4.13 Equivalent coefficient of friction related with landslide source volume

4.5 Statistical model of landslide mobility

Based on one by one qualitative analysis of the general tendencies between equivalent coefficient of friction and 6 influential factors in section 4.4, the results suggests that each influential factor had more or less effect on landslide mobility ($1/\mu$), but the statistical correlation between equivalent coefficient of friction (μ) and each influential factor is very weak, even no correlation, it implies that if only considering one influential factor, it was impossible to obtain a reliable regression model to estimate landslide mobility based on these 46 landslides triggered by the 2008 Wenchuan earthquake; it also implies that landslide mobility was not affected by one main factor but simultaneously affected by numerous factors. As a result of numerous influences on landslide mobility, in order to clarify which factor/factors is/are predominant, multivariable analysis would be used to quantitatively explore the effectiveness of each factor on equivalent coefficient of friction in this section.

4.5.1 Development of statistical model

Based on the linear assumption, equivalent coefficient of friction was supposed to be linearly correlated with influential factors and obey the model shown in **Table 4.1**. Multiple linear regression was implemented and backward elimination approach was applied to obtain optimization model in the aid of F-test and t-test. The regression procedures and results were listed in **Table 4.1**.

Table 4.1 Multivariable analysis of landslide mobility by backward elimination approach

$\mu = H_{\max}/L_{\max} = m_1 \log h + m_2 RT + m_3 \sin \varepsilon + m_4 \log V + m_5 \tan \theta + m_6 \log PHA$											
Variable and parameter		m_1	m_2	m_3	m_4	m_5	m_6	Multiple R	Adjusted R ²	F-stat (F _{0.05})	t-test (t _{0.05})
6 variables	m_i	0.505	-0.073	-0.412	-0.086	0.124	-0.015				
	t-stat	4.248	-3.259	-2.851	-2.086	1.237	-0.098	0.972	0.914	115.774 (2.342)	2.023
	m'_i	0.513	-0.412	-0.414	-0.335	0.171	-0.012				
5 variables	m_i	0.504	-0.073	-0.415	-0.087	0.122					
	t-stat	4.307	-3.309	-2.998	-2.244	1.252		0.972	0.916	142.365 (2.449)	2.021
	m'_i	0.512	-0.413	-0.418	-0.340	0.169					
4 variables	m_i	0.564	-0.077	-0.376	-0.096						
	t-stat	5.247	-3.512	-2.768	-2.477			0.971	0.916	175.196 (2.600)	2.020
	m'_i	0.573	-0.436	-0.378	-0.372						

In **Table 4.1**, $\mu = H_{\max}/L_{\max}$ refers to equivalent coefficient of friction. h represents slope height (m). RT refers to rock type, it was qualitatively considered and 4, 3, 2, and 1 were respectively assigned to RT1, RT2, RT3 and RT4. ε represents slope transition angle ($^{\circ}$). V represents landslide source volume (m^3). θ denotes slope angle ($^{\circ}$). PHA refers to horizontal peak ground acceleration (m/s^2), estimated by Eq. (3.1). The basis of logarithm is 10. Multiple R means multiple correlation coefficient, which represents the correlated level between dependent variable and independent variables. Adjusted R² represents adjusted coefficient of multiple determination, namely, adjusted squared multiple correlation, which reveals the goodness of fit, ranging from 0

for no correlation to 1 for a perfect correlation. F-stat denotes regressive F-value, $F_{0.05}$ denotes F-test threshold value with 95% significance level, if F-stat is bigger than $F_{0.05}$, it suggests overall regression of the model satisfies statistical significance level. t-stat denotes regressive t-value of each regression coefficient, $t_{0.05}$ denotes t-test threshold value with 95% significance level, if t-stat is larger than $t_{0.05}$, it suggests corresponding regression coefficient, m_i , satisfies statistical significance level. However, not all regression coefficients are significant during regression procedures, therefore, the variable with smallest absolute t-stat value (bold digit in the **Table 4.1**) was eliminated and then re-regressed, step by step until overall regression of the model (F-test) and all regressive coefficients (t-test) both satisfy significance levels. These procedures are named as backward elimination regression. Because the units of independent variables affect regression coefficient, m_i , therefore, standardized regression coefficient, m'_i , was applied to exclude the effect of unit dimension, so as to have insight into the effectiveness of each independent variable on dependent variable.

Compared three models in **Table 4.1**, F-tests suggest that all of these hypothetical models have statistical significance and satisfy linear assumption. Based on those absolute values of standardized regression coefficients in the 4 variables' model and backward elimination procedures, they both suggest that slope height, rock type, slope transition angle and landslide volume had predominant effect on equivalent coefficient of friction, slope angle and seismic acceleration had relatively weaker influence. Furthermore, the model with 4 variables satisfied not only overall statistical significance but also the significance of each regression coefficient. Hence, the empirical optimization model for the estimation of equivalent coefficient of friction is as follows:

$$\mu = H_{\max} / L_{\max} = 0.564 \log h - 0.077RT - 0.376 \sin \varepsilon - 0.096 \log V \quad (4.1)$$

The predicted equivalent coefficient of friction by Eq. (4.1) and observed values were compared in **Figure 4.14**, which suggests this statistical model is effective for most of landslides in this dataset. Therefore, this model might be useful to predict landslide mobility in Wenchuan earthquake affected area and similar geological and geomorphological areas.

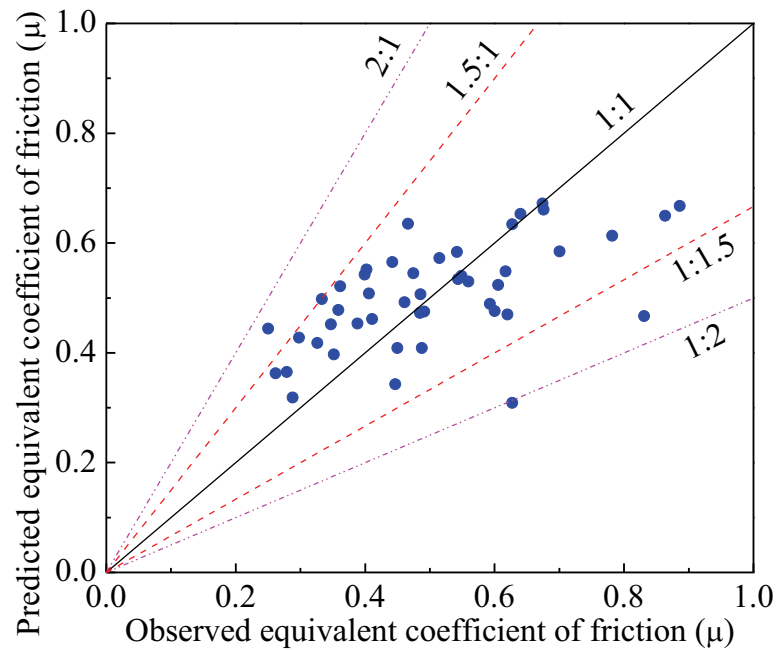


Figure 4.14 Predicted versus observed equivalent coefficient of friction

4.5.2 Comparison with previous models

There are many previous studies on landslide mobility, and several prediction models were worldwide established. They were summarized in **Table 4.2**. Making use of these four previous models to estimate equivalent coefficient of friction of these 46 landslides triggered by Wenchuan earthquake, the results were shown in **Figure 4.15**, which suggests that the model proposed by Corominas (1996) and Hunter and Fell (2003) yielded lower agreement with observed values, the average estimation errors of these two models are 43.73% and 45.97%, respectively. The reason was inferred that Corominas model was developed from a dataset including 35% debris flows, which appears a special mobile mechanism due to relatively higher water content of failed mass. Debris flow is very different from other types of landslide, such as, rotational landslide, translational landslide, block slide, and it generally had higher mobility (larger $1/\mu$), therefore, the predicted equivalent coefficients of friction by Corominas model were generally smaller than the observed. For the relatively lower reliability of Hunter and Fell (2003) model, it might be attributable to the amount limitation of data source, which 11 landslides were used to obtain empirical model. Compared proposed mode, Eq. (4.1), with the models of Scheidegger (1973) and Legros (2000), the results suggest that the average estimation error of Eq.

(4.1) is 10% lower than these two models. In general, the validity of Eq. (4.1) is much higher than that of previous models.

Table 4.2 Landslide mobility prediction models and their comparisons

Prediction models	Data source	Authors	Average error
$\mu=0.564\log h -0.077RT -0.376\sin\epsilon -0.096\log V$	46 landslides	This section	21.16%
$\log\mu= -0.157\log V+0.624$	33 landslides	Scheidegger, 1973	31.11%
$\mu=0.16V^{-0.15}$	32 landslides	Legros, 2000	31.22%
$\log\mu= -0.085\log V -0.047$	204 landslides (including 71 debris flows)	Corominas, 1996	43.73%
$\mu=0.69\tan\theta + 0.086$	11 landslides	Hunter and Fell, 2003	45.97%

*Hint: V in unit of m^3 except the model of Legros(2000), which V is in unit of km^3

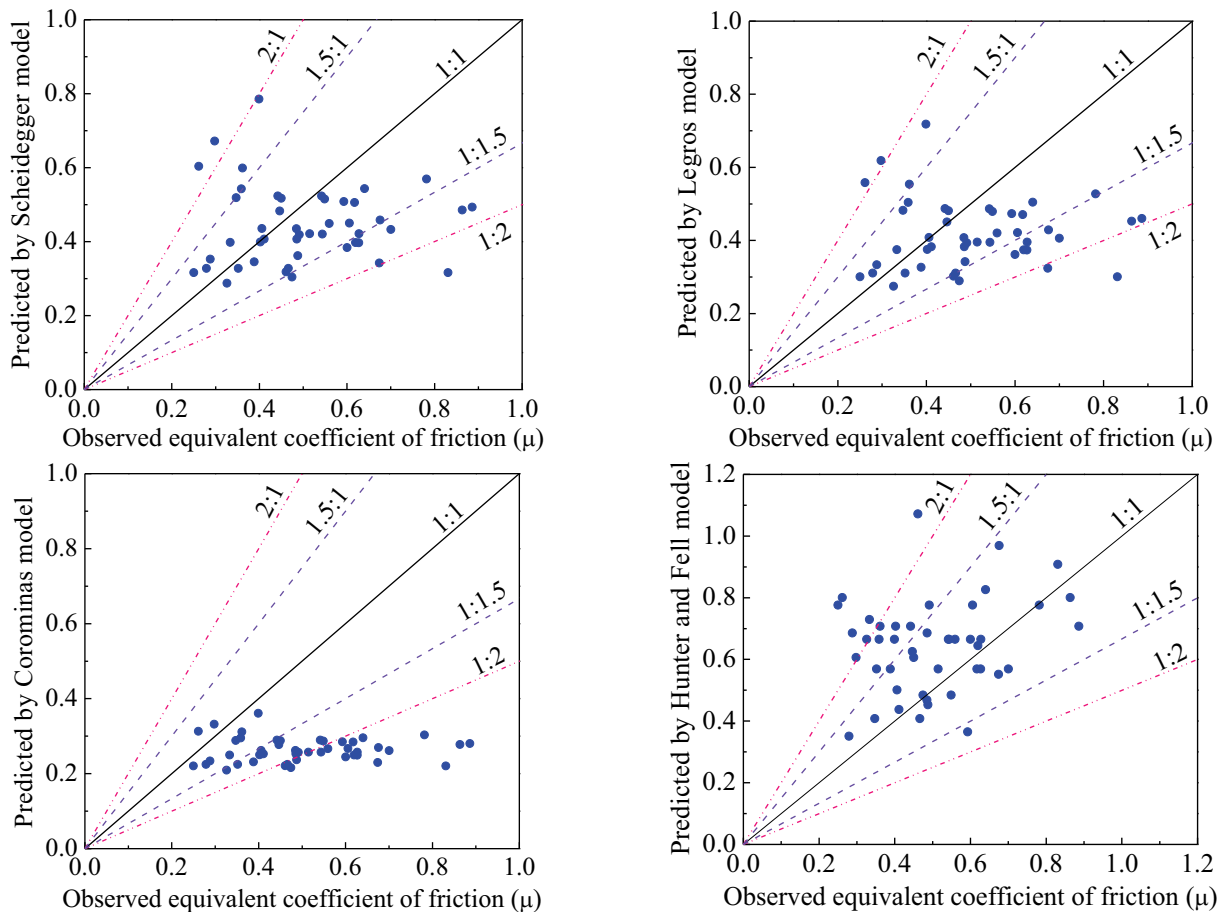


Figure 4.15 Predicted equivalent coefficient of friction by previous models versus the observed

4.6 Statistical model of landslide travel distance

4.6.1 Development of statistical model

In section 4.5, equivalent coefficient of friction was discussed, although it is useful to estimate the mobile ability of failed mass, however, it is not convenient to directly predict landslide travel distance, moreover, small landslide displayed a variable landslide mobility which can be as low as large landslide (Corominas, 1996); Hunter and Fell (2003) reanalyzed the data from Corominas (1996) and obtained two empirical equations of equivalent coefficient of friction for small and large unconfined landslides, as shown in **Figure 4.16**. Therefore, it is necessary to develop a new model for landslide travel distance prediction, so as to assess the potentially endangered travel path.

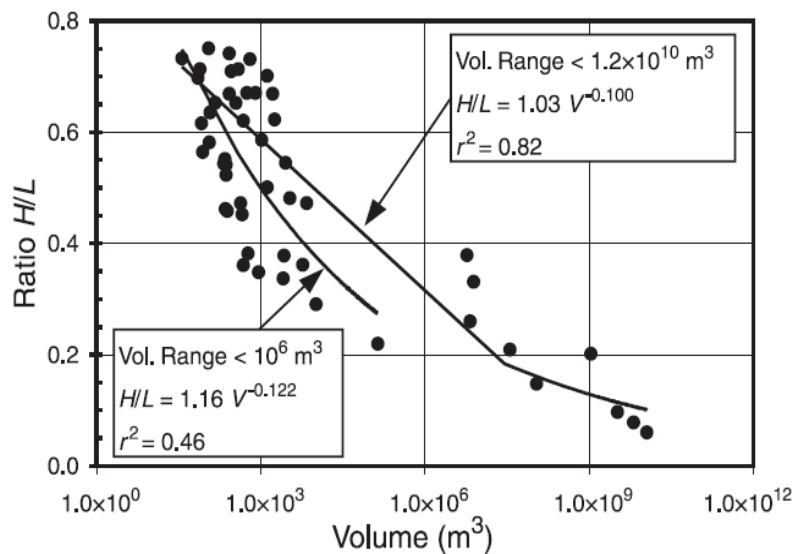


Figure 4.16 Landslide mobility of unconfined debris flows (Hunter and Fell, 2003).

Under the linear assumption, multiple linear regression and backward elimination approach were applied again to obtain optimization model of landslide travel distance and explore the effectiveness of influential factors on landslide travel distance with the help of F-tests and t-tests. The regression procedures and results were listed in **Table 4.3**.

Table 4.3 Multivariable analysis of landslide travel distance by backward elimination approach
$$\log L_{\max} = n_1 RT + n_2 \log V + n_3 \sin \varepsilon + n_4 \log h + n_5 \log PHA + n_6 \tan \theta + n_0$$

Variable and parameter	n_1	n_2	n_3	n_4	n_5	n_6	n_0	Multiple R	F-stat	$F_{0.05}$	t-test ($t_{0.05}$)
n_i	0.139	0.189	0.618	-0.182	-0.133	0.049	1.795				
6 variables t-stat	4.439	3.280	2.749	-0.737	-0.555	0.351	3.544	0.719	6.973	2.342	2.023
n'_i	0.507	0.475	0.403	-0.120	-0.070	0.044	-				
n_i	0.137	0.185	0.633	-0.165	-0.125	-	1.811				
5 variables t-stat	4.491	3.312	2.911	-0.689	-0.530	-	3.630	0.718	8.530	2.449	2.021
n'_i	0.501	0.465	0.413	-0.109	-0.066	-	-				
n_i	0.137	0.176	0.584	-0.129	-	-	1.686				
4 variables t-stat	4.534	3.324	2.994	-0.568	-	-	3.867	0.716	10.781	2.600	2.020
n'_i	0.501	0.444	0.381	-0.085	-	-	-				
n_i	0.136	0.159	0.529	-	-	-	1.497				
3 variables t-stat	4.539	3.692	3.150	-	-	-	5.345	0.713	14.501	2.827	2.018
n'_i	0.496	0.401	0.345	-	-	-	-				

Compared four models in **Table 4.3**, F-tests suggest that all of these hypothetical models have statistical significance and satisfy linear assumption. Based on those absolute values of standardized regression coefficients in the 6 variables' model and the backward elimination procedures, they both suggest that rock type, landslide volume and slope transition angle were more influential than slope height, seismic acceleration and slope angle on landslide travel distance. Furthermore, the model with 3 variables satisfied not only overall statistical significance but also the significance of each regression coefficient, hence, the optimization empirical model for landslide travel distance prediction is as follows:

$$\log L_{\max} = 0.136RT + 0.159 \log V + 0.529 \sin \varepsilon + 1.497 \quad (R^2 = 0.51) \quad (4.2)$$

where L_{\max} is the landslide horizontal travel distance (m); V represents landslide source volume (m^3); RT represents rock type, qualitatively considered as 4, 3, 2, 1 for RT1, RT2, RT3, RT4, respectively; ε is slope transition angle ($^\circ$); log is logarithm with 10 basis.

By using Eq.(4.2) to predict the travel distance of surveyed 46 landslides, the comparison between predictions and observations was shown in **Figure 4.17**, this self-verification suggests that proposed statistical model for travel distance prediction is valid for most landslides in this dataset. The average estimation error of these 46 landslides, $|L_{predicted} - L_{observed}| / L_{observed} \times 100\%$, is 32.95%. In order to further verify the applicability of proposed empirical model, 8 landslides in Wenchuan earthquake area were used to check the validity of Eq.(4.2), the parameters of each landslides and the predictive results were listed in **Table 4.4**, and the corresponding 8 landslides were compared their observed and predicted travel distances in **Figure 4.17**, which further suggest that the proposed model is valid. Therefore, it might be useful to preliminarily assess the travel distance of potential landslide in Wenchuan earthquake area and other similar geological and geomorphological regions.

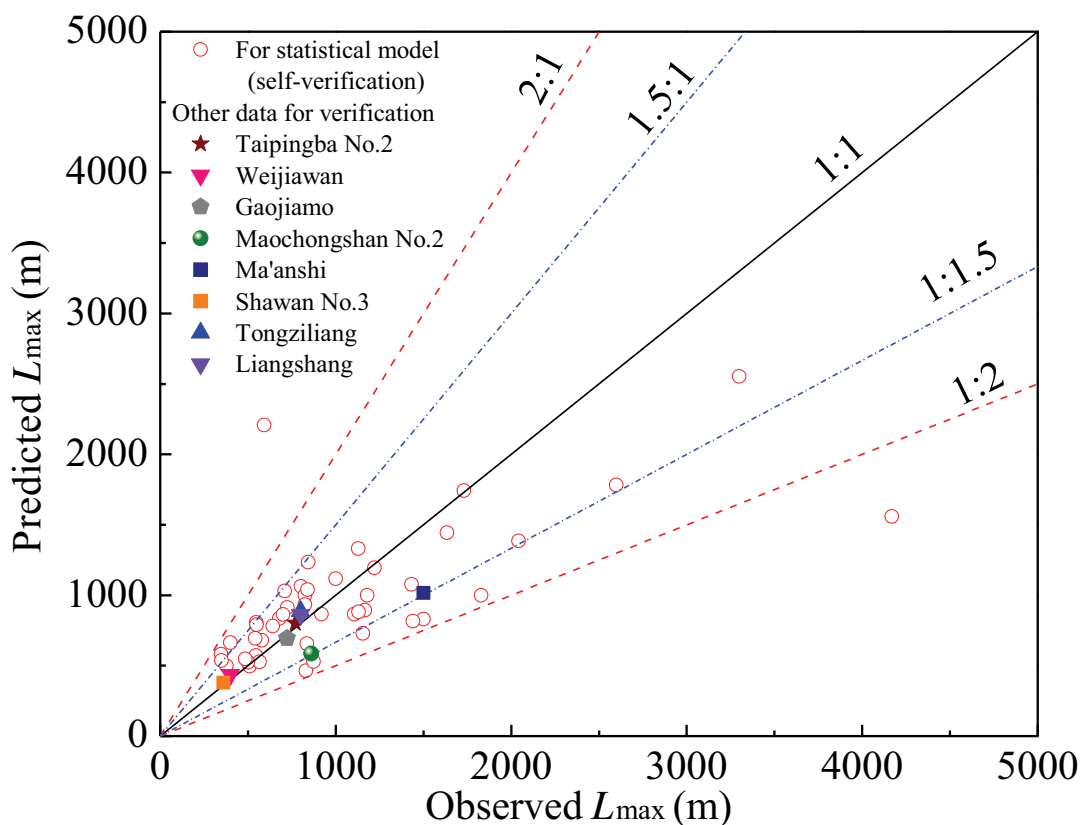


Figure 4.17 Predicted versus observed horizontal travel distance

Table 4.4 The validation of proposed statistical model for landslide travel distance by case studies

Landslide	Slope transition angle, $\varepsilon(^{\circ})$	Sliding volume, V (10^4m^3)	Main lithology	Rock type, RT	H_{\max} (m)	Observed L_{\max} (m)	Predicted L_{\max} (m)	Estimation error (%)	Reference
Taipingba No.2	150	30	weakly weathered phyllite	RT3 ($RT=2$)	540	770	802.35	4.20%	Gou, 2012
Weijiawan	172	10	weakly weathered phyllite and limestone	RT3 ($RT=2$)	200	400	434.13	8.53%	Gou, 2012
Gaojiamo	168	113	weakly weathered phyllite and limestone	RT3 ($RT=2$)	340	722	694.10	3.86%	Gou, 2012
Maochongshan No.2	171	58	weakly weathered metasandstone	RT3 ($RT=2$)	534	860	586.33	31.82%	Gou, 2012
Ma'anshi	151	148	weakly weathered phyllite	RT3 ($RT=2$)	464	1500	1015.16	32.32%	Gou, 2012
Shawan No.3	172	30	moderately~strongly weathered metasandstone	RT4 ($RT=1$)	240	360	377.99	5.00%	Gou, 2012
Tongziliang	146	256	moderately~strongly weathered metasandstone	RT4 ($RT=1$)	110	800	886.59	10.82%	Gou, 2012
Liangshang	155	600	weakly weathered shale and moderately weathered limestone	RT4 ($RT=1$)	620	800	859.59	7.45%	Gou, 2012

4.6.2 Comparison with previous models

Table 4.5 Landslide travel distance prediction models and their comparisons

Prediction model	Data source	Authors	Average error for 54 surveyed landslides
$\log L_{\max} = 0.136RT + 0.159 \log V + 0.529 \sin \epsilon + 1.497$	46 landslides	This section	29.99%
$L_{\max} = 1.9V^{0.16}H_{\max}^{0.83}$	160 debris flows	Rickenmann, 1999	116.77%
$L_{\max} = 8V^{0.25}$	32 landslides	Legros, 2000	248.26%

*Hint: V and L_{\max} in unit of m^3 and m, respectively, except the model of Legros(2000), which V and L_{\max} is in km^3 and km

In order to directly assess landslide travel distance, Rickenmann (1999) and Legros (2000) developed empirical models for this issue, and being listed in **Table 4.5**. Making use of these two previous models to estimate the travel distance of these 54 landslides in Wenchuan earthquake area, the results were shown in **Figure 4.18** and **Figure 4.19**, which suggests that the model proposed by Rickenmann (1999) and Legros (2000) cannot obtain satisfactory assessment, the average estimation errors of these two models are 116.77% and 248.26%, respectively, which means that these two previous models are not suitable to be applied in Wenchuan earthquake area. The reasons were inferred that Rickenmann's model was developed from debris flows, however, dataset in this paper is mainly included rock (soil) slide and debris (rock) avalanche, therefore, it may draw a conclusion that the mechanism of debris flow is very different from rock (soil) slide and debris (rock) avalanche, and results in the failed application of Rickemann model in Wenchuan earthquake area; on the other hand, most of predictions by Rickemann model are significantly bigger than the observations (above the dash line with 2:1 gradient in **Figure 4.18**), and there is no prediction smaller than observation, it means that under the same conditions (volume, rock type, slope transition angle, etc.), debris flow usually will travel longer than rock (soil) slide and debris (rock) avalanche. The reason was inferred that the lubrication of water content in the failed mass of debris flow increased travel distance. This comparison reconfirmed and implied that landslide travel distance was heavily affected by mobile mechanism of sliding mass, especially, failed mass with relatively abundant water content, it would cause the mobilization of debris flow was quite different from other types of landslides. For the Legros's model, the comparison between prediction and observation of landslide travel distance was

shown in **Figure 4.19**, its invalidity in Wenchuan earthquake area might be due to the difference of geomorphological and hydro-geological conditions.

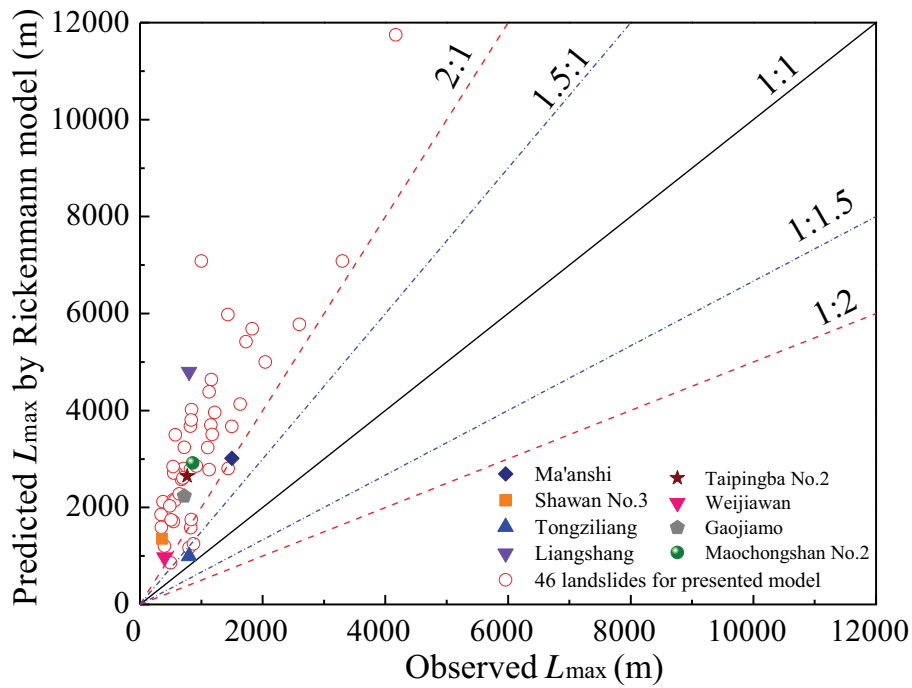


Figure 4.18 Predicted landslide travel distance by Rickenmann's model versus the observed

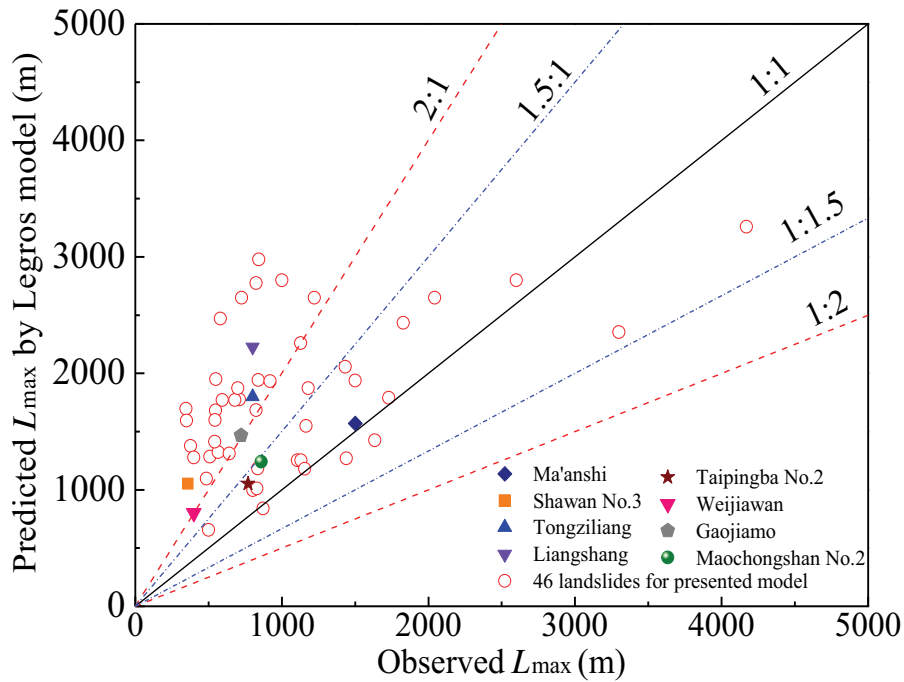


Figure 4.19 Predicted landslide travel distance by Legros's model versus the observed

4.7 Discussions

The disaster caused by high mobility landslide was severe, such as Donghekou landslide travelled about 2.6km and buried four villages and more than 780 lives (Qi et al., 2011), while landslide mobility was affected by numerous factors, such as topographical factors, the degree of path confinement, geomechanical properties of rock (soil), mobile mechanism, and so on. Therefore, how to estimate landslide mobility is a very complicate issue. Corominas (1996) pointed out that travel distance (L_{\max}) was not an appropriate indicator of landslide mobility, because high fall generally results in long horizontal reaches, but longer horizontal distance does not necessarily correspond to lower travel distance angle (smaller μ , higher mobility), meanwhile, the statistical result illustrated in **Figure 4.6** suggests that H_{\max} had significant linear correlation with L_{\max} . Hence, this chapter used the ratio of H_{\max} to L_{\max} as an index of landslide mobility, which was termed by Shreve (1968) and Scheidegger (1973) as equivalent coefficient of friction. The reasons why the maximum horizontal travel distance was used, instead of the travel distance of gravity center, are as follows: firstly, maximum horizontal travel distance (L_{\max}) is more applicable to estimate the farthest reach and forecast the potentially endangered area; secondly, how to estimate the gravity center of pre-failure and post-failure is so difficult that it is high probability to result in deviation and affect the reliability of prediction model.

As many influential factors as possible to be collected, 46 landslides with 9 parameters were used to qualitatively and quantitatively analyse. However, the general tendencies of each influential factor related with equivalent coefficient of friction are more or less scattering, as shown in **Figure 4.7–4.8, 4.10–13**, which might be caused by the discretization of data. Because our data excluded not only landslides obstructed by river, valley and relatively large infrastructure but also travel path confined by lateral steep slope and landslides with large deflection travel path, besides, some data were from field investigation, remote sensing interpretation and some data were from the detail descriptions of published papers and books. During the investigation, it was difficult to judge the confinement degree, the boundary between partly confined and confined was not only relied on the experience of investigator but also affected by the relative magnitude between landslide volume and obstacles or topographical changes, hence, the estimation error of several predictions was too large to be accepted; moreover, travel distance of 46 landslides used to develop statistical model is 91.3% (42 out of 46) shorter

than 2000m, it may cause the predicted results of landslides with over 2000m observed travel distance are more scattering than others in **Figure 4.17**. Although, it is difficult to give a clear definition between partly confined and confined, and there are some inevitable statistical errors, the stepwise regression method, shown in **Table 4.1** and **Table 4.3**, gave a reasonable approach to obtain empirical prediction models for equivalent coefficient of friction and landslide travel distance, respectively, their validities were further verified by comparison between predictions and observations, as shown in **Figure 4.14** and **Figure 4.17**, which suggest the two statistical models mainly yielded satisfactory agreements between observations and predictions. Moreover, the comparisons between presented models and previous models suggested that this chapter proposed models were more suitable in Wenchuan earthquake area; they might be useful in the region with similar conditions as Longmenshan mountainous area.

However, note that, the data of sliding source volume used here was between 4.5×10^4 and $2.75 \times 10^7 \text{m}^3$, and horizontal travel distance was between 347 and 4170m; besides, the effects of ground water, geological structures and landslide type on landslide movement were not discussed. Previous studies have been found that pore-water pressure caused shear strength significant reduction (Takarada et al., 1999; Major and Iverson, 1999; Wang and Sassa, 2003; Sassa et al., 2004, 2005), and then resulting in failed mass might perform different mobile motions during sliding. The reason why the effect of ground water on landslide travel distance did not analyze is that there were rainfalls after earthquake, so the ground water condition of landslide occurrence had changed during investigation. The effect of geological structure on slope failure mode was demonstrated by Aydan et al. (2006, 2009), and Corominas (1996) proposed that different landslide types appeared different mobile abilities based on empirical relations of different landslide types. Therefore, discussion on landslide mobility and its travel distance should consider the influences of geological structures and landslide type. However, in this chapter, our data are limited to 46 landslides and the types of slope failure mainly included rock (or soil) slide, rock avalanche and debris avalanche, if these data were further classified into several groups, the regression model of each type of landslide would be uncertainty. Hence, a more generalized model was derived to estimated landslide mobility and its travel distance. In spite of ignoring the influences of ground water, geological structures and landslide type on landslide movement in proposed models, most of the predicted results are reasonable, compared with observations and estimations by previous models. Notwithstanding, the applicability of proposed models needs to

be further verified and more influential factors on landslide mobility and its travel distance were recommended to take into consideration during improvement.

4.8 Summary

In this chapter, 46 landslides with relatively long runout were used to discuss landslide mobility and travel distance related with numerous influential factors, such as slope angle(θ), slope transition angle(ε), slope height(h), rock type (RT), landslide source volume(V), horizontal peak ground acceleration ($PH A$). Based on the qualitative and quantitative analysis, several findings are as follows :

- (1) Landslide travel distance (L_{max}) had relatively strongly linear correlation with landslide height(H_{max}) .
- (2) Multivariable analysis revealed that slope height, rock type, slope transition angle and landslide volume were the most important influential factors on landslide mobility, and followed by slope angle; seismic acceleration had weakest effect on landslide mobility.
- (3) Rock type, landslide volume and slope transition angle were more influential than slope height, seismic acceleration and slope angle on landslide travel distance.
- (4) Two empirical models, as Eq.(4.1) and (4.2), were proposed to predict equivalent coefficient of friction and travel distance in similar geological conditions as Wenchuan earthquake affected area.

References

- Aydan, ö., Hamada, M., 2006. Damage to civil engineering structures by Oct.8,2005 Kashmir earthquake and recommendations for recovery and reconstruction, Journal of Disaster Research,1(3), 1-9.
- Aydan, ö., Ohta, Y., Hamada, M., et al., 2009. The characteristics of the 2008 Wenchuan earthquake disaster with a special emphasis on rock slope failure, quake lakes and damage to tunnels. Journal of The School of Marine Science and Technology , Tokai University, 7(2), 1-23.

- Corominas, J., 1996. The angle of reach as a mobility index for small and larger landslides. *Canadian Geotechnical Journal*, 33, 260–271.
- Chigira, M., Wu, X.Y., Inokuchi, T., Wang, G. H., 2010. Landslides induced by the 2008 Wenchuan earthquake, Sichuan, China. *Geomorphology*, 118, 225–238.
- Dai, F.C., Xu, Q., Yao, X., Xu, L., Tu, X.B., Gong, Q.M., 2011. Spatial distribution of landslides triggered by the 2008 Ms8.0 Wenchuan earthquake, China. *Journal of Asian Earth Sciences*, 40, 833–895.
- Fan, X.Y., Qiao, J.P., 2010. Influence of landslide and ground factors on large-scale landslide movement. *Chinese Journal of Rock Mechanics and Engineering*, 29(11), 2337–2347. (In Chinese with English abstract).
- Gorum, T., Fan, X.M., Westen, C.J., Huang, R.Q. Xu, Q., 2011. Distribution pattern of earthquake-induced landslides triggered by the 12 May 2008 Wenchuan earthquake, *Geomorphology*, 133, 152–167.
- Gou, F.G., 2012. Regularity and risk analysis of landslides induced by Wenchuan earthquake—Using a case of Pingtong-Naban segment, Chengdu University of Technology. (Master thesis, In Chinese with English abstract)
- Heim, A., 1932. *Bergsturz und Menschenleben*. Fretz und Wasmuth, Zurich, p.218.
- Hsü, K.J., 1975. Catastrophic debris streams (sturzstroms) generated by rock falls. *Geological Society of America Bulletin*, 86, 129–140.
- Hayashi, J.N. and Self, S., 1992. A comparison of pyroclastic flow and landslide mobility. *Journal of Geophysical research*, 97, 9063–9071.
- Hunter, G., Fell, R., 2003. Travel distance angle for “rapid” landslides in constructed and natural soil slopes. *Canadian Geotechnical Journal*, 40, 1123–1141.
- Huang, R.Q., Li, W.L., 2008. Research on development and distribution rules of geohazards induced by Wenchuan earthquake on 12th May, 2008. *Chinese Journal of Rock Mechanics and Engineering*, 27(12), 2585–2592. (In Chinese with English abstract)
- Huang, R.Q., Li, W.L., 2009a. Analysis on the number and density of landslides triggered by the 2008 Wenchuan earthquake, China. *Journal of Geological Hazards and Environment Preservation*, 20(3), 1–7. (In Chinese with English abstract)

- Huang, R.Q., Li, W.L., 2009b. Analysis of the geo-hazards triggered by the 12 May 2008 Wenchuan earthquake, China. *Bulletin of Engineering Geology and the Environment*, 68, 363–371.
- Hattanji, T., Moriwaki, H., 2009. Morphometric analysis of relic landslides using detailed landslide distribution maps: Implications for forecasting travel distance of future landslides. *Geomorphology*, 103,447–454.
- Hattanji, T., Moriwaki, H., 2011. Topographic features and mobility of old landslides in Tanzawa and Hakone areas—Focusing on equivalent coefficient of dynamic friction and areal expansion of landslide mass, *Journal of Japan Landslide society*, 48(1), 45– 51. (In Japanese with English abstract)
- Kokusho, T., Ishizawa, T., Nishida, K., 2009. Travel distance of failed slopes during 2004 Chuetsu earthquake and its evaluation in terms of energy. *Soil Dynamics and Earthquake Engineering*, 29, 1159–1169.
- Lergros, F., 2002. The mobility of long-runout landslides. *Engineering Geology*,63, 301-331.
- Li, X.Z., Kong, J.M., Deng, H.Y., et al., 2009. Analysis on characteristics and deformation failure mode of large-scale landslides induced by “5·12” Wenchuan earthquake. *Journal of Sichuan University (Engineering Science Edition)*, 41(3), 72–77. (In Chinese with English abstract).
- Li, X.Z., Kong, J.M., 2010. Runout distance estimation of landslides triggered by “5·12” Wenchuan earthquake. *Journal of Sichuan University (Engineering Science Edition)*, 42(5), 243–249. (In Chinese with English abstract).
- Li, X.Z., Kong, J.M., Cui, Y., Tian, S.J., 2010. Statistical relations between landslides induced by Wenchuan earthquake and earthquake parameters, geological as well as geomorphological factors. *Journal of Engineering Geology*, 18(1), 8–14. (In Chinese with English abstract).
- Major, J.J., Iverson, R.M., 1999. Debris-flow deposition: effects of pore-fluid pressure and friction concentrated at flow margins. *Geological Society of America Bulletin*, 111, 1424–1434.
- Okura,Y., Kitahara, H., Kawanami, A, Kurokawa, U., 2003. Topography and volume effects on travel distance of surface failre. *Engineering Geology*, 67, 243–254.

- Qi, S.W., Xu, Q., Lan, H.X., et al., 2010. Spatial distribution analysis of landslides triggered by 2008.5.12 Wenchuan earthquake, China, *Engineering Geology*, 116, 95–108.
- Qi, S.W., Xu, Q., Zhang, B., et al., 2011. Source characteristics of long runout rock avalanches triggered by the 2008 Wenchuan earthquake, China. *Journal of Asian Earth Sciences*, 40, 896–906.
- Rickenmann, D., 1999. Empirical relationships for debris flows. *Natural Hazards*, 19, 47–77.
- Shreve, R.L., 1968. The Blackhawk landslide. Geological Society of America, Special paper 108, 1–47.
- Scheidegger, A.E., 1973. On the prediction of the reach and velocity of catastrophic landslides. *Rock Mechanics*. 5, 231–236.
- Shaller, P.J., 1991. Analysis and implications of large martian and terrestrial landslides, Doctor thesis, California institute of Technology.
- Takarada, S., Ui, T., Yamamoto, Y., 1999. Depositional features and transportation mechanism of valley-filling Iwasegawa and Kaida debris avalanches, Japan. *Bulletin of volcanology*. 60, 508–522.
- Sassa, K., Wang, G.H., Fukuoka, H., et al., 2004. Landslide risk evaluation and hazard zoning for rapid and long-travel landslides in urban development areas. *Landslides*, 1, 221–235.
- Sassa, K., Fukuoka, H., Wang, F., Wang, G.H., 2005. Dynamic properties of earthquake-induced large-scale rapid landslides within past landslide masses, *Landslides*, 2, 125–134.
- Tang, C., Zhu, J., Chang, M., et al., 2012. An empirical-statistical model for predicting debris flow runout zones in the Wenchuan earthquake area. *Quaternary International*, 250, 63–73.
- Wang, G.H., Sassa, K., 2003. Pore-pressure generation and movement of rainfall-induced landslides: effects of grain size and fine-particle content. *Engineering Geology*, 69, 109–125.
- Xie, H.P., Deng, J.H., Tai, J.J., et al., 2008. Wenchuan large earthquake and post-earthquake reconstruction-related geotechnical problems. *Chinese Journal of Rock Mechanics and Engineering*, 27(9), 1781–1791. (In Chinese with English abstract)
- Xu, Q., Pei, X.J., Huang, R.Q. et al., 2009a. Larger-scale landslides induced by the Wenchuan earthquake. Science press, Beijing. (In Chinese)

- Xu, C., Dai, F.C., Yao, X., et al., 2009b. GIS-based landslide susceptibility assessment using analytical hierarchy process in Wenchuan earthquake region. *Chinese Journal of Rock Mechanics and Engineering*, 28, Supp.2, 1–8. (In Chinese with English abstract)
- Xu, C., Dai, F.C., Yao, X., et al., 2010. GIS based certainty factor analysis of landslide triggering factors in Wenchuan earthquake. *Chinese Journal of Rock Mechanics and Engineering*, 29:Supp.1, 2972–2981. (In Chinese with English abstract)
- Xu, C., Xu, X.W., 2012. Comment on “Spatial distribution analysis of landslides triggered by 2008.5.12 Wenchuan earthquake, China” by Shengwen Qi, Qiang Xu, Hengxiang Lan, Bing Zhang, Jianyou Liu [*Engineering Geology* 116(2010) 95–108], *Engineering Geology*, 133–134, 40–42.
- Xu, C., Xu, X.W., Wu, X.Y., et al., 2013a. Detailed catalog of landslides triggered by the 2008 Wenchuan earthquake and statistical analyses of their spatial distribution. *Journal of Engineering Geology*, 21(1), 25–44. (In Chinese with English abstract)
- Xu, C., Xu, X.W., Yao, X., Dai, F.C., 2013b. Three (nearly) complete inventories of landslides triggered by the May 12, 2008 Wenchuan Mw 7.9 earthquake of China and their spatial distribution statistical analysis, *Landslides*, open access.
- Yin, Y.P., Wang, F.W., Sun, P., 2009. Landslide hazards triggered by the 2008 Wenchuan earthquake, Sichuan, China. *Landslides*, 6, 139–151.

Chapter 5 Seismic Performance of Reinforced Slope

5.1 Introduction

In chapter 3 and chapter 4, slope stability and landslide mobility were respectively discussed. In order to learn from seismic damage and take effective countermeasures to enforce slope stability, this chapter would report the field survey about seismic damage of four slope reinforcements, that is, anchor cable, frame beam, soil nailing wall and shotcrete with bolts. The investigation was conducted along National Road 213 and Dujiangyan–Wenchuan expressway, the route of field investigation was illustrated in **Figure 5.1**.

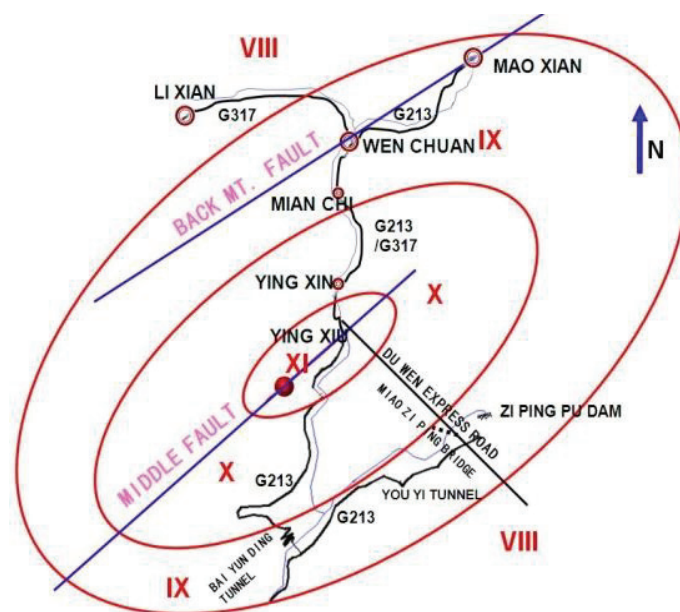


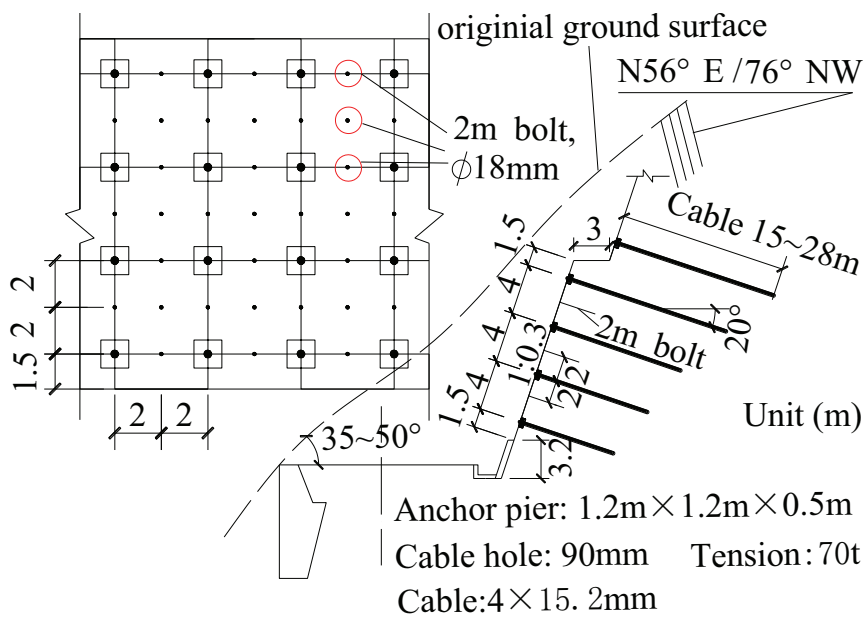
Figure 5.1 The sketch of investigated route

5.2 Anti-seismic behaviors of different slope reinforcements



(a) visible crack nearby anchor head

(b) Anchor head was pulled out



(c) Reinforcement parameters of anchor cable

Figure 5.2 Performance of anchor cable reinforced slopes and reinforcement parameters

Slopes reinforced by anchor cable were located along the left bank road of Zipingpu dam, slope gradient was cut to 1:0.3, and their cables were 15–28m length with 4m spacing. **Figure 5.2(a)** and **(b)** are two typical slopes reinforced by anchor cable. These slopes were designed to have the capability to sustain VII scale of Chinese seismic intensity (CSIS, GB/T17742-1999),

that is, fortification seismic intensity is VII scale (VII Chinese seismic intensity coincides with 0.1 seismic coefficient). However, the actually experienced seismic intensity was VIII scale and estimated horizontal PGA was about 0.35g. Although experienced acceleration exceeded the design level, slopes were wholly stable except several visible cracks nearby anchor heads and except that several anchor heads were pulled out and (or) destroyed by collapsed rock from upper non-reinforced parts.

The investigation result suggests anchor cable has good anti-seismic property. This is consistent with the analytical result about dynamic responses of anchor cable reinforced slopes during Kobe earthquake, which revealed anchor cable effectively constrained slope deformation and reduced shear stress at the slope toe (Yamamoto and Toriihara, 2003), as a result of anchor cable had significant ability to restrain the acceleration amplification effect from slope base toward slope upside (Masuda, et al., 1996, 1997); Besides, it might be attributed to cables were long enough to penetrate the potential sliding surface, as so to enhance slope stability. Therefore, slopes reinforced by anchor cable performed good anti-seismic behavior during Wenchuan earthquake.

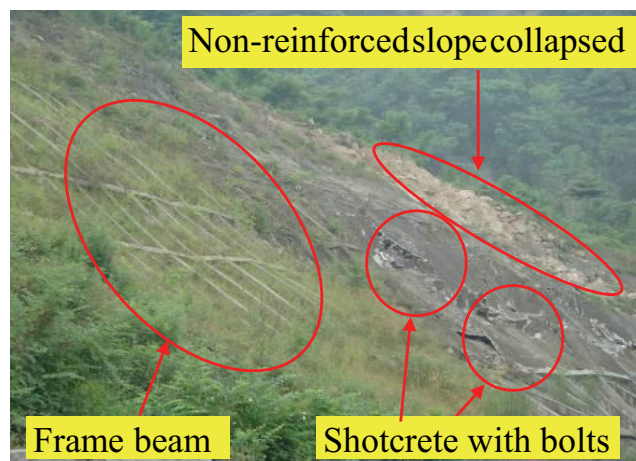
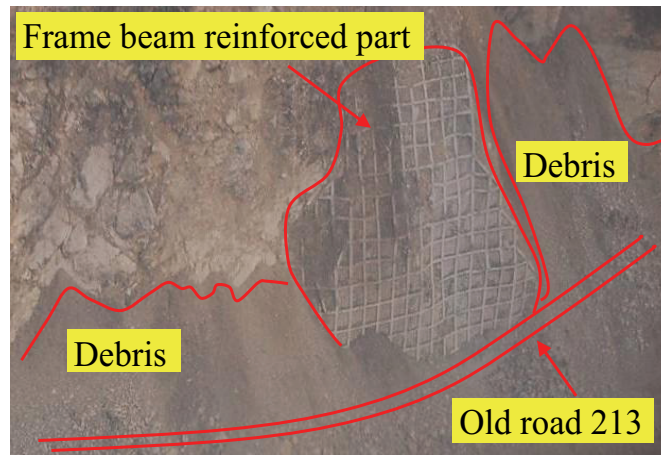


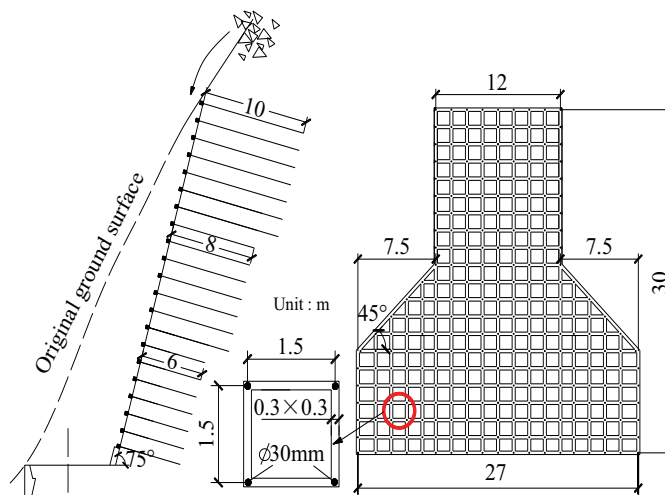
Figure 5.3 Comparison between reinforced slope and non-reinforced slope (Zhou, et al., 2010)

Slope shown in **Figure 5.3** was located at national road 213, about 50km from the epicenter (Zhou, et al., 2010). Its estimated horizontal peak ground acceleration was about 0.4g. One part reinforced by frame beam was wholly stable except visible cracks at the beam joints, other part reinforced by shotcrete with bolts was stable except that its steel mesh and shotcrete layer were

compressed to uplift due to shotcrete layer down-slip. However, adjacent non-reinforced slope collapsed. This comparison suggests frame beam had good anti-seismic property, but shotcrete with bolts had limited ability to enhance slope stability.



(a) comparison between frame beam reinforced slope and non-reinforced slope



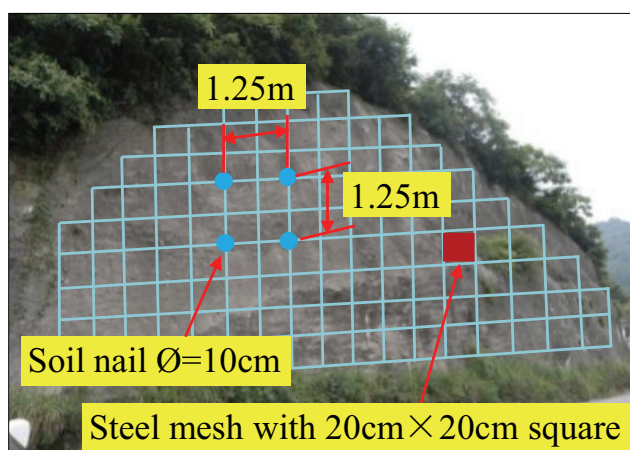
(b) Reinforcement parameters of frame beam

Figure 5.4 Performance of frame beam reinforced slope and reinforcement parameters

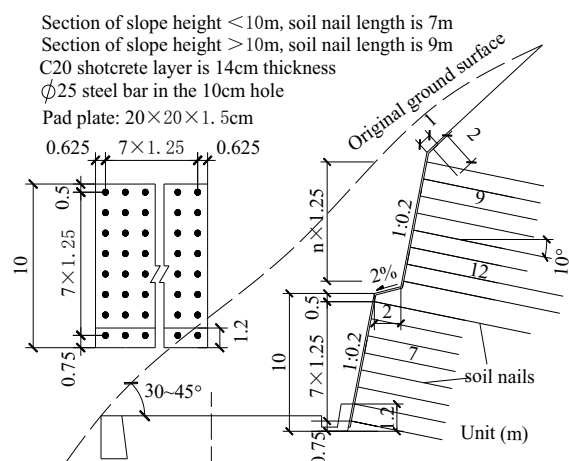
Another case to demonstrate frame beam had good anti-seismic property was illustrated in **Figure 5.4**, by comparing the performances between frame beam reinforced part and non-reinforced part. Slope angle was cut to 75° , and slope geological structure was rock layer

structure, with slope angle bigger than the inclination of rock layer. But a part of this slope was fractured structure, so this part was reinforced by frame beam. The reinforcement parameters were shown in **Figure 5.4(b)**. Cross section of beams was 30cm×30cm, 6–10m bolts were applied at the beam joints to make frame beam work together with inner rock. Even if this slope experienced about 0.55g horizontal peak ground acceleration, reinforced part survived from Wenchuan earthquake, however, non-reinforced part collapsed and its debris destroyed the road. This comparison shows that slope reinforced by frame beam was stable and the anti-seismic property of frame beam was good.

In **Figure 5.5**, Slope was cut to 1:0.2 gradient and reinforced by soil nailing wall. Rock materials were dense sandy soil mixed with block rock. The diameter of soil nails was 10cm, with 7–12m length and 1.25m spacing. Shotcrete layer was 6–10cm thickness. Detailed reinforcement parameters were shown in **Figure 5.5(b)**. Fortification seismic intensity of this slope was VII scale of Chinese seismic intensity (coinciding with 0.1 seismic coefficient); the actually experienced seismic intensity was VIII scale. Although actual seismic intensity exceeded the design level, the stability of this slope was not affected by Wenchuan earthquake. Investigating other slopes reinforced by soil nailing wall, cracks and the exposure of steel mesh were induced, as shown in **Figure 5.6**, whereas these seismic damages had no effect on slope stability. The investigation results about slopes reinforced by soil nailing wall suggested this countermeasure had good ability to improve slope anti-seismic property.



(a) Slope reinforced by soil nailing wall



(b) Reinforcement parameters of soil nailing wall

Figure 5.5 Performance of soil nailing wall reinforced slope and its reinforcement parameters

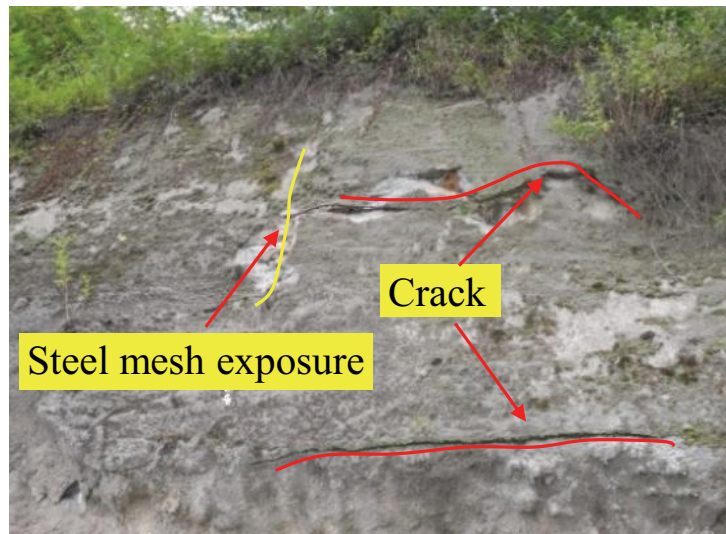
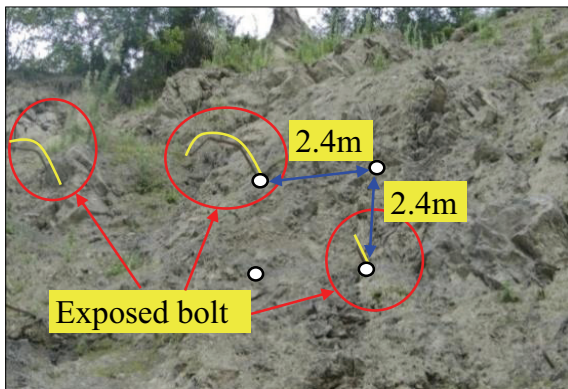
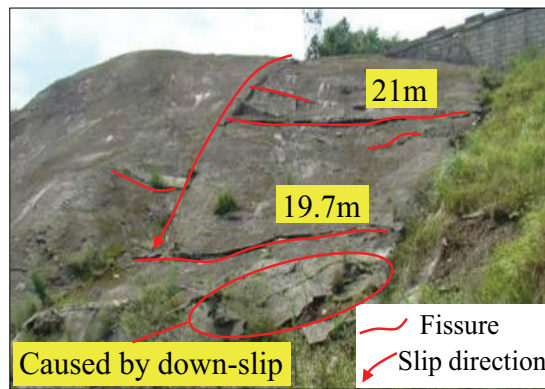


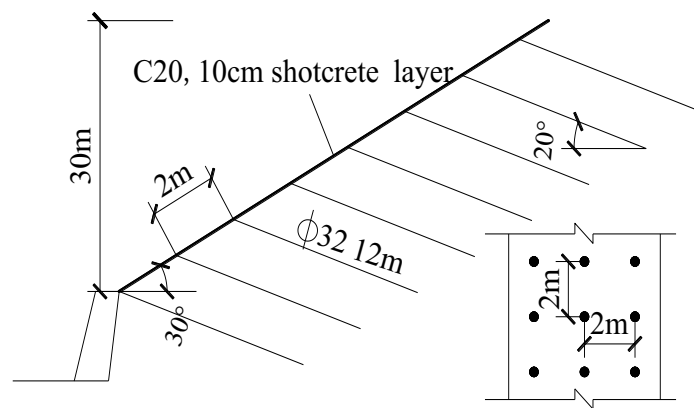
Figure 5.6 Cracks and steel mesh exposure of the slope reinforced by soil nailing wall



(a) Slope shallow collapse



(b) Shotcrete layer with fissures



(c) Reinforcement parameters of slope in (b)

Figure 5.7 Performance of slopes reinforced by shotcrete with bolts

Slope in the **Figure 5.7(a)** was reinforced by shotcrete with bolts, its slope angle was 67° , the length of bolts was 8–12m, with 2.4m spacing. Shotcrete layer was 8 cm thickness. This slope experienced about 0.35g horizontal peak ground acceleration during Wenchuan earthquake, it was triggered shallow collapse, resulting in bolts exposed 0.4–1m length. For the slope shown in **Figure 5.7(b)**, its slope angle was 30° , 12m bolts with 2m spacing were applied to reinforce this slope in the aid of 10cm shotcrete layer. As a result of this slope suffered about 0.3g horizontal peak ground acceleration and strong ground shaking, several fissures and down-slip movement of shotcrete layer were induced. The investigation results showed that shotcrete with bolts had limited ability to enhance slope stability during Wenchuan earthquake; its anti-seismic property depended on the parameters of shotcrete with bolts.

5.3 Comparison and analysis of four reinforcements

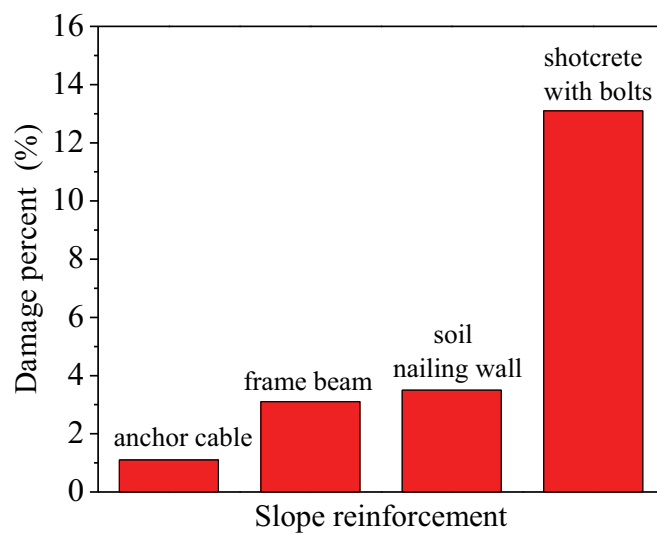


Figure 5.8 The comparison of damage percent among four reinforcements

As mentioned above, four reinforcements performed different anti-seismic behaviors and appeared different damaged patterns. Herein, damage of reinforced slope referred to the visible changes of status or configuration, from visible crack to slope failure. Since the area of crack was so difficult to be measured at the steep slope, therefore, the length of visible damage along the road extending orientation was measured to compare anti-seismic properties of different reinforcements. Statistical results of four reinforcements were shown in **Figure 5.8**, in which

damage percent referred to damaged length along road divided by the surveyed total length of each reinforcement. It suggested damage percents of anchor cable, frame beam and soil nailing wall were all less than 5%, but damage percent of shotcrete with bolts was 14%. The comparison implied that anchor cable, frame beam and soil nailing wall had good anti-seismic property, however, shotcrete with bolts had limited ability to enhance slope stability during the earthquake.

The reason was inferred that anchor cable and frame beam having good anti-seismic property was attributed to that cables or long bolts penetrated the potential sliding surface to make shallow layer work together with inner stable rock, then their deformations kept coordinated. As a result of slope deformation was effectively constrained by anchor cable or frame beam, thus, slopes reinforced by those countermeasures performed very well during the earthquake.

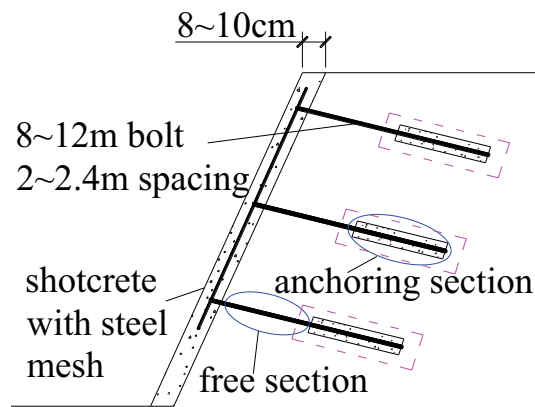


Figure 5.9 Reinforcement principle sketch of shotcrete with bolts

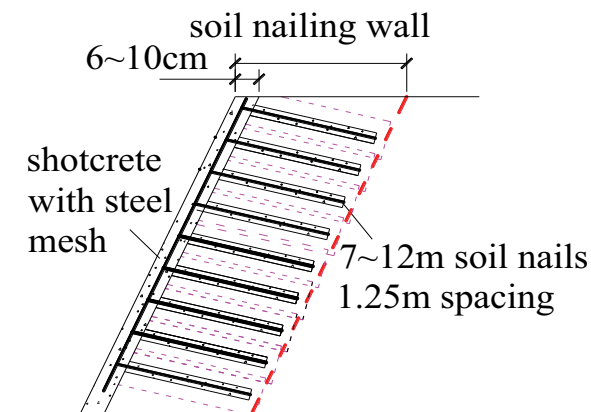


Figure 5.10 Reinforcement principle sketch of soil nailing wall

Comparing soil nailing wall and shotcrete with bolts, they are both flexible reinforcements, but soil nailing wall performed better during the earthquake. The reason was inferred that the whole length of soil nails interacted with soils, however, the bolt was divided into free section and grouting section, as shown in **Figure 5.9**. Therefore, the range reinforced by one soil nail was larger than that reinforced by one bolt; meanwhile, spacing between soil nails was smaller than that of bolts, thereby, soil nails, shotcrete layer and soils formed a compound body, which is like a gravity retaining wall, as shown in **Figure 5.10**. If some soil nails failed during earthquake, the compound body was hardly affected. Hence, the stability of slopes reinforced by soil nailing wall would be slightly affected. However, due to larger spacing, bolts weakly worked together, if one bolt was destroyed, affected zone would extend, then adjacent bolts became failure, finally resulted in slope instability.

Even though the anti-seismic property of shotcrete with bolts was not as good as other three reinforcements, it still improved slope stability. The limited anti-seismic ability was indirectly verified by the comparison of average collapse depth between non-reinforced slopes and shotcrete with bolts reinforced slopes. Average collapse depth of the slope reinforced by shotcrete with bolts was estimated from the exposed length of bolts. Average collapse depth of non-reinforced slope was estimated from typical longitudinal profile of slope, as shown in **Figure 3.2**.

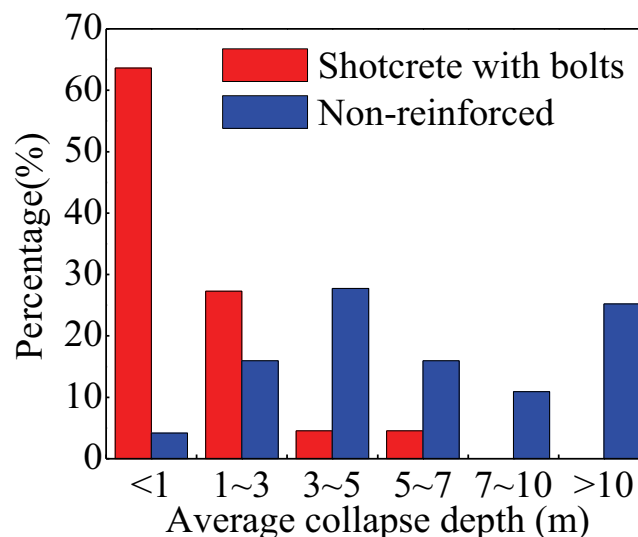


Figure 5.11 The comparison of average collapse depth between non-reinforced slopes and shotcrete with bolts reinforced slopes.

The result of average collapse depth comparison was shown in **Figure 5.11**. It suggested average collapse depth of non-reinforced slopes was 80% larger than 3 meters. However, average collapse depth of shotcrete with bolts reinforced slopes was 91% smaller than 3 meters and 64% smaller than 1 meter. Conclusion may be drawn that shotcrete with bolts was able to reduce sliding volume and mitigate disaster scale, whereas its anti-seismic ability depended on bolt length and spacing between bolts. If bolts were not long enough or sparse, the main effect of shotcrete with bolts was protecting slope from rock weathering rather than resisting earthquake.

5.4 Summary

In order to learn from seismic damage and take effective countermeasures to enhance slope stability, this chapter investigated four slope countermeasures along National Road 213 and Dujiangyan–Wenchuan expressway, the findings are following:

- (1) The rank of anti-seismic properties of investigated reinforcements is anchor cable, frame beam, soil nailing wall, shotcrete with bolts.
- (2) Anchor cable and frame beam could effectively restrain slope deformation; soil nails combine themselves with soil and form an analogical gravity retaining wall to improve slope anti-seismic property.
- (3) The anti-seismic ability of shotcrete with bolts was limited and depended on bolts length and spacing between bolts.

References

- Masuda, T, Fujii, N., Yamada, H, et al., 1996. The stability analysis of walls with the anchor on the earthquake. Proc. of annual conference of the Japan society of civil engineers. 51, 444–445. (In Japanese)
- Masuda, T, Fujii, N., Yamada, H, et al., 1997. The stability analysis of the walls with the anchor on the earthquake. Proc. of annual conference of the Japan society of civil engineers, 52, 396–397.1997. (In Japanese)

- Yamamoto, A., Toriihara, M., 2003. An earthquake-proof technique for ground anchorages. *Journal of Japan society of civil engineering*, 63(736), 153–166. (In Japanese with English abstract)
- Zhou, D.P., Zhang, J.J., Tang, Y., 2010. Seismic damage analysis of road slopes in Wenchuan earthquake. *Chinese Journal of Rock Mechanics and Engineering*, 29(3), 565–576. (In Chinese with English abstract)

Chapter 6 Conclusions and Future Perspectives

6.1 Finding summary

On May 12, 2008, a greatly destructive Wenchuan earthquake occurred in Longmenshan thrust fault belt. Due to frail geological environment and high earthquake magnitude, there were a huge number of slope failures and subsequent disasters. In this study, chapter 1 firstly introduced the tectonic and geological settings of Wenchuan earthquake, and then generally reported the damaged related with slope failure, further reviewed previous studies on slope failure distribution, slope stability and landslide mobility; From a whole viewpoint, chapter 2 discussed the relationship between slope failure distribution and seismic parameters from qualitative and quantitative aspects in the Wenchuan earthquake wholly affected area; various influential factors on slope stability and dynamic responses were explored in chapter 3, which were based on field investigation, theoretical derivation and numerical simulation; chapter 4 continued from chapter 3 to study the influential factors on landslide mobility and its travel distance based on 46 landslides with relatively long runout in Wenchuan earthquake area, so as to analyze the whole process from slope failure to post-failure performance. In the chapter 5, four reinforcements of slope were analyzed and compared with each other based on field investigation, intending to learn lessons from seismic damage. At last, some findings in this research are listed as follows:

- [1] Slope failure distribution exponentially decreased with the increment of epicentral distance and distance from surface fault rupture; the transforming section of rupturing motion and surface rupture end section had significant effect on the occurrence of slope failure.
- [2] The regressions of acceleration attenuation demonstrated that seismic ground acceleration on the hanging wall side was apparently larger than that on footwall side, which caused hanging-foot wall effect.

- [3] For Wenchuan earthquake, slope failure distribution (*LNC*, *LAP*) did not peak at epicenter but around the intersection between multiple co-seismic faults.
- [4] Slope failure distribution (*LNC*, *LAP*) with respect to surface fault rupture had highly linear correlation with seismic peak ground acceleration, implying that slope failure distribution attenuation had the same decaying form as seismic acceleration.
- [5] The threshold value of slope failure occurrence ranged within 182–212cm/s² horizontal PGA. Due to much wider area of susceptible lithology on the hanging wall, horizontal PGA of slope failure occurrence on the hanging wall side was 18% smaller than that of footwall side.
- [6] Landslide occurrence probability decreased with the increment of distance from the surface fault rupture, and increased with the horizontal peak ground acceleration.
- [7] High and steep slopes consisting of soft rock were more likely to be triggered as landslides.
- [8] Geological structures had significant effect on slope stability, and rock layer with more than 10° gradient in the same direction of slope inclination, namely GS2 geological structure, were relatively more susceptible to sliding.
- [9] The multivariable analysis revealed that the square root of sliding source area and cubic root of sliding source volume were linearly correlated with the combination of slope height, horizontal peak ground acceleration, inclination of rock layer, slope angle and rock type.
- [10] Stepwise regression results suggested that slope height, horizontal peak ground acceleration and geological structure were more influential to sliding source area and volume than slope angle and rock type during earthquake. Since sliding source area and volume are two most important impact factors of slope failure, the results implied that slope height, horizontal peak ground acceleration and geological structure had predominant influence on slope stability during earthquake among investigated five influential factors.
- [11] Theoretical solution has proved the elevation amplification effect. With elevation increase, displacement (velocity, acceleration) amplification ratio becomes larger; meanwhile, amplification ratio turns larger from slope inner to the outer.
- [12] The shape of contour plot of displacement amplification ratio is determined by seismic wave frequency; with the increment of frequency, the contour plot changes from nearly parallel to slope surface to rhythm distribution with multiple peak values. Lower frequency induces more dangerous dynamic responses.

- [13] The maximum displacement amplification ratio relies on Poisson's ratio, input angle of seismic wave and slope angle.
- [14] Mass density has smaller effect on slope dynamic responses than Young's modulus.
- [15] The thickness of saliently affected region by earthquake becomes larger with the increase of Young's modulus and seismic wave input angle, and with the decrease of seismic wave frequency.
- [16] Slope surface geometry shape has very limited influence on natural frequency of low order vibration mode.
- [17] Seismic acceleration was generally amplified with the increment of slope elevation, especially, at the steep section and ground surface curvature sharp changing section.
- [18] Slopes with convex and S-like shape are much more unstable than other three shapes of slope during earthquakes; step-like slopes have relatively higher stability; concave slopes and inverse S-like slopes have medium stability.
- [19] Landslide travel distance (L_{\max}) had relatively strongly linear correlation with landslide height (H_{\max}).
- [20] Multivariable analysis revealed that slope height, rock type, slope transition angle and landslide volume were the most important influential factors on landslide mobility, and followed by slope angle; seismic acceleration had weakest effect on landslide mobility.
- [21] Rock type, landslide volume and slope transition angle were more influential than slope height, seismic acceleration and slope angle on landslide travel distance.
- [22] Two empirical models, as Eq.(4.1) and (4.2), were proposed to predict equivalent coefficient of friction and travel distance in similar geological conditions as Wenchuan earthquake affected area.
- [23] The rank of anti-seismic properties of investigated reinforcements is anchor cable, frame beam, soil nailing wall, shotcrete with bolts.
- [24] Anchor cable and frame beam could effectively restrain slope deformation; soil nails combine themselves with soil and form an analogical gravity retaining wall to improve slope anti-seismic property.
- [25] The anti-seismic ability of shotcrete with bolts was limited and depended on bolts length and spacing between bolts.

6.2 Future research topics

As a result of catastrophic earthquake, there were a large amount of slope failures triggered by the 2008 Wenchuan earthquake; meanwhile, destructive magnitude heavily disturbed the environment along Longmenshan fault zone, where is so vulnerable as to be easily induced slope failure during rainfall seasons, such as, Sept.2008, Beichuan debris flows, Aug.2010 Zhouqu mudslide. Hence, there are lots of challenges to researchers for mitigating not only earthquake-induced disasters but also the subsequent disasters after earthquake.

1. Perspective research topics about earthquake-induced landslides

- Because topographical and geological factors have significant effect on slope failure, hence, slope failure distribution attenuation model should consider these influences; however, due to lack of geological data of earthquake wholly affected area, the model in chapter 2 was limited to analyze the correlation between slope failure distribution and earthquake parameters. Therefore, the empirical model proposed for slope failure distribution attenuation is needed to be improved. V_{s30} is recommended to reflect comprehensive effects from topography and geology, because V_{s30} has some empirical relations with these two conditions based on recent research results.
- Slope stability is affected by numerous factors. Although the effects of various factors have been discussed in chapter 3, it is not enough and it is necessary to research more. Especially, the effect of interplay between ground water and rock (or soils) under seismic conditions on slope stability.
- After slope failure, rapid or long travel landslide severely endanger the lives and properties along travel path, further studies on the mechanism of these types of geo-hazard are strongly necessary to understand their initiation, development and movement.
- Since large or huge landslide is nearly impossible to be prevented, hence, the prediction of landslide mobility and travel distance is very important to previously evacuate residents.

2. Perspective research topics about post-earthquake slope stability

- Due to heavily environmental disturbance induced by Wenchuan earthquake, it is easy to trigger landslide during rainfall seasons in the Wenchuan earthquake affected mountainous

area, hence, the monitoring and early-warning of potential landslide is essential to protect lives and properties.

- Slope reinforcements are effective countermeasures to mitigate the damage caused by slope failure, so their anti-seismic behaviors and validities are needed to be further researched.

Appendix

Table 1: The parameters of 187 strong motion stations

Station code	Latitude(°)	Longitude(°)	PGA of EW comp.(cm/s ²)	PGA of NS comp.(cm/s ²)	PGA of UD comp.(cm/s ²)	PGA of horizontally vectorial composition(cm/s ²)	D _{rup} (km)	Hanging wall/ Footwall
51WCW	103.2	31	957.70	652.85	948.10	1039.92	11.17	Hanging wall side
51MXT	103.9	31.7	-306.58	302.16	-266.64	345.77	25.62	Hanging wall side
51MXN	103.7	31.6	-421.29	349.24	-352.48	480.53	30.21	Hanging wall side
51LXT	103.5	31.6	339.73	342.38	379.58	349.49	42.72	Hanging wall side
51XJD	102.6	31	-94.87	132.09	-83.66	136.01	50.27	Hanging wall side
51LXM	103.3	31.6	320.94	-283.84	357.81	338.70	55.36	Hanging wall side
51XJB	102.4	31	67.93	73.79	-41.83	98.92	63.47	Hanging wall side
51MXD	103.7	32	246.49	-206.21	-143.91	246.66	63.48	Hanging wall side
51PWM	104.5	32.6	273.74	287.37	177.38	289.57	63.84	Hanging wall side
51LXS	102.9	31.5	221.26	261.75	211.09	276.05	71.11	Hanging wall side
62WIX	104.5	33	-142.69	-141.16	-131.97	196.72	96.32	Hanging wall side
51HSL	103.3	32.1	-107.64	-142.57	-108.97	156.45	96.7	Hanging wall side
62WUD	105	33.4	-184.87	-163.99	108.62	186.60	98.34	Hanging wall side
51SPA	103.6	32.5	-186.54	131.63	89.28	186.70	110.95	Hanging wall side
51JZW	104.2	33	-128.17	173.72	81.52	177.05	115.68	Hanging wall side
51HSD	103	32.1	-102.49	89.76	-51.65	111.38	116.3	Hanging wall side
51JZG	104.3	33.1	-169.75	241.45	109.26	244.27	117.76	Hanging wall side
51SPT	103.6	32.6	-40.15	29.78	24.39	41.83	119.18	Hanging wall side
51JZY	104.3	33.2	-91.74	100.04	65.31	106.51	125.9	Hanging wall side
62TSH	105.9	34.5	-130.62	-116.59	-51.47	143.23	130.49	Hanging wall side
51SPC	103.6	32.8	37.78	-40.86	-21.06	42.56	136.67	Hanging wall side

Station code	Latitude(°)	Longitude(°)	PGA of EW comp.(cm/s ²)	PGA of NS comp.(cm/s ²)	PGA of UD comp.(cm/s ²)	PGA of horizontally vectorial composition(cm/s ²)	D _{rup} (km)	Hanging wall/ Footwall
51MEZ	102.3	31.9	57.64	42.47	35.58	59.09	137.57	Hanging wall side
51JZB	104.1	33.3	-96.00	-112.20	-70.84	112.45	147.25	Hanging wall side
51MED	102.2	31.9	-27.64	23.74	18.86	29.71	148.4	Hanging wall side
62SHW	104.5	33.7	-91.45	108.78	58.91	120.14	154.97	Hanging wall side
51JZZ	103.8	33.3	167.49	-299.49	-127.11	318.28	165.21	Hanging wall side
62ZHQ	104.4	33.8	-32.50	-37.86	22.65	42.88	168.93	Hanging wall side
62TCH	104.4	34.1	74.47	83.96	43.31	88.62	193.5	Hanging wall side
51LHT	100.7	31.4	6.96	-8.93	-5.89	9.54	209.07	Hanging wall side
62JNI	105.8	35.5	-14.92	-9.55	13.01	15.03	218.72	Hanging wall side
62MXT	104	34.4	-70.63	-44.98	25.26	75.31	242.18	Hanging wall side
51GZX	100	31.6	5.72	-3.03	-3.65	5.93	271.64	Hanging wall side
51GZT	100	31.6	5.25	4.82	3.02	5.85	272.03	Hanging wall side
62ZNI	103.5	34.6	-18.38	-19.47	-9.86	25.36	290.36	Hanging wall side
62LTA	103.4	34.7	-7.44	10.24	6.60	10.26	305.01	Hanging wall side
62XKY	104.2	35.8	12.47	17.40	-8.93	18.02	341.95	Hanging wall side
62KLE	103.7	35.4	-16.51	15.41	7.78	17.06	342.74	Hanging wall side
62BAS	103.5	35.3	-17.87	-17.80	-6.75	19.02	347.71	Hanging wall side
62QSY	104.2	35.9	17.98	-18.16	-10.36	20.84	349.17	Hanging wall side
62HEP	104	36	41.17	-44.16	-24.78	53.46	360.78	Hanging wall side
62HEZ	102.9	35	-8.03	10.27	3.95	11.03	360.78	Hanging wall side
62YSH	103.9	35.8	-12.35	-10.14	-8.07	13.13	360.87	Hanging wall side
62LDA	104	35.9	-7.59	-7.73	-6.95	8.11	361.94	Hanging wall side
62JAI	104.1	36	21.13	10.88	-6.58	21.49	363.38	Hanging wall side
62ZPU	103.7	35.8	11.52	-11.27	-8.45	11.64	372.53	Hanging wall side

Station code	Latitude(°)	Longitude(°)	PGA of EW comp.(cm/s ²)	PGA of NS comp.(cm/s ²)	PGA of UD comp.(cm/s ²)	PGA of horizontally vectorial composition(cm/s ²)	D _{rup} (km)	Hanging wall/ Footwall
62YTA	103.9	36.1	7.90	-7.55	-4.68	8.48	383.66	Hanging wall side
62GXT	103.9	36.1	14.83	10.22	6.98	16.16	384.18	Hanging wall side
62DZJ	103.9	36.1	-17.93	-21.14	-11.58	21.36	384.4	Hanging wall side
62ERT	103.8	36.1	17.28	17.23	9.81	17.47	390.13	Hanging wall side
62YLG	103.7	35	8.22	10.93	8.86	10.94	390.54	Hanging wall side
62HJI	103	35.5	-9.56	7.53	-4.68	10.96	393.34	Hanging wall side
62BWG	103.7	36.1	-7.27	-6.53	4.27	8.40	396.25	Hanging wall side
62LJB	103.7	36.1	16.92	-15.49	-8.47	17.15	396.95	Hanging wall side
62CJA	103.7	36.1	15.77	-14.63	7.25	16.09	397.16	Hanging wall side
62ZHH	103.8	36.2	9.94	10.60	8.76	10.73	398.78	Hanging wall side
62XGU	103.6	36.1	-20.14	13.00	8.44	20.68	405.38	Hanging wall side
62GLA	103.9	36.4	15.75	18.18	-6.40	19.12	408	Hanging wall side
62CHJ	103.5	36.1	12.61	-11.39	-7.80	13.88	409.66	Hanging wall side
62YJN	103.3	36	11.63	-11.88	5.22	14.75	413.36	Hanging wall side
62TZY	103.8	36.4	-13.58	-11.51	5.54	13.59	415.14	Hanging wall side
63HEN	101.6	34.7	-3.71	3.44	2.06	3.71	416.98	Hanging wall side
62DSH	103.6	36.3	13.72	-15.14	11.49	15.24	419.03	Hanging wall side
62ZXX	103.6	36.3	16.80	-15.11	-8.50	18.86	419.49	Hanging wall side
62SHP	103.6	36.3	7.73	7.48	-6.30	8.56	421.34	Hanging wall side
62YGX	103.3	36.1	-6.28	6.34	3.64	6.67	422.31	Hanging wall side
62PAN	103.3	36.2	15.00	-11.54	-6.61	16.67	429.97	Hanging wall side
62XIC	103.6	36.5	10.80	13.07	-8.49	13.24	435.04	Hanging wall side
62HUZ	103.2	36.2	8.22	-9.13	4.23	10.83	436.38	Hanging wall side
62HZU	103.1	36.2	11.30	7.21	-4.71	11.40	443.35	Hanging wall side

Station code	Latitude(°)	Longitude(°)	PGA of EW comp.(cm/s ²)	PGA of NS comp.(cm/s ²)	PGA of UD comp.(cm/s ²)	PGA of horizontally vectorial composition(cm/s ²)	D _{rup} (km)	Hanging wall/ Footwall
62QCH	103.6	36.7	-8.26	-5.83	-5.71	8.60	450.4	Hanging wall side
63TOR	102.1	35.5	-2.96	-3.53	2.55	3.53	451.15	Hanging wall side
62DAT	103.4	36.6	-16.15	-10.97	-7.97	16.27	455.23	Hanging wall side
62HGU	103	36.3	-7.20	6.49	3.16	7.31	457.39	Hanging wall side
63MIH	102.9	36.3	-13.39	-11.91	-5.03	13.41	463.36	Hanging wall side
62XHS	102.9	36.4	8.23	7.31	5.22	8.33	472.02	Hanging wall side
62HEQ	102.9	36.5	8.44	9.16	-4.71	9.34	479.12	Hanging wall side
63DAW	100.3	34.5	1.70	1.59	-1.36	1.78	481.27	Hanging wall side
62TOY	103	36.7	-7.87	-5.41	3.07	7.88	491.79	Hanging wall side
62DTX	103.4	37.3	-4.34	4.81	3.55	4.85	511.06	Hanging wall side
63LED	102.4	36.6	2.08	-2.43	2.08	2.94	518.84	Hanging wall side
62DCG	103	37.1	-8.17	9.10	-3.38	9.68	519.18	Hanging wall side
62PYJ	103.5	37.5	6.09	-5.76	-3.03	7.44	520.49	Hanging wall side
62HZT	103.6	37.6	8.82	-6.61	-3.84	9.69	522.08	Hanging wall side
62JQY	102.9	37.1	-5.17	-4.72	-2.54	6.87	526.77	Hanging wall side
62ANY	102.9	37.3	6.73	-4.54	3.37	7.18	534.18	Hanging wall side
62XIJ	103.4	37.6	6.21	-6.07	2.91	6.68	535.08	Hanging wall side
62HYC	103.1	37.4	-6.53	-5.45	4.09	6.54	539.07	Hanging wall side
63GUD	101.4	36.1	-3.10	-4.80	-2.38	5.09	543.64	Hanging wall side
63GUN	100.7	35.6	-1.58	-1.64	1.58	1.69	545.93	Hanging wall side
62HSY	102.9	37.4	5.29	-7.04	-2.63	7.86	550.14	Hanging wall side
63XIN	101.7	36.6	3.18	3.30	2.67	3.50	563.6	Hanging wall side
62CCX	102.9	37.9	9.58	8.20	3.02	11.25	588.19	Hanging wall side
62JDN	102.7	38.1	6.13	7.32	2.46	9.54	617.85	Hanging wall side

Station code	Latitude(°)	Longitude(°)	PGA of EW comp.(cm/s ²)	PGA of NS comp.(cm/s ²)	PGA of UD comp.(cm/s ²)	PGA of horizontally vectorial composition(cm/s ²)	D _{rup} (km)	Hanging wall/ Footwall
62HYS	102.9	38.4	-5.35	4.97	2.09	6.01	629.5	Hanging wall side
63DUL	98.1	36.3	1.20	-0.94	0.61	1.31	763.93	Hanging wall side
63QIL	100.2	38.2	0.87	-1.12	-1.05	1.29	782.53	Hanging wall side
63DLH	97.4	37.4	0.44	-0.44	0.88	0.51	897.21	Hanging wall side
51MZQ	104.1	31.5	-824.13	802.71	622.91	911.97	3.08	Footwall side
51JYH	104.6	31.8	-519.49	-350.14	-444.33	526.93	8.58	Footwall side
51BXZ	102.9	30.5	153.26	-117.08	109.25	162.16	9.14	Footwall side
51BXY	102.9	30.5	-190.23	-155.70	93.70	190.74	9.26	Footwall side
51LDS	102.2	29.9	44.63	-50.74	32.02	54.77	10.26	Footwall side
51BXD	102.8	30.4	-73.81	-77.54	50.99	95.58	10.39	Footwall side
51SFB	104	31.3	556.17	-581.59	633.09	665.10	13.54	Footwall side
51JYD	104.7	31.8	-511.33	458.68	-198.28	604.45	15.25	Footwall side
51AXT	104.3	31.5	-289.54	203.45	179.93	311.95	15.31	Footwall side
51LDL	102.2	29.8	-109.49	-120.30	46.77	120.31	18.36	Footwall side
51TQL	102.4	29.9	-123.28	115.73	40.28	132.42	24.08	Footwall side
51JYC	105	31.9	297.19	278.96	-180.49	317.61	25.47	Footwall side
51LDJ	102.2	29.7	47.52	58.27	-35.61	58.31	26.82	Footwall side
51GYZ	106.1	32.6	424.48	-410.48	-183.34	483.11	29.06	Footwall side
51LSJ	102.9	30.2	-118.15	-112.16	59.92	122.87	33.33	Footwall side
51JLT	104.5	28.2	16.77	-13.26	6.52	16.84	35.19	Footwall side
51LDD	102.2	29.6	109.42	-112.08	-56.02	120.15	35.29	Footwall side
51PXZ	103.8	30.9	120.52	142.20	99.12	148.67	35.68	Footwall side
51DXY	103.5	30.6	-135.11	-127.64	82.69	159.05	40.92	Footwall side
51LSF	102.9	30.1	124.15	94.03	47.66	126.61	40.96	Footwall side

Station code	Latitude(°)	Longitude(°)	PGA of EW comp.(cm/s ²)	PGA of NS comp.(cm/s ²)	PGA of UD comp.(cm/s ²)	PGA of horizontally vectorial composition(cm/s ²)	D _{rup} (km)	Hanging wall/ Footwall
51LSH	102.9	30.1	-91.49	-84.89	-49.22	91.87	41.2	Footwall side
51SMK	102.1	29.4	41.95	29.47	-17.34	42.71	43.56	Footwall side
51QLY	103.3	30.4	-173.78	-199.85	55.09	204.42	43.72	Footwall side
51DYB	104.5	31.3	-126.29	-136.33	88.99	139.30	44.82	Footwall side
51HYY	102.5	29.7	82.72	-80.78	38.30	93.53	46.93	Footwall side
51GYS	105.8	32.2	320.49	273.97	-143.70	350.82	50.49	Footwall side
51SMW	102.2	29.4	-75.61	-93.89	-60.94	94.57	50.86	Footwall side
51YAM	103.1	30.1	171.16	175.37	46.69	204.07	54.66	Footwall side
51YAD	103	30	-153.58	141.58	75.98	173.80	55.92	Footwall side
51YAL	102.9	29.9	93.05	-117.37	64.88	129.64	57.5	Footwall side
51PJD	103.4	30.3	-195.81	-190.33	-58.99	211.52	58.45	Footwall side
51HYQ	102.6	29.6	142.33	125.19	54.42	144.81	61.63	Footwall side
51YAS	103	29.9	102.11	-91.19	-32.70	117.37	63.69	Footwall side
51JLT	101.5	29	16.77	-13.26	6.52	16.84	64.45	Footwall side
51SMX	102.3	29.3	62.40	-81.33	33.74	88.07	64.88	Footwall side
51HYJ	102.6	29.5	-74.90	-83.04	-46.70	96.86	69.73	Footwall side
51SMM	102.4	29.3	72.42	-85.54	34.88	102.95	71.6	Footwall side
51PIW	103.6	30.3	97.74	101.17	-46.90	113.76	72.52	Footwall side
51XJL	103.8	30.4	107.64	89.13	39.33	108.36	76.65	Footwall side
51CDZ	104.1	30.6	-79.80	69.72	-45.33	83.17	78.85	Footwall side
51SMC	102.3	29.1	76.39	-103.33	-34.78	111.88	81.62	Footwall side
51SML	102.3	29	49.81	40.56	21.10	59.33	88.79	Footwall side
51CXQ	105.9	31.7	-184.83	-166.93	-69.86	228.34	99.25	Footwall side
51MNA	102.1	28.7	16.47	27.12	13.03	27.13	99.8	Footwall side

Station code	Latitude(°)	Longitude(°)	PGA of EW comp.(cm/s ²)	PGA of NS comp.(cm/s ²)	PGA of UD comp.(cm/s ²)	PGA of horizontally vectorial composition(cm/s ²)	D _{rup} (km)	Hanging wall/ Footwall
51HYW	102.9	29.2	63.22	49.02	34.40	63.77	113.25	Footwall side
51MNJ	102.2	28.6	-14.54	17.73	-10.75	19.05	115.12	Footwall side
51MNH	102.1	28.5	-19.91	22.50	-9.33	23.59	116.07	Footwall side
51MNC	102.3	28.6	45.87	47.94	15.17	51.93	121.29	Footwall side
51YXX	102.5	28.7	74.38	-76.63	-32.81	87.10	126.72	Footwall side
51YXZ	102.5	28.6	-52.46	-51.86	22.75	54.68	135.33	Footwall side
51XDM	102.3	28.4	-31.77	17.18	17.72	31.98	137.66	Footwall side
51MNL	102.2	28.3	-41.94	-54.10	15.44	54.25	138.52	Footwall side
51YYM	101.4	27.5	9.26	-9.37	-5.63	12.17	147.02	Footwall side
51XDG	102.4	28.3	-17.72	-12.91	-8.32	18.09	152.26	Footwall side
51XCL	102.2	28.1	-15.90	-22.05	-11.56	24.98	153.83	Footwall side
51YYW	101.7	27.5	11.25	9.22	6.17	12.23	168.06	Footwall side
51XCT	102.2	27.9	-5.65	8.76	4.09	8.83	170.74	Footwall side
51XCX	102.2	27.9	5.75	-4.13	3.21	6.01	171.52	Footwall side
51YYJ	102	27.7	-9.45	-11.35	7.50	11.36	172.87	Footwall side
51XCZ	102.3	27.9	23.50	25.12	12.13	26.33	177	Footwall side
51XCC	102.3	27.9	23.22	29.10	9.96	31.78	177.34	Footwall side
51MCL	103.7	29	98.52	82.33	41.49	100.80	182.83	Footwall side
51XCY	102.2	27.7	19.15	-16.58	7.62	20.83	186.39	Footwall side
51MBD	103.5	28.8	-41.96	-40.55	-19.59	47.13	186.5	Footwall side
51XCH	102.2	27.6	-8.16	-10.82	-9.61	10.82	194.04	Footwall side
51ZJJ	102.6	27.9	8.90	7.18	-4.48	8.93	197.82	Footwall side
51ZJQ	102.8	28	-14.41	-11.74	-5.67	14.48	204.36	Footwall side
51DCN	102.2	27.4	10.31	-10.02	-6.57	11.23	211.5	Footwall side

Station code	Latitude(°)	Longitude(°)	PGA of EW comp.(cm/s ²)	PGA of NS comp.(cm/s ²)	PGA of UD comp.(cm/s ²)	PGA of horizontally vectorial composition(cm/s ²)	D _{rup} (km)	Hanging wall/ Footwall
51PZT	101.5	26.7	4.38	3.97	-1.70	5.05	217.89	Footwall side
51PZF	101.4	26.6	2.52	1.42	-2.16	2.68	218.93	Footwall side
51BTD	102.8	27.7	12.09	-10.63	-10.15	15.68	228.56	Footwall side
51LBH	103.8	28.5	-24.88	-26.52	14.75	30.69	230.41	Footwall side
51LBD	103.6	28.3	-13.57	13.03	9.91	14.47	233.15	Footwall side
514ZG	104.8	29.3	55.03	47.72	19.97	55.32	233.72	Footwall side
51YBY	104.6	29	-36.79	32.12	15.80	36.80	234.13	Footwall side
51BTT	102.8	27.6	-10.43	10.26	5.26	12.54	236.76	Footwall side
51HLY	102.3	27.1	4.91	4.18	2.76	4.99	241.42	Footwall side
51MYL	102.1	26.9	8.21	-10.65	5.07	11.16	243.7	Footwall side
51MYS	102	26.8	-5.91	5.96	2.01	6.58	245.1	Footwall side
51FSB	104.8	29.1	-32.06	-24.73	-12.79	32.57	248.96	Footwall side
51HLB	102.3	27	-4.92	5.66	-3.20	6.96	249.07	Footwall side
51NNS	102.6	27.2	-5.47	-5.18	3.30	5.68	254.07	Footwall side
51YBH	101.9	26.5	6.21	6.91	3.53	7.03	261.38	Footwall side
51HWB	102.3	26.8	-5.64	-5.72	-3.02	6.76	264.81	Footwall side
51NNL	102.7	27.1	6.36	6.20	3.14	7.79	269.76	Footwall side
51NNT	102.8	27.1	6.03	8.33	-4.72	8.39	275.98	Footwall side
51HLF	102.1	26.5	-4.94	-3.85	2.33	5.11	276.42	Footwall side
51CNT	104.9	28.6	-18.60	14.20	-8.41	20.24	287.4	Footwall side
51NNH	102.9	26.9	-4.38	-3.55	-2.54	4.53	299.49	Footwall side
51JLN	101.7	28.8	25.26	22.30	11.99	27.13	301.89	Footwall side

Table 2: 119 landslides in Wenchuan County induced by Wenchuan earthquake

Latitude, Longitude	D_{rup}	PHA (gal)	Slope angle (θ°)	Slope height (h , m)	Rock type	Geological structure, (joint inclination, δ°)	Source area ($\times 10^4 m^2$)	Source volume ($\times 10^4 m^3$)	Intensity
30°53'52"N,103°19'33"E	5	865.53	32.5	93	RT3	5	3.6	5.5	XI
31°06'41"N,103°17'46"E	11.26	369.26	47	62	RT4	6	0.6	1.21	XI
30°56'52"N,103°23'31"E	4.97	505.20	34	49	RT2	7	1.4	5.6	XI
31°05'45"N,103°14'42"E	16.55	546.41	48	82	RT3	8	1.6	5.7	X
31°31'55"N,103°31'18"E	34.8	328.60	52	196	RT4	9	4.3	46.7	IX
31°03'57"N,103°23'24"E	4.97	866.76	25	45	RT4	11	0.42	5.88	XI
31°19'30"N,103°27'38"E	19.8	491.65	23	100	RT1	13	2.4	12	XI
31°14'59"N,103°23'05"E	19.1	502.62	23.5	145	RT4	14	13	160	X
31°34'34"N,103°34'28"E	34.9	327.84	28	280	RT4	18	0.57	2.3	VIII
30°53'45"N,103°20'30"E	4.85	871.72	26.5	146	RT1	19	7.9	78	XI
31°28'35"N,103°35'55"E	24.6	426.41	27	90	RT4	22	5.5	76.8	X
31°30'24"N,103°34'01"E	29.6	372.95	39	25	RT4	25	0.45	2.7	VIII
31°34'01"N,103°32'23"E	37.61	308.29	37	90	RT4	26	0.9	5.6	VIII
31°17'22"N,103°26'32"E	18.44	513.35	37	28	RT2	26	0.43	1.5	X
31°05'33"N,103°14'28"E	16.54	546.59	34	31	RT4	26	0.17	1.35	XI
31°04'57"N,103°18'39"E	9.5	709.99	32	110	RT4	26	13	27	IX
30°54'37"N,103°01'38"E	12.14	639.82	37	88	RT4	26	4.1	6.7	XI
31°28'36"N,103°35'28"E	26.84	400.92	18	80	RT3	27	4.5	35	X
31°26'33"N,103°32'45"E	25	421.66	32.5	237	RT4	27	24	480	X
31°28'08"N,103°37'04"E	23.88	435.21	30	250	RT4	27	1.8	5.4	X

Latitude, Longitude	D_{rup}	PHA (gal)	Slope angle (θ°)	Slope height (h , m)	Rock type	Geological structure, (joint inclination, θ°)	Source area ($\times 10^4 \text{m}^2$)	Source volume ($\times 10^4 \text{m}^3$)	Intensity
30°54'08"N, 103°19'07"E	3.92	911.88	47	139	RT3	27	1.9	15.2	XI
31°06'45"N, 103°15'21"E	17.19	534.81	31.5	37	RT4	29	0.61	6.7	XI
31°36'06"N, 103°31'08"E	41.67	282.54	33	250	RT4	30	4.3	27.9	VIII
31°36'43"N, 103°34'52"E	39.04	298.77	42.5	150	RT4	30	0.6	2.5	VIII
30°55'05"N, 103°03'09"E	9.9	698.52	35	120	RT4	30	11	41	IX
31°33'38"N, 103°31'40"E	37.68	307.81	37.5	65	RT4	31	1	6.3	VIII
30°56'54"N, 103°17'30"E	1.29	1044.81	39	34	RT4	32	1.49	1.7	XI
30°53'54"N, 103°21'28"E	5.02	503.78	23	27	RT1	34	0.8	3.9	XI
31°05'29"N, 103°14'23"E	16.33	550.50	25	80	RT1	34	0.6	3	X
31°19'37"N, 103°28'36"E	19.5	496.30	30	50	RT4	35	0.56	2.8	X
31°14'10"N, 103°24'48"E	17.34	532.15	49.5	130	RT2	35	1.6	69	IX
31°27'14"N, 103°34'18"E	24.8	424.02	40	191	RT4	36	8.12	243.6	X
31°33'59"N, 103°32'20"E	37.63	308.15	43	67	RT4	37	0.6	3.5	VIII
31°06'24"N, 103°17'53"E	10	390.88	41	110	RT3	37	1.5	21	IX
30°56'25"N, 103°25'25"E	7.75	435.64	23	61	RT2	37	1	6.5	XI
31°07'31"N, 103°15'50"E	17.42	530.75	48	86	RT2	37	0.5	1.8	X
31°07'15"N, 103°15'52"E	17.27	533.39	30	80	RT4	37	0.72	4.5	XI
31°00'46"N, 103°09'31"E	12.42	351.18	42	56	RT4	38	1.1	2.7	IX
31°07'25"N, 103°29'19"E	3.71	921.39	44	145	RT4	38	2	16	XI
30°54'43"N, 103°21'10"E	4.51	886.04	40	68	RT4	39	1.96	144.4	XI
31°24'20"N, 103°30'44"E	24.3	430.04	45	65	RT3	40	0.32	2.25	XI

Latitude, Longitude	D_{rup}	PHA (gal)	Slope angle (θ°)	Slope height (h , m)	Rock type	Geological structure, (joint inclination, θ°)	Source area ($\times 10^4 m^2$)	Source volume ($\times 10^4 m^3$)	Intensity
31°19'46"N, 103°27'35"E	20	488.59	55	100	RT4	40	1.6	11.2	XI
31°28'56"N, 103°36'23"E	24.57	426.77	34	149	RT3	41	1.5	10	X
30°53'42"N, 102°59'14"E	13.45	609.33	45	59	RT3	42	1.3	7.2	IX
31°06'51"N, 103°17'39"E	12.9	621.82	30	260	RT4	43	10.2	9.6	XI
30°59'22"N, 103°28'03"E	4.7	877.98	55	112	RT4	43	1.55	1.09	X
31°07'31"N, 103°16'32"E	16.55	546.41	52	277	RT3	45	0.8	23	X
31°01'57"N, 103°10'48"E	12.52	630.71	60	90	RT3	46	1.5	2.2	IX
31°26'58"N, 103°32'35"E	27.54	393.49	38	236	RT3	49	12	72	IX
31°31'12"N, 103°32'50"E	32.27	348.96	61	70	RT4	52	0.8	2.4	VIII
31°27'50"N, 103°33'06"E	28.22	386.50	40	600	RT4	52	8.6	68.8	IX
31°28'31"N, 103°34'48"E	27.4	394.95	40	20	RT3	52	4	20	VIII
31°20'04"N, 103°27'57"E	20	488.59	47	156	RT1	55	1.8	3.6	X
30°54'20"N, 103°20'29"E	4.98	504.92	28	64	RT4	55	1.2	4.7	XI
31°12'11"N, 103°22'44"E	16.62	545.12	58	50	RT2	56	0.32	1.3	X
31°19'41"N, 103°27'38"E	19.8	491.65	47	150	RT1	57	2.86	11.4	X
31°17'32"N, 103°26'45"E	18.28	516.01	47	176	RT4	61	4.9	9.8	XI
30°57'05"N, 103°04'22"E	13.47	336.13	52	205	RT3	84	2.3	6.8	X
30°56'55"N, 103°04'54"E	11.2	663.37	46	83	RT4	85	0.8	2	IX
30°55'40"N, 103°20'14"E	3	954.87	43	52	RT3	87	1.57	2.3	XI
30°54'49"N, 103°01'18"E	12.95	620.67	32.5	110	RT3	88	2.2	23	IX
30°58'45"N, 103°27'34"E	5.01	504.06	47	164	RT2	89	1.78	6.3	X

Latitude, Longitude	D_{rup}	PHA (gal)	Slope angle (θ°)	Slope height (h , m)	Rock type	Geological structure, (joint inclination, θ°)	Source area ($\times 10^4 m^2$)	Source volume ($\times 10^4 m^3$)	Intensity
30°54'54"N,103°24'04"E	8.43	421.18	39	350	RT2	92	7.1	213.42	X
31°27'42"N,103°37'06"E	22.82	448.76	35	200	RT2	94	6.97	29.29	X
31°15'11"N,103°23'11"E	19.1	502.62	30	142	RT4	95	12.9	324.5	X
31°36'31"N,103°34'35"E	38.77	300.53	30	200	RT3	98	2	20	VIII
30°53'46"N,103°20'30"E	4.92	506.63	30	124	RT1	99	6	120	XI
31°07'29"N,103°15'39"E	17.92	522.09	39	210	RT2	101	2.1	40	X
31°27'24"N,103°34'41"E	23.91	434.84	30	105	RT4	104	2.5	7	X
30°59'48"N,103°27'35"E	4.99	865.94	26	64	RT2	104	1.47	5.89	XI
30°56'54"N,103°04'40"E	11.7	650.66	51	56	RT3	105	0.19	1.56	X
30°54'09"N,103°00'33"E	12.72	626.00	35	110	RT4	106	1.6	11	X
31°28'53"N,103°34'36"E	28.19	386.80	27.5	306	RT4	107	4.25	85	VIII
31°01'43"N,103°30'02"E	4.91	869.23	31	142	RT4	108	6.33	117.5	X
30°53'48"N,103°00'30"E	11.5	655.70	42	97	RT3	110	1.26	5.67	IX
30°57'21"N,103°05'40"E	10	695.70	43	90	RT3	110	0.8	5.2	IX
30°55'34"N,103°03'13"E	10.9	671.21	39	62	RT3	112	0.42	2.33	IX
30°55'55"N,103°03'28"E	11.25	369.43	41	110	RT3	113	1	60	X
31°02'47"N,103°28'15"E	1.73	1020.30	51	71	RT3	113	1.7	6.7	XI
31°07'10"N,103°15'15"E	17.9	522.44	36	150	RT2	115	2	20	X
31°17'50"N,103°26'45"E	19.2	501.02	25	196	RT4	118	9.2	45.08	X
31°37'09"N,103°34'49"E	39.41	296.39	30	125	RT4	119	23.4	140	IX
30°53'24"N,102°58'31"E	13.7	603.80	40	67	RT3	121	1.4	18	X

Latitude, Longitude	D_{rup}	PHA (gal)	Slope angle (θ°)	Slope height (h , m)	Rock type	Geological structure, (joint inclination, θ°)	Source area ($\times 10^4 m^2$)	Source volume ($\times 10^4 m^3$)	Intensity
31°25'33"N, 103°31'21"E	26.97	399.52	38	109	RT3	125	2	3	VIII
30°57'29"N, 103°05'22"E	12.3	635.96	37.5	190	RT3	126	1.3	21	IX
31°31'13"N, 103°33'22"E	30	369.18	57	85	RT4	129	15.6	202.8	IX
31°29'01"N, 103°34'52"E	28.05	388.22	32	133	RT4	129	8.1	121	IX
30°56'29"N, 103°25'22"E	5.03	503.49	32	285	RT4	129	11.8	41.3	XI
31°29'02"N, 103°35'11"E	27.71	391.72	46	115	RT4	130	1.1	3.6	VIII
31°12'20"N, 103°23'52"E	13.8	601.61	41	252	RT3	131	11	187	X
31°33'55"N, 103°31'45"E	19.2	501.02	30	100	RT2	137	5	21.6	X
31°19'34"N, 103°27'39"E	19.9	490.12	25	100	RT3	140	3	30	X
30°57'47"N, 103°27'17"E	5.1	501.51	41	127	RT2	141	2.7	6.75	XI
31°32'34"N, 103°30'39"E	35	327.08	35	260	RT1	142	6.9	48.3	VIII
31°31'14"N, 103°32'34"E	32.5	347.02	38	60	RT4	142	1.6	6.7	VIII
31°33'54"N, 103°33'32"E	35	327.08	40	204	RT4	145	7.8	68.7	VIII
31°19'18"N, 103°28'41"E	38.3	303.63	31.5	58	RT4	148	0.5	2.2	VIII
30°52'58"N, 102°58'03"E	13.5	608.22	24	157	RT4	Block structure	11.58	60.79	X
30°56'16"N, 103°25'36"E	8.18	426.40	20	65	RT2	Block structure	4.97	3.57	XI
30°55'26"N, 103°24'25"E	8.02	429.80	28	110	RT4	Block structure	5.2	63	X
31°28'06"N, 103°37'41"E	22.61	451.53	25	180	RT3	Block structure	3.36	15.29	X
31°04'04"N, 103°29'31"E	1.04	1059.20	47	244	RT2	Block structure	8	6	XI
31°07'24"N, 103°17'01"E	14.6	321.17	46	55	RT4	Fractured structure	0.4	1.78	XI
31°31'38"N, 103°31'42"E	34.5	330.91	52	63	RT4	Fractured structure	0.97	5.8	VIII

Latitude, Longitude	D_{rup}	PHA (gal)	Slope angle (θ°)	Slope height (h, m)	Rock type	Geological structure, (joint inclination, θ°)	Source area ($\times 10^4 m^2$)	Source volume ($\times 10^4 m^3$)	Intensity
31°03'55"N, 103°12'39"E	13.55	335.03	39	90	RT4	Fractured structure	0.95	120	IX
31°31'31"N, 103°32'05"E	33.38	339.77	51	120	RT4	Fractured structure	1.5	8.7	VIII
30°54'12"N, 103°00'51"E	12.34	352.38	45	230	RT3	Fractured structure	1.8	16	IX
30°57'53"N, 103°06'25"E	9.9	392.70	51	43	RT1	Fractured structure	0.3	1.06	XI
31°18'36"N, 103°21'26"E	27.55	393.38	24.5	170	RT4	Fractured structure	2.2	7.72	VIII
31°13'14"N, 103°29'04"E	9.52	399.72	47	79	RT1	Fractured structure	0.45	1.37	XI
31°23'23"N, 103°29'54"E	22.98	446.67	40	110	RT4	Fractured structure	1.4	1.4	X
31°02'10"N, 103°28'06"E	1.92	608.03	42	62	RT3	Fractured structure	1.94	3.78	XI
31°07'27"N, 103°15'15"E	18.06	519.72	49	115	RT4	Fractured structure	3.5	110	X
30°54'56"N, 103°21'17"E	18.05	519.88	46	102	RT3	Fractured structure	5.4	22	X
31°04'10"N, 103°20'07"E	8.83	729.95	43	210	RT2	Fractured structure	5.2	140	XI
31°03'37"N, 103°20'27"E	7.67	766.90	28.5	90	RT2	Fractured structure	9.1	92	XI
31°15'01"N, 103°25'36"E	4.99	865.94	38.5	390	RT3	Fractured structure	3.2	10	XI
31°01'15"N, 103°28'09"E	3.28	941.42	56	76	RT2	Fractured structure	1.71	2.48	XI
31°02'16"N, 103°28'49"E	2.42	983.82	43	158	RT3	Fractured structure	1.8	23	XI

Table 3: 46 landslides with relatively long travel distance induced by Wenchuan earthquake

Latitude, Longitude(°)	Slope angle, $\theta(^{\circ})$	Slope transition angle, $\varepsilon(^{\circ})$	Slope height, $h(m)$	Source volume, $V(m^3)$	Source area, $A(m^2)$	L_{max} (m)	H_{max} (m)	PHA (m/s^2)	Rock type, RT	Reference
N31.563,E103.703	25	173	481	1.200E+07	2.857E+06	725	338	4.082	RT3	Li et al. 2010; Li and Kong,2010
N31.293,E103.848	40	170	361	2.430E+06	1.620E+05	710	386	5.373	RT2	Li et al. 2009,2010; Li and Kong,2010;
N32.055,E104.678	31	165	260	1.954E+06	1.149E+05	547	222	7.556	RT3	Li et al. 2009,2010; Li and Kong,2010;
N32.227,E104.865	30	162	481	1.920E+07	4.800E+05	843	400	6.754	RT3	Li et al. 2009,2010; Li and Kong,2010;
N32.181,E104.814	42	167	301	8.775E+05	2.925E+05	378	335	6.935	RT4	
N32.086,E104.658	35	166	254	2.022E+06	2.528E+05	347	243	6.503	RT4	Li et al. 2010; Li and Kong,2010
N32.412,E105.122	45	140	510	1.500E+07	1.284E+06	2600	650	6.916	RT3	Xu et al., 2009a; Fan and Qiao, 2010; Qi, et al., 2011
N32.431,E105.109	35	166	260	8.575E+06	4.970E+05	1829	710	6.316	RT3	Xu et al., 2009a; Li et al., 2010; Li and Kong, 2010
N32.451,E105.193	45	168	180	1.575E+06	4.145E+05	350	212	7.232	RT4	
N31.816,E104.448	52	140	602	1.400E+06	1.254E+05	1166	788	10.367	RT4	Xu et al., 2009a; Li et al. 2010; Li and Kong,2010
N31.647,E104.278	40	147	348	2.402E+06	1.101E+05	593	372	6.601	RT1	Xu et al., 2009a; Li et al. 2010; Li and Kong,2010; Fan and Qiao, 2010
N31.622,E104.141	50	165	310	1.500E+07	3.532E+05	1000	831	9.404	RT3	Xu et al., 2009a
N31.830,E104.459	35	165	350	2.400E+06	1.300E+05	680	350	9.536	RT3	Yin, 2009; Xu et al., 2009a
N31.919,E104.576	40	165	200	1.600E+06	4.711E+05	545	305	9.572	RT4	Xu et al., 2009a
N32.309,E104.966	21	168	250	1.200E+07	6.957E+05	2043	570	6.600	RT2	Xu et al., 2009a
N31.045,E103.458	41	149	420	7.500E+06	5.277E+05	3300	950	10.820	RT1	Xu et al., 2009a; Qi, et al., 2011
N31.553,E104.135	40	153	380	2.750E+07	2.946E+06	4170	1360	6.638	RT3	Xu et al., 2009a

Latitude, Longitude(°)	Slope angle, $\theta(^{\circ})$	Slope transition angle, $\varepsilon(^{\circ})$	Slope height, $h(m)$	Source volume, $V(m^3)$	Source area, $A(m^2)$	L_{max} (m)	H_{max} (m)	PHA (m/s^2)	Rock type, RT	Reference
N31.397,E103.841	45	143	550	2.500E+06	2.943E+05	1730	850	9.469	RT2	Xu et al., 2009a
N31.508,E104.226	43	168	254	3.449E+06	2.299E+05	1500	500	3.888	RT3	
N32.177,E104.821	35	155	450	3.520E+06	2.380E+05	550	345	7.156	RT4	Fan and Qiao, 2010
N32.093,E104.724	30	165	180	6.670E+05	5.973E+04	510	280	7.480	RT4	
N32.091,E104.780	35	163	200	7.500E+05	7.106E+04	567	350	8.835	RT4	
N32.704,E105.538	22	174	220	7.240E+05	1.206E+05	641	380	7.286	RT2	
N31.628,E104.342	25	171	200	6.370E+05	2.548E+05	1440	500	4.567	RT2	
N31.605,E104.198	46	150	200	2.418E+05	8.061E+04	803	210	7.903	RT2	
N31.911,E104.550	55	170	300	1.445E+07	4.817E+05	824	380	9.103	RT3	
N31.444,E104.018	29	173	250	1.956E+06	1.304E+05	825	400	6.327	RT2	
N32.426,E105.036	42	176	145	2.541E+05	1.271E+05	830	300	5.500	RT3	
N32.345,E105.037	37	164	120	1.219E+05	6.094E+04	873	260	6.970	RT3	
N32.298,E105.044	40	148	200	4.778E+05	1.195E+05	836	300	8.411	RT4	
N31.855,E104.306	39	157	300	3.484E+06	2.903E+05	839	520	5.915	RT3	
N31.516,E103.551	40	152	400	6.016E+05	2.005E+05	1107	600	3.580	RT3	
N32.264,E104.925	28	165	290	6.352E+06	4.234E+05	1128	550	6.910	RT2	
N32.634,E105.518	42	151	380	6.002E+05	2.401E+05	1131	500	8.870	RT3	
N31.833,E104.230	35	175	237	1.202E+07	6.011E+05	1222	430	5.401	RT2	
N31.845,E104.492	40	157	320	4.354E+06	5.984E+05	1433	860	10.053	RT3	Li and Kong,2010; Qi, et al., 2011
N31.302,E103.838	38	162	240	1.007E+06	3.357E+05	1635	730	6.047	RT1	Qi, et al., 2011
N31.510,E104.137	47	174	400	4.738E+05	1.579E+05	1156	740	5.511	RT2	Qi, et al., 2011

Latitude, Longitude(°)	Slope angle, $\theta(^{\circ})$	Slope transition angle, $\varepsilon(^{\circ})$	Slope height, $h(m)$	Source volume, $V(m^3)$	Source area, $A(m^2)$	L_{max} (m)	H_{max} (m)	PHA (m/s^2)	Rock type, RT	Reference
N31.660,E104.237	27	173	257	3.000E+06	1.694E+05	1180	485	10.465	RT2	Xu et al., 2009a; Fan and Qiao, 2010
N31.527,E103.770	34	170	421	9.100E+06	1.820E+06	580	391	4.940	RT4	Li et al. 2010; Li and Kong,2010
N31.676,E104.360	40	172	180	4.500E+04	1.344E+05	501	200	5.540	RT2	
N31.919,E104.576	42	150	360	3.400E+06	2.429E+05	920	370	9.567	RT4	Xu et al., 2009a
N31.919,E104.576	41	149	300	3.000E+06	2.727E+05	700	340	9.577	RT4	Xu et al., 2009a
N32.278,E104.941	37	166	140	6.500E+05	3.700E+04	400	180	6.867	RT3	Xu et al., 2009a; Yuan et al. 2011
N31.516,E104.222	46	167	391	9.750E+05	6.500E+04	542	468	4.080	RT3	Li et al. 2009,2010; Li and Kong,2010;
N32.222,E104.467	45	155	280	3.519E+05	8.796E+04	486	380	3.448	RT4	Qi, et al., 2011

Publication list

- [1] Deping Guo, Masanori Hamada, 2013. Qualitative and Quantitative Analysis on Landslide Influential Factors during Wenchuan Earthquake: a Case Study in Wenchuan County. *Engineering Geology*, 152, 202-209. (SCI)
- [2] Deping Guo, Masanori Hamada, 2012. Observed Stability of Natural and Reinforced Slopes During the 2008 Wenchuan Earthquake. *Journal of Japan Society of Civil Engineers, Ser. A1 (Structural Engineering & Earthquake Engineering (SE/EE))*, 68(2) 481-494.
- [3] Deping Guo, Masanori Hamada, Chuan He, Yufeng Wang, Yulin Zou. An Empirical Model for Landslide Travel Distance Prediction in Wenchuan Earthquake Area, *Landslides*. (SCI, Accepted)
- [4] Deping Guo, Masanori Hamada, Chong Xu, Chuan He. Analysis of the Relations Between Slope Failure Distribution and Seismic Ground Motion During the 2008 Wenchuan Earthquake. *Soil Dynamics and Earthquake Engineering*. (SCI, Major revision)
- [5] Deping Guo, Masanori Hamada, Hongyu Jia, 2013. Influential Factors on Slope Stability and Landslide Mobility. The 2nd IACGE International Conference on Geotechnical and Earthquake Engineering. (ASCE-GSP, In Press)
- [6] Deping Guo, Masanori Hamada, 2013. Susceptibility Analysis on Landslide Triggering Factors During the 2008 Wenchuan Earthquake. *Seventh International Conference on Case Histories in Geotechnical Engineering*, Chicago.
- [7] Deping Guo, Masanori Hamada, 2012. Lessons Learnt From Seismic Damage Induced by the 2008 Wenchuan Earthquake. *2012 International Conference on Vibration, Structural Engineering and Measurement, Applied Mechanics and Materials*, Vols. 226-228, pp.889-896, (EI, Oral Presentation)
- [8] Deping Guo, Masanori Hamada, 2012. Landslide Distribution Related with Seismic Ground Motion during the 2008 Wenchuan Earthquake. *Proc. of the First International Symposium on Earthquake Engineering, JAEE, Vol.1, 115–124, Tokyo*. (Parallel session, Oral presentation)
- [9] Deping Guo, 2012. Theoretical Analysis on Dynamic Responses of Single Surface Slope during Earthquake, *15th World Conference on Earthquake Engineering, Lisbon*. (e.poster).
- [10] Deping Guo, Masanori Hamada, 2012. Statistical Analysis of Landslides Triggered by Wenchuan Earthquake, *14th International summer Symposium of JSEC, Nagoya*. (Parallel session, Oral Presentation)
- [11] Deping Guo, Chuan He, Jimin Zhou, Ping Geng, 2009. Discussion on Anti-upward Moving Calculation Method of Submarine Shield Tunnel during the Construction and Service Stages, *Proc. of the Fifth China-Japan Conference on Shield Tunneling*, 152-158. (In Chinese with English abstract)
- [12] Jimin Zhou, Chuan He, Deping Guo, Zhun Tan, 2009. Research on Mechanical Behavior of Lining Structure Influenced by Embedded Depth of Submarine Shield Tunnel, *Proc. of the Fifth China-Japan Conference on Shield Tunneling*, 131-136. (In Chinese with English abstract)